POLYMER ELECTROLYTE MEMBRANE DEGRADATION AND OXYGEN REDUCTION IN FUEL CELLS: AN EPR AND DFT INVESTIGATION

Von der Fakultät Chemie der Universität Stuttgart zur
Erlangung der Würde eines Doktors der Naturwissenschaften
(Dr. rer. nat.) genehmigte Abhandlung

vorgelegt von

Dipl.-Chem. Alexander Panchenko

aus Jarowoje, Russland

Hauptberichter: Prof. Dr. Emil Roduner
Mitberichter: Prof. Dr. Hermann Stoll

Tag der mündlichen Prüfung: 12.10.2004

INSTITUT FÜR PHYSIKALISCHE CHEMIE
DER UNIVERSITÄT STUTTGART

Oktober 2004

Eidesstattliche Erklärung

Ich versichere, dass ich diese Dissertation selbstständig verfasst und nur die angegebenen Quellen und Hilfsmittel verwendet habe.

Stuttgart, 28.07.2004.   Alexander Panchenko

Prüfungsvorsitzender: Prof. Dr. Thomas Schleid

Hauptberichter: Prof. Dr. Emil Roduner

Mitberichter: Prof. Dr. Hermann Stoll

Tag der mündlichen Prüfung: 12.10.2004

CONTENTS

Abbreviations

A 501	Polyethersulfone reacted with bis(4,4'-diethylamino)benzophenone
ACF	Activated Carbon Fibers
ACM	Adiabatic Connection Method
CCM	Catalyst Coated Membrane
DBNBS	3,5-dibromo-4-nitrosobenzene-sulfonic acid
DEPMPO	5-diethoxyphosphoryl-5-methyl-1-pyrroline-N-oxide
DFT	Density Functional Theory
DMFC	Direct Methanol Fuel Cell
DMPO	5,5-dimethyl-1-pyrroline-N-oxide
EELS	Electron Energy Loss Spectroscopy
EPR	Electron Paramagnetic Resonance
FEP-g-PSA	Poly(tetrafluoroethylene-co-hexafluoropropylene) grafted with poly(styrenesulphonic acid)
GDE	Gas Diffusion Electrode
GGA	Generalized Gradient Approximation
HF	Hartree Fock
IRAS	Infrared Reflectance-Absorption Spectroscopy
KS	Kohn and Sham
LCAO	Linear Combination of Atomic Orbitals
LDA	Local Density Approximation
LSDA	Local Spin Density Approximation
LYP	Lee, Yang, and Parr
MEA	Membrane Electrode Assembly
ML	Monolayer
MOR	Methanol Oxidation Reaction
MPMS	Magnetic Property Measurement System
NEXAFS	Near Edge X-ray Adsorption Fine Structure
ORR	Oxygen Reduction Reaction
PAW	Projector Augmented Wave
PBI	Polybenzimidazole
PEK	Polyether(ether)ketone
PEMFC	Polymer Electrolyte Membrane Fuel Cell
PFSA	Perfluorosulfonic Acid

POBN	α-(4-pyridyl-1-oxide)-*N-tert*-butylnitrone
PROX	Preferential Oxidation
PS	Polystyrene
PSA	Pressure Swing Adsorption
PSU	Polyethersulfone
PTFE	Polytetrafluoroethylene
SERS	Surface Enhanced Raman Spectroscopy
sPEKH	sulfonated polyether(ether)ketone
SQUID	Superconducting Quantum Interference Device
UHV	Ultra High Vacuum
UPS	Ultraviolet Photoemission Spectroscopy
US	Ultra-Soft
VASP	Vienna Ab-initio Simulation Package
VWN	Vosko, Wilk, and Nusair

List of figures

List of tables

Chapter 1

1 INTRODUCTION

1.1 General introduction and main objectives

It is generally believed that fuel cells will play an important role in energy supply already in the near future [1 - 3]. Fuel cells will be providing energy for cars and trucks, producing electricity for utilities, and heating and cooling homes and businesses. They may even replace the expensive batteries in personal computers with power sources that can run for almost a year on a tea spoon full of alcohol.

The fuel cell is approximately twice as efficient in energy conversion through a chemical process than through combustion. Hydrogen, the simplest element consisting of one proton and one electron, is plentiful and is exceptionally clean as a fuel. Hydrogen makes up 90% of the composition of the universe and is the third most abundant element on the earth's surface. Such a wealth of fuel would provide an almost unlimited pool of energy at relatively low cost. But there is a price to pay. The fuel cell core (or stack), which converts oxygen and hydrogen to electricity, is expensive to build and maintain.

Hydrogen must be carried in a pressurized bottle. If propane, natural gas or diesel is used, a reformer is needed that converts the fuel to hydrogen. Reformers for Polymer Electrolyte Membrane Fuel Cells (PEMFCs) are bulky and expensive. They start up slowly, and further purification of the hydrogen is required. Often the hydrogen is delivered at low pressure, and additional compression is required. Some fuel efficiency is lost and a certain amount of pollution is produced. However, these pollutants are typically 90% less than what comes from the tailpipe of a car.

Major car manufacturers have teamed up with fuel cell research centers or are doing their own development. There are plans for mass-producing cars running on fuel cells. Because of the low operating cost of the combustion engine, and some unresolved technical challenges of the fuel cell, however, experts predict that a large scale implementation of the fuel cell to power cars will not occur before 2015, or even 2020.

Large power plants running in the 40,000 kW range will likely out-pace the automotive industry. Such systems could provide electricity to remote locations within 10 years. Many of these regions have an abundance of fossil fuel that could be utilized. The stack on these large power plants would last longer than in mobile applications because of steady use, even operating temperatures and absence of shock and vibration.

Fuel cells may soon compete with batteries for portable applications, such as laptop computers and mobile phones. However, today's technologies have limitations in meeting the cost and size criteria for small portable devices. In addition, the cost per watt-hour is less favorable for small systems than large installations.

High efficiency, low emission, fuel diversification, and silence are the most important advantages of the fuel cell technology today [4 - 6]. And one of the most promising types is the PEM fuel cell (PEMFC), but several shortcomings have to be overcome prior to its large-scale introduction to the market. Most crucial is its lifetime, for which more than 40,000 hours of continuous and stable performance are required. Poisoning of the platinum-based anode catalysts by trace amounts of CO inevitably contained in reformed fuel results in a severe reduction of performance [4, 7].

The advantages of the PEMFC technology are:

- there is no free corrosive liquid in the cell;

- it is simple to fabricate the cell;

- the cells are able to withstand large pressure differences;

- material corrosion problems are minimal;

- the cells have demonstrated long life.

The disadvantages of the PEMFCs are:

- the fluorinated polymer electrolyte is traditionally expensive and cell costs are high;

- water management in the membrane is critical for an efficient operation;

- CO tolerance is poor;

- kinetics of O_2 reduction at the cathode is relatively poor, especially at low temperatures;

- long term high performance with low catalyst loadings on the electrodes needs to be demonstrated;

- difficulty of its thermal integration into a reformer.

In this work we try to acquire new insights in problems of a long term stability for low temperature fuel cells. There are several points which have to be considered in this respect. Among them are the electrode stability, membrane stability, stability of bipolar plates and some others. We concentrate on the studies of membrane stability because the membrane is a

key component of a fuel cell often limiting the performance of a whole fuel cell system. In our studies the main aim is to monitor intermediates (i.e. organic radicals on the membrane surface) of the membrane degradation directly during fuel cell operation. We want to identify the species which are formed on the fuel cell catalyst and which lead to membrane degradation at the cathode and/or at the anode side of the fuel cell. Because of the fact that these intermediates are radicals, the EPR approach is a natural choice for such studies. Construction of a miniature fuel cell capable of operation in a resonator of an EPR spectrometer is a prerequisite for successful realization of the studies.

For a better understanding of the nature of the aggressive species ($^\bullet$OH, $^\bullet$OOH, H_2O_2) under conditions relevant for the fuel cells we employ *ab initio* DFT methods to study their behavior on different Pt surfaces present on the fuel cell catalyst with and without applied electric field. For obtaining accurate geometries and adsorption energies Pt substrates are modeled as infinite surfaces utilizing a periodic boundary approach, whereas for electric field calculations a cluster model of the Pt substrate is exploited. The issue of adsorbate solvation on Pt surfaces by coadsorbed water molecules and its possible influence on the adsorbate properties and reactivity is also considered. These studies are also of a great importance for a better understanding of the oxygen reduction reaction, aiming at a prediction of the factors which can facilitate the process or hinder it.

1.2   Organization of the Dissertation

The Dissertation consists of five main parts. In the INTRODUCTION a short foreword about research areas of interest and aims of the work are given. It is followed by the FUNDAMENTALS where several topics concerning fuel cell research are discussed. Fuel cells as power sources from an electrochemical point of view are introduced. Possible pathways of membrane degradation are pointed out. An introduction into specific aspects of fuel cell operation and oxygen reduction at the cathode side of the fuel cell provides a background for a better understanding of results obtained in experiments and calculations later-on. Recent ideas on oxygen reduction and its intermediates are exemplified and discussed.

The chapter EXPERIMENTAL AND THEORETICAL METHODS introduces the employed EPR and SQUID techniques as well as the *ab initio* DFT approach. The RESULTS AND DISCUSSION chapter summarizes experimental data from *ex situ* studies of fuel cell components and *in situ* EPR studies of radical formation and membrane degradation processes in a working fuel cell. Spin trap experiments on different membranes utilizing different spin trap molecules are discussed. Results of calculations on oxygen reduction aspects on three low index Pt surfaces are given. The presence of an applied electric field and coadsorbed water molecules as well as the significance for low temperature fuel cells are discussed. The SUMMARY resumes the results.

Chapter 2

2   FUNDAMENTALS

In this chapter several aspects of the low temperature fuel cell technology are discussed. An introduction into a complex process of oxygen reduction is given in the second part.

2.1   Selected issues of the fuel cell technology

Usually, William Grove is considered to be the inventor of the fuel cell. He described his hydrogen/oxygen fuel cell consisting of platinized platinum electrodes immersed in sulphuric acid in 1839 [8]. But in the 1830s Christian Friedrich Schönbein in Switzerland experimented with hydrogen and oxygen and air electrodes; so he was the actual initiator of the hydrogen/oxygen fuel cell [9]. He was a friend of Grove and stayed with him and they experimented together. Why Grove did not mention this, when he published first his gaseous cell in 1839, is not known.

The wish to convert the chemical energy of fossil fuels directly into electricity was popular already around 1900, and resulted in surprisingly large scale experiments trying to oxidize coal and coal gas electrochemically in "piles" [4]. The demise of all experiments at that time was caused by material problems. The systems were poorly designed and their operating lifetime was short. After 1920, the gas diffusion electrode was recognized as the key for successful low temperature operations.

After the Second World War the efforts were concentrated on an alkaline fuel cell system with porous metal electrodes. After the NASA Space Fuel Cells in 1968 research in the field became exciting again, porous carbon as a substrate with low catalyst loadings proved to be a low cost solution for hydrogen-air fuel cells and the interest in electric automobiles propelled by fuel cells became widespread, leading to several prototypes. In the middle 1970s the alkaline system, which had reached the highest level of development in the space programs, was replaced in world-wide research and development efforts by the phosphoric-acid system, which was seemingly better suited for stationary power plants. The obviously better overall efficiency together with the heat from a high temperature plant of molten carbonate fuel cell

systems in the 1980s and of solid oxide fuel cells in the 1990s accelerated the development of these new fuel cell types. The surprising turn in fuel cell technology occurred in the 1990s. The polymer electrolyte membrane fuel cell system appeared as the most attractive object for development. This system was already in existence in the 1960s, but it did not perform reliably in the space fuel cell projects, and its importance fell behind the alkaline systems. High power densities were obtained as a result of new membrane types and catalyst research. Operating life expectancies improved also considerably. Several large drawbacks remained: the membrane and electrode stability and performance still needed to be improved.

2.1.1 Electrochemical background

Historically, fuel cells are classified by the nature of the electrolyte and/or by the temperature of operation. Thus, one distinguishes between alkaline or acidic, or low temperature (up to approx. 100°C), medium (up to approx. 200°C) or high temperature (up to approx. 1000°C) fuel cells [10].

Table 1: The different fuel cells that have been realized and are currently in use and development.

Fuel Cell System	Electrolyte	Fuel	Oxidant	Temperature	Electrical efficiency
AFC	30% KOH	pure H_2	pure O_2	60-90°C	Cell: 60 - 70% System: 62%
PEMFC	H^+ conducting membrane	H_2	O_2, Air	50-100°C	Cell: 50 - 68% System: 43 - 58%
DMFC	H^+ conducting membrane	CH_3OH	O_2, Air	80-130°C	Cell: 20 - 30%
PAFC	concentrated H_3PO_4	natural gas, biogas, H_2	O_2, Air	160-220°C	Cell: 55% System: 40%
MCFC	molten Li_2CO_3, K_2CO_3	natural gas, biogas, H_2	O_2, Air	620-660°C	Cell: 65% System: 55 - 60%
SOFC	ZrO_2/YO_3	natural gas, biogas, H_2	O_2, Air	800-1000°C	Cell: 60 - 65% System: 55%

Low temperature fuel cells are the Alkaline Fuel Cell (AFC), the Polymer Electrolyte Membrane Fuel Cell (PEMFC) and the Direct Methanol Fuel Cell (DMFC). The medium temperature fuel cell is the Phosphoric Acid Fuel Cell (PAFC). Two different types of the high temperature fuel cell have been developed, these are the Molten Carbonate Fuel Cell (MCFC) and the Solid Oxide Fuel Cell (SOFC). All types are presented in Table 1 [11].

In a fuel cell making use of gaseous reactants, the anodic and cathodic reactants are fed into their respective chambers and an electrolyte layer is placed between the two electrodes. The half cell reaction at the anode yields electrons, which are transported through the external circuit and reach the cathode. These electrons are then transferred to the cathodic reactants. The circuit is completed by the transport of ions from one electrode to the other through the electrolyte. Table 2 [12] summarizes the anode and cathode processes for different fuel cell types.

Table 2: Electrode processes for different fuel cell types.

Fuel Cell System	Anode reaction	Cathode reaction
AFC	$H_2 + 2OH^- \rightarrow 2H_2O + 2e^-$	$\frac{1}{2}O_2 + H_2O + 2e^- \rightarrow 2OH^-$
PEMFC	$H_2 \rightarrow 2H^+ + 2e^-$	$\frac{1}{2}O_2 + 2H^+ + 2e^- \rightarrow H_2O$
DMFC	$CH_3OH + H_2O \rightarrow CO_2 + 6H^+ + 6e^-$	$\frac{3}{2}O_2 + 6H^+ + 6e^- \rightarrow 3H_2O$
PAFC	$H_2 \rightarrow 2H^+ + 2e^-$	$\frac{1}{2}O_2 + 2H^+ + 2e^- \rightarrow H_2O$
MCFC	$H_2 + CO_3^{2-} \rightarrow H_2O + CO_2 + 2e^-$	$\frac{1}{2}O_2 + CO_2 + 2e^- \rightarrow CO_3^{2-}$
SOFC	$H_2 + O^{2-} \rightarrow H_2O + 2e^-$	$\frac{1}{2}O_2 + 2e^- \rightarrow O^{2-}$

For the case of a hydrogen/oxygen fuel cell – the total reaction is:

$$H_2 + \frac{1}{2}O_2 \rightarrow H_2O \;\; with \; \Delta G = -237 \, kJ \, mol^{-1} \qquad (2\text{-}1)$$
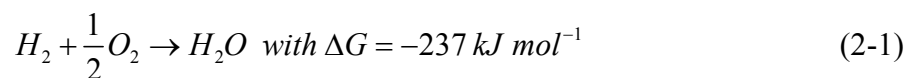
Hydrogen enters the pores of the anode and reaches the reaction zone, where gas, electrolyte (polymer membrane) and the solid conducting matter meet. The hydrogen gas diffuses to the electrochemically active site (e.g., a surface coated with a platinum catalyst),

where it is adsorbed and dissolved by the electrolyte. It dissociates and ionizes to $2H^+$. The two electrons are made available to the electrical circuit. The protons go through the electrolyte to the cathode and react with $1/2\ O_2$ to produce water, thereby taking up two electrons from the outer circuit. If the reaction is related to one oxygen molecule, the process produces a total of four electrons. The equilibrium cell voltage ΔE^0 for standard conditions at 25°C is:

$$\Delta E^0 = \frac{-\Delta G}{nF} = 1.23\,V \qquad (2\text{-}2)$$

The equilibrium cell voltage is the difference of the equilibrium electrode potentials of cathode and anode which are determined by the electrochemical reaction taking place at the respective electrodes:

$$\Delta E^0 = E_C^0 - E_A^0 \qquad (2\text{-}3)$$

Electrochemical reactions in a fuel cell are characterized by the thermodynamic equilibrium potential described by the Nernst equation. Even under no-current conditions the voltage of a fuel cell can be lower than the Nernstian value. When current flows, a deviation from the open circuit voltage occurs due to the electrical work performed by the cell. The deviation of the potential from the equilibrium value is called the overvoltage (overpotential) (η). For a redox reaction at one electrode the current density (j) is given by the Butler-Volmer equation:

$$j = j_0 \left\{ \exp(\alpha_A F\eta / RT) - \exp(-\alpha_C F\eta / RT) \right\} \qquad (2\text{-}4a)$$

$$\alpha_C = 1 - \alpha_A \qquad (2\text{-}4b)$$

with j_0 the exchange current density, α_A and α_C the transfer coefficients for the anodic and cathodic reaction, respectively, and η the overvoltage to drive the reaction. This equation holds when the charge transfer dominates the reaction at small values of j and η.

There are several types of the overvoltage which lead to irreversible losses of the potential in a particular fuel cell [4]. These are:

- "**Activation overvoltage**" is an expression for the voltage loss caused by the fact that the charge transport (charge transfer) in any material or process has a limited rate.

- "**Concentration overvoltage**" stands for voltage differences caused by diffusion processes (pressure gradients, changes in the usage rates of gases or liquids).

- "**Reaction overvoltage**" is a term for the voltage difference appearing when an earlier or simultaneous (related) chemical reaction produces another compound which changes the

operating conditions – for example, the water produced in a hydrogen-oxygen cell dilutes the electrolyte, which causes an electrolyte concentration change at the electrode interface.

- "**Transfer overvoltage**" is limited to the description of the changes in potential under load conditions as a fundamental interrelation of current and potential.

- "**Resistance overvoltage**" has no correlation with any chemical process at the electrodes and is simply the voltage drop across the resistive components of the cell.

At non-zero current densities, there is an activation overpotential: to drive the dissociation of the reactant molecules, a certain activation energy must be exceeded. Essentially, the oxygen and hydrogen molecules must diffuse through pores in the metal catalyst and adsorb. This is a "three-phase interface problem", since gaseous fuel, solid metal catalyst, and liquid electrolyte must all contact. The catalyst reduces the activation barrier, but a loss in voltage remains due to the still slow oxygen reaction. The hydrogen activation overpotential is negligible compared to the oxygen overpotential; the oxygen reaction is several orders of magnitude slower. Also, competing reactions occur at the oxygen electrode: oxidation of the platinum, corrosion of carbon support, and oxidation of organic impurities on the electrode. The total overpotential is 0.1 to 0.2 V, reducing the maximum potential to less than 1.0 V even under open circuit conditions.

There is also a continuous drop in voltage as current increases, and this is due to linear, ohmic losses (i.e. resistance) in the ionic conduction through the electrolyte. The thinner the membrane, the lower this loss. Thinner membranes are also advantageous because they keep the anode electrode wet by "back" diffusion of water from the cathode, where it is generated, towards the anode.

Finally, at very high current densities (fast fluid flows), mass transport causes a rapid drop-off in the voltage, because oxygen and hydrogen simply cannot diffuse through the electrode and ionise fast enough, and products cannot be moved out quickly enough.

These losses are most often shown in what is known as a Tafel plot or polarization curve; cell potential in volts is graphed versus the cell current density in amperes per square centimeters. The current density basically represents how fast the reaction is taking place (it is the number of electrons per second, divided by the surface area of the fuel cell electrolyte face).

The power curve as a function of current density ($E \cdot i$ versus i) shows a characteristic maximum beyond which decreasing voltage becomes a stronger negative effect than the increasing current.

Temperature and pressure dependencies of the fuel cell potential

The fuel cell potentials can be calculated theoretically at any temperature using the following equation if data for entropy changes of the corresponding cell reactions are available:

$$E = -\frac{\Delta H}{nF} + T\left(\frac{\partial E}{\partial T}\right)_P \tag{2-5}$$

The second term in equation (2-5) is related to the entropy change of the cell reaction by the equation:

$$nF\left(\frac{\partial E}{\partial T}\right)_P = \Delta S \tag{2-6}$$

The dependence of the pressure of the fuel cell potential can be expressed using following equation:

$$E_P = E_0 - \Delta n \frac{RT}{nF} \ln \frac{P}{P_0} \tag{2-7}$$

where E_P and E_0 are the cell potentials at (total) pressures of P and P_0, respectively. Δn is the change in the number of gaseous molecules during the reaction. The effect of pressure on the thermodynamically reversible cell potentials is small for reactions involving only liquids and solids. However, in the cases where gaseous reactants and products are involved, and if the volume change is significant (e.g., in the hydrogen-oxygen fuel cell), pressure effects must be taken into account. For example, increasing the total pressure from 1 to 10 atm in the H_2 - O_2 fuel cells changes the cell potential by 45 mV.

Fuel cell efficiencies

For the case of an electrochemical energy converter working ideally, it has been shown that the free-energy change of the reaction can be totally converted to electrical energy. Thus, the **thermodynamic efficiency** of a fuel cell can be given in a way:

$$\eta_{th} = \frac{\Delta G}{\Delta H} = 1 - \frac{T\Delta S}{\Delta H} \tag{2-8}$$

For most reactions utilized in fuel cells today, the thermodynamic efficiencies are greater than 90%. At the present time, overpotential losses reduce the practical efficiencies to values much less than the thermodynamic efficiencies. However, if sufficient advances in

electrocatalysis could be made (by reduction of overpotentials), it might be possible to attain practical efficiencies of over 100% and close to the maximum thermodynamic efficiencies.

A measure of the quality of a fuel cell – apart from operational life, weight, cost and other parameters – is the **electrochemical efficiency** and electrochemical kinetics of the electrodes. The electrochemical efficiency is also termed voltage efficiency and is defined as:

$$\eta_{el} = -\frac{nFE^K}{\Delta G} = \frac{E^K}{E^0} \tag{2-9}$$

where E^K is the operating potential and E^0 the standard electrode potential. Electrochemical efficiencies observed in H_2 - O_2 fuel cells are as high as 0.9 at low current densities and decrease only slowly with increasing current drawn from the cell until a limiting value is reached.

It is also useful to state the **practical efficiency** under load conditions, as this takes account of the influence of some irreversible processes:

$$\eta_P = -\frac{nFE^K}{\Delta H} \tag{2-10}$$

The **faradaic efficiency** is defined as:

$$\eta_f = \frac{I}{I_m} \tag{2-11}$$

I is the observed current from the fuel cell. I_m is the theoretically expected current on the basis of the amount of reactants consumed, assuming that the overall reaction in the fuel cell proceeds to completion.

The total efficiency of the fuel cell includes (excluding parasitic currents and self-discharging) pumping of the fuel and the oxidation material, and also the necessary energy for heating, cooling, compression and auxiliary installations. Exact data depend heavily on the system design and can only be obtained experimentally [4, 11].

Fuel cell systems are often used as co-generation systems, and the total efficiency often includes the thermal and electrical efficiency. Because the electrical energy is an energy form of a higher quality than the thermal energy, it is very important to make an exergy analysis which also includes application of the second law of thermodynamics.

2.1.2 Fuel cell components

PEMFCs use a proton exchange membrane as an electrolyte. They are low temperature fuel cells, generally operating between 85 and 105°C. The membrane is an electronic insulator, but excellent conductor of hydrogen ions. It consists of a fluorocarbon or F-free aromatic polymer backbone, to which sulfonic acid groups are attached. The acid molecules are fixed to the polymer and cannot "leak" out, but the protons on these acid groups are free to migrate through the membrane.

The membrane in PEMFCs is incorporated between two Gas Diffusion Electrodes (anode and cathode) forming the so-called Membrane Electrode Assembly (MEA).

The Gas Diffusion Electrodes (GDE) are composed of a thin catalyst layer of Pt or Pt-alloys deposited on carbon (0.01 - 0.05 mm) and a hydrophobic backing (0.1 - 0.4 mm) of carbon cloth or carbon paper. The function of the backing layer is to: 1) act as a gas diffuser; 2) provide mechanical support; 3) provide an electrical pathway for electrons. The backing layer is typically carbon-based, and may be in cloth form, a non-woven pressed carbon fibre configuration, or simply a felt-like material. The layer incorporates a hydrophobic material, such as polytetrafluoroethylene (PTFE). The function of PTFE is to prevent water from "pooling" within the pore volume of the backing layer so that gases freely contact the catalyst sites. Furthermore, it facilitates product water removal on the cathode as it creates a non-wetting surface within the passages of the backing material [13].

In the next two subsections membranes and electrodes which are currently used in PEMFCs will be in focus of detailed examination.

2.1.2.1 Membranes

The proton-conducting membrane is the key component of a fuel cell system, because only extremely stable membranes can withstand the harsh chemical and physical environment, which includes active noble metal catalysts, temperatures which can exceed 100°C, aggressive fuels and their partial oxidation products, aggressive oxidants, and the formation of reactive radicals. The essential requirements for polymer membrane electrolyte materials of PEMFC include: 1) proton conductivity; 2) chemical stability; 3) thermal stability; 4) mechanical properties (strength, flexibility, and processability); 5) low gas permeability; 6) low water drag; 7) fast kinetics of electrode reactions; 8) low cost and good availability [14].

The currently well-developed PEMFC technology is based on perfluorosulfonic acid (PFSA) polymer membranes (e.g., Nafion[®], the copolymer of tetrafluoroethylene and perfluoroether [15]) as electrolyte. The Teflon-like molecular backbone gives these materials excellent long term stability in both oxidative and reductive environments. A lifetime of over 60,000 hours under fuel cell conditions has been achieved with commercial Nafion[®] membranes [14]. However, even extremely stable Nafion[®] can suffer from degradation [16]. Using XPS analysis of the MEA before and after fuel cell operation Huang *et al.* found that -CF_2- groups of Nafion[®] are destroyed under electrochemical stress, yielding the -HCF- or -CCF- configurations [17]. Under the anode potential the hydrophobic part (e.g., fluorocarbon) may react with carbon or hydrogen atoms, resulting finally in the degradation of the electrolyte.

Although the perfluorinated ionomers show excellent performance under moderate conditions, considerable deterioration in the conductivity and the mechanical strength takes place above the glass transition temperature (ca. 110°C), which makes them unavailable for the use in high temperature fuel cells. The high cost and environmental inadaptability of the fluorinated polymers also urge the necessity to develop alternative proton-conducting polymers. A great number of polymer materials have been prepared and functionalised as membrane electrolytes for PEMFCs. Two main groups of polymers have been widely investigated for this purpose. One group is polymers containing inorganic elements, i.e., silicon in polysiloxanes [18], and zirconium in zirconium phosphates [19]. The other group is aromatic polymers with phenylene backbones.

Among the new approaches are different nonfluorinated ionically, covalently and covaletionically cross-linked polyaryl-blend membranes [20 - 24]. The stability of these materials must be investigated.

A localisation of the degradation would open the possibility to elucidate a mechanism and to prevent degradation by selective precautions. •OH and •OOH radicals originating during oxygen reduction at the cathode side of a fuel cell are responsible for the degradation reactions. Evidence for it are the formation of H_2O_2 as detected in product water, and other well known degeneration processes of polymers in general [25 - 28]. These radicals can also be formed via oxygen diffusion through the membrane and incomplete reduction at the fuel cell anode [29].

By combining the gas crossover results and the long term stability data it was shown that the rate of degradation increases with increasing gas crossover [30]. This indicates that the stability of the highly cross-linked membranes is not only caused by cross-linking of the

polystyrene chains, which slows down the loss of -SO_3H from the membranes, but also by reduced gas crossover and, therefore, reduced $^\bullet$OOH and $^\bullet$OH formation. High degrees of cross-linking (more than 12%) could improve the stability, however, the simultaneous increase of membrane resistance might not be tolerable [31]. The optimum membrane thickness which, as a compromise between gas crossover and resistance, must be found.
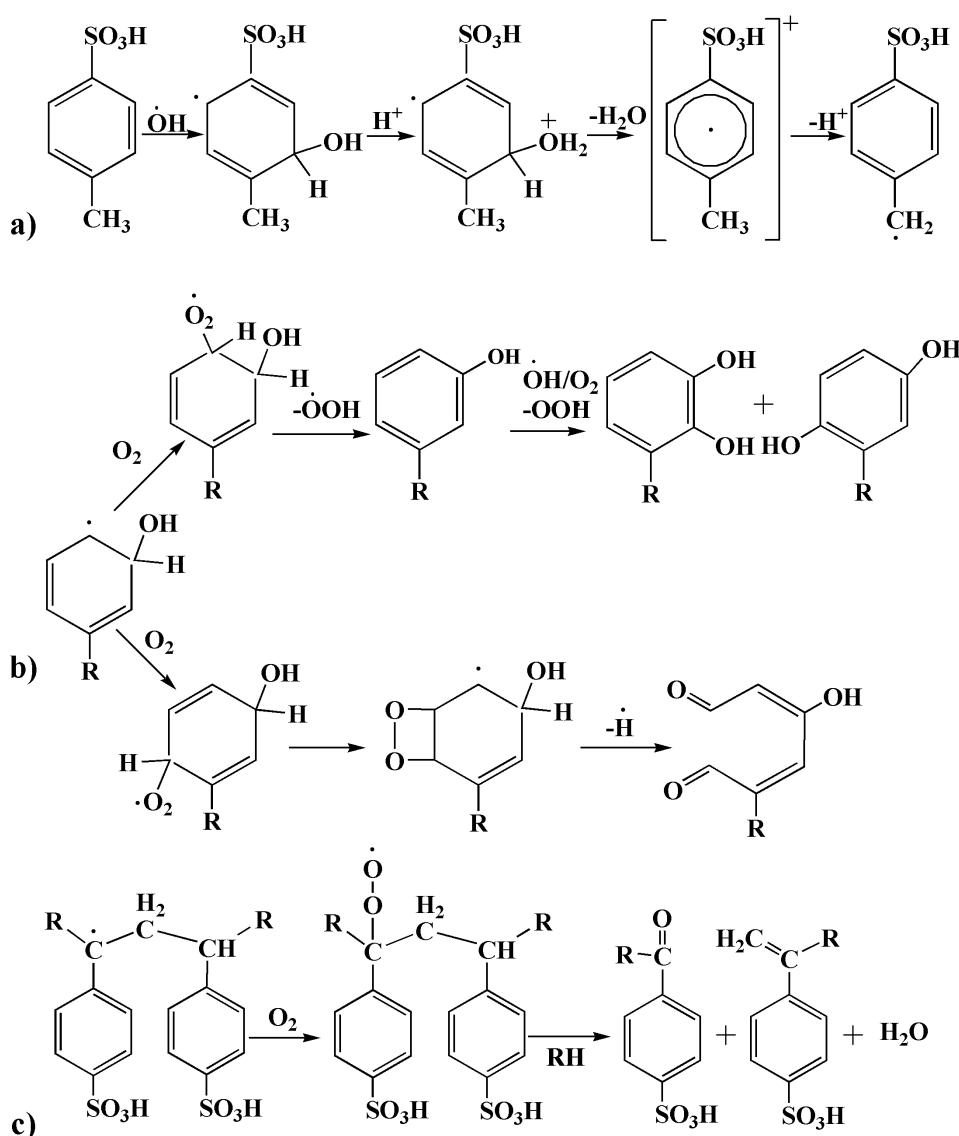
Fig. 1: Mechanisms of consecutive degradation processes caused by reactions with $^\bullet$OH radicals and oxygen molecules; a) formation of benzyl radicals by acid catalysis from hydroxycyclohexadienyl radicals; b) formation of different phenolic compounds and bond breaking; c) C-C bond breaking leading to the loss of -SO_3H groups [24, 27, 34].

Formed on the platinum catalyst active radicals can desorb from its surface and attack the membrane material [32, 33]. The dominating reaction in degradation processes of unsaturated polymers is the addition of $^\bullet$OH to the aromatic rings, preferentially in the *ortho* position to

alkyl- and RO-substituents (since in sulfonated PS, PSU, PEK and FEP-g-PSA the *para* position is substituted and thus blocked) (Fig. 1, path a)) [34]. It demonstrates the combined *ortho* activation by these substituents and the *meta* directing effect of the -SO₃H group in electrophilic addition reactions.

The crucial point is the acid catalysed water elimination from hydroxycyclohexadienyl adducts (Fig. 1, path a). This process requires the presence of labile benzylic α-H atoms, thus it is not relevant for PSU or PEK type membranes but important in the case FEP-g-PSA. In an endothermic process this can lead to chain scission ("reverse polymerisation") and thus to loss of -SO₃H groups. When water is eliminated from cyclohexadienyl radicals in polystyrenesulfonate, radical intermediates are identified by UV-VIS and EPR under acidic conditions [35]. They can act as centers of degradation reactions in all of the newly developed polymers. The lack of α-H atoms certainly contributes to a much better long term behavior [29].

Another crucial point is the C-O-C bond breaking, initiated by attack of •OH. This degradation mechanism is of relevance for the polymers with phenoxybenzene ether bridges like PSU or PEK. However, phenoxyl radicals are not observed at pH < 5, so the degradation may be avoided as long as the local pH is sufficiently low [34]. Fig. 2 summarizes possible sites from which degradation can start for several polymers [24].
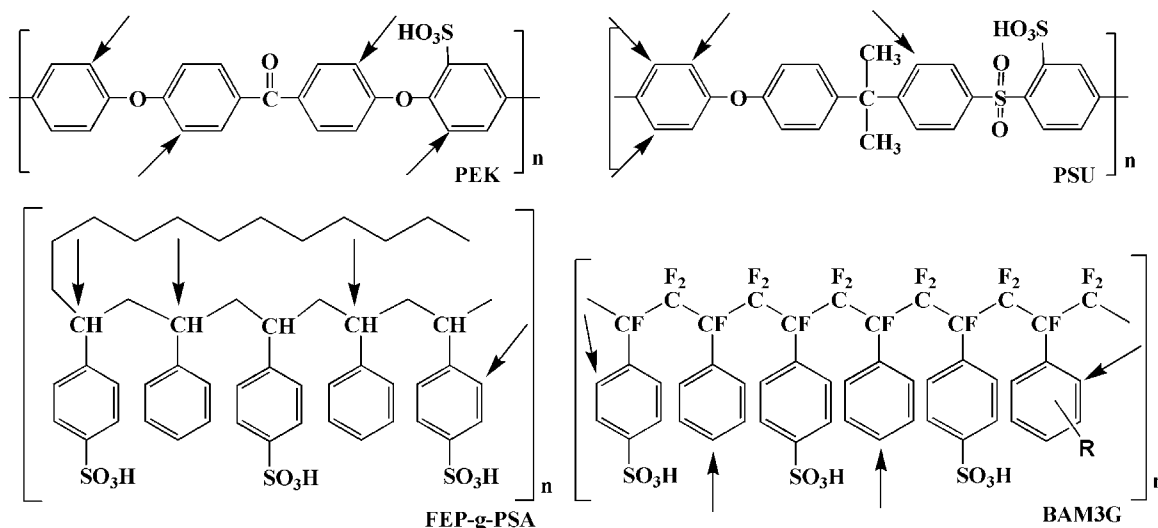
Fig. 2: Possible sites for •OH radical attack on various polymers used in proton-conducting membranes [24].

Under fuel cell operating conditions there is plenty of ³O₂ present, at least near the cathode. It was proposed that ³O₂ reacts with cyclohexadienyl radicals under formation of peroxy radicals, which finally leads to bond breaking within the aromatic rings [36].

In the presence of both $^\bullet$OH radicals and oxygen, complete degradation of the aromatic rings can be achieved within a few hours. In view of this, the saturated and perfluorinated Nafion$^\circledR$ which is much more inert has an inherent advantage over the new membranes based on aromatic hydrocarbons. However, perfluorinated membranes also have some severe disadvantages, including the high price and the high methanol permeability in direct methanol fuel cells which leads to cell potential reduction. So the needs for new membrane materials are extremely high today.

2.1.2.2   Electrodes

Electrodes for PEMFCs are generally porous GDEs to ensure the supply of the reactant gases to the active zones where the noble metal catalyst is in contact with the ionic and electronic conductor. The backing is a porous carbon cloth with a hydrophobic coating. To date, platinum has proven to be the best catalyst for both the hydrogen oxidation and oxygen reduction reactions. The main requirement of a good electrode is a three-phase boundary between the gas supply on the one hand, and the catalyst particle and the ionic conductor on the other hand.

When using humidified gases or methanol-water mixtures the catalyst layer must be sufficiently hydrophobic to prevent the pores from flooding. This hydrophobicity can be provided by introducing PTFE as a binder, in combination with Nafion$^\circledR$ that is hydrophobic. Usually the catalyst is made into an ink with water and isopropanol and mixed with the binder material. The ink can be cast straight onto the membrane.

To achieve the lowest Pt loadings, the metal is supported on high surface area carbon blacks with high mesoporous areas (> 75 $m^2\,g^{-1}$) and a degree of graphitic character, which leads to high electrical conductivity and good corrosion resistance, especially under cathodic conditions [37]. A high surface area of the carbon support is important in acquiring a high dispersion for Pt, and the pore structure may also be influential to the catalyst dispersion because the micropores may cause loss of the catalyst dispersion [38].

Under operating conditions for longer times a "ripening" of the Pt particles has been reported which manifests itself in a decrease of active surface area due to the formation of larger particles [39]. If the platinum particles cannot maintain their structure over the lifetime of the fuel cell, changes in the morphology of the catalyst layer from the initial state results in a loss of electrochemical activity [40].

Cathode processes

Although a huge variety of catalysts have been investigated, so far Pt-based catalysts are the superior material for the Oxygen Reduction Reaction (ORR). However, at relatively low temperatures typical for PEMFC the strong kinetic inhibition of the cathodic ORR leads to high overpotentials, amounting to several hundreds of millivolts. Therefore, the slow ORR kinetic is one of the limiting factors in the energy conversion efficiency of PEMFCs [41]. The high surface area carbon support is susceptible to corrosive processes limiting the lifetime of the cathode, and Pt catalyst have been suspected to accelerate the rate of carbon corrosion under conditions relevant for fuel cells [42].

Aspects of oxygen reduction will be discussed in more details in section 2.2.

Anode processes

The oxidation of hydrogen in PEMFCs occurs readily on Pt-based catalysts. The kinetics of this reaction is very fast on Pt catalysts, and in a fuel cell the oxidation of hydrogen at higher current densities is usually controlled by mass-transfer limitations [12]. The oxidation of hydrogen involves the adsorption of the molecule and electrochemical reaction to two ions as follows:

$$2Pt + H_2 \rightarrow Pt - H + Pt - H \tag{2-12}$$

$$Pt - H \rightarrow H^+ + e^- + Pt \tag{2-13}$$

Although this reaction is fast on Pt catalysts, in a fuel cell some problems may arise when impure hydrogen is used. Operating a fuel cell with pure hydrogen gives the best performance, but pure hydrogen is expensive and difficult to store. Alternatives to pure hydrogen are natural sources such as natural gas, propane or alcohols [43 - 45]. These substances have to be reformed, however, into hydrogen and even after gas clean up some contaminants such as carbon monoxide can still exist in the fuel feed. A PEMFC is extremely sensitive to even low concentrations of carbon monoxide produced by steam reforming due to severe poisoning of anode electrocatalysts. So although, in principle, a pure Pt catalyst can be used for hydrogen oxidation, similar studies into alloys have been carried out to improve the catalyst activity with contaminated hydrogen [46, 47].

Several physical and chemical purification methods, such as pressure swing adsorption (PSA), passage through inorganic or organic membranes, solvent absorption, water-gas shift reaction, methanation, and preferential oxidation (PROX), have been employed in order to reduce the CO concentration to under 100 ppm [48].

As with the methanol oxidation catalysts in DMFCs, the CO poisons the catalyst by blocking the active sites on the surface [49]. It is now widely accepted that the most promising catalyst materials used for the methanol oxidation reaction (MOR) are all platinum-based bimetallics. A generalized reaction scheme including the initial adsorption and dehydrogenation of methanol on the Pt surface and oxidative removal of the adsorbed intermediates was proposed already in 1977 [50].

Various Pt-based binary catalysts have been reported to decrease the poisoning effect of the intermediate products and to increase the long term stability of the electrocatalysts. The catalyst plays a bifunctional role enhancing the rate of methanol electrooxidation by supplying a surface oxide or other oxygen containing species at a lower potential than on pure Pt. Adding another metal to Pt also changes the position of the d-band center for Pt, which accounts for the adsorption energy of an adsorbate. This change can lower the CO adsorption energy on Pt and thereby gives more free Pt on the surface [51]. Thus, the use of bimetallic Pt-Co, Pt-Sn, Pt-Ni, $Pt-MoO_X$ [46, 52 - 54] leads to improved electrode performance. It is also known that the Pt-Ru catalyst has the highest catalytic activity for methanol oxidation [55 - 57]. However it has recently been reported that some ternary and quaternary alloy catalysts based on Pt/Ru have a higher catalytic activity than Pt-Ru [54, 58, 59].

2.1.3   Water management

Membranes in PEM fuel cells are generally water saturated to keep the conductivity high [60]. The water produced at the cathode does not dissolve in the electrolyte and is, instead, expelled from the back of the cathode into the oxidant gas stream. As the PEMFC operates at about 80°C, the water is produced as a liquid and is carried out of the fuel cell by excess oxidant flow. In the cell water transport processes are a function of the current and the characteristics of both the membrane and electrodes. Water transfer through the membrane is dependent on the difference between the relative humidity at the cathode and anode. So, influencing the water transport are the water drag through the cell, back diffusion from the cathode, and the diffusion of any water in the membrane and the electrodes themselves. One of the parameters on the anode side that plays an important role in the water transport process is the anode saturation temperature.

The number of water molecules transferred through the membrane per proton is approximately 3 and increases with increasing water content and increasing temperature [61].

The proton conductivity strongly increases with increasing concentration of absorbed water and falls with decreasing water content. One way of improving the water management is to humidify the gases coming into the fuel cell. Another form of water management can be found in the direct hydration of the membrane by mounting porous fibre wicks [62]. A novel method has been developed at Ballard. With appropriate stack design, liquid water accumulated in the cathode can be drawn across the membrane to the anode by a concentration gradient, and removed in the fuel stream. This method of water management, "anode water removal", can significantly reduce parasitic loads associated with the oxidant side of the fuel cell, and results in a totally new approach to fuel cell system design.

Under PEMFC conditions, the protonic current through the membrane produces an electro-osmotic water current in the same direction that leads to a depletion of water at the anode, resulting in an increased membrane resistance, i.e., a reduced fuel cell performance. So, the mechanisms of membrane dehydration are: 1) electro-osmotic drag pulling water from anode to cathode; 2) loss of water to undersaturated fuel or air streams [63]. Operating the fuel cell below 0°C leads to water freezing inside the membrane and dramatic reduction of its performance. However, the removal of water from the PEMFC by supplying dry gases or an antifreeze solution before the cell temperature falls to bellow 0°C can prevent the performance degradation [64].

2.2   Oxygen reduction on Pt catalysts

In this section some results from fundamental experimental and computational studies concerning the species of interest in our computations will be discussed. Most of these studies were carried out for the platinum-UHV interface, which leads to the best-defined conditions. I would like to point out that these are not necessarily the conditions most applicable to the electrochemical interface.

2.2.1   Reduction pathways

Platinum catalysts are involved in a vast variety of red-ox reactions, and O_2 reduction is one of the most important of them. Therefore, enormous efforts are undertaken by electrochemists to understand fundamental aspects of Pt catalysts and to improve the properties of applied catalytic systems in general. The fundamental relevance of Pt catalytic properties has become even more important because carbon-supported Pt catalysts have so far been the best choice for the oxygen reduction at the cathode of low temperature PEMFCs [52].

The ORR on Pt surfaces has been widely studied in electrochemistry, but the details of the mechanism remain elusive. The overall ORR is a multi-step process involving four electron transfers during which bonds are broken and formed. Damjanovic proposed that the first step is electron transfer to the O_2 molecule:

$$O_2 + e^- \rightarrow O_2^-$$
(2-14)

This step is rate determining and is either accompanied by or followed by a fast proton transfer [65, 66]. Recent results by Markovic *et al.* [67] support this proposal based on their experiments on oxygen reduction at single-crystal electrodes.

A theoretical study by Sidik *et al.* has proven the first electron transfer to be rate determining on dual adsorption sites. Proton transfer is involved in this step, because the electron affinity of the reactant complex is increased significantly by the proton field, and this lowers the activation energy for reduction [68]. In the potential range of 0.47 - 1.20 V, the calculated barrier for the formation of $^\bullet$OOH is lower than the calculated 0.74 eV O_2 dissociation barrier, implying that O_2 does not dissociate on the Pt electrode before the first electron transfer.

From the experimental point of view, there is evidence for the dissociative adsorption of O_2 at the platinum-UHV interface at room temperature [69], but there is no evidence for the direct cleavage of the O-O bond at the electrochemical interfaces.

In general, O_2 reduces by either $2e^-$ to H_2O_2, or by $4e^-$ to H_2O, depending on the electrode material and surface modifications [66]. Adzic and coworkers [70] distinguish the following pathways: 1) a "direct" four-electron reduction to H_2O (in acidic media) or to OH^- (in alkaline media) without hydrogen peroxide detected on the ring; 2) a two electron pathway involving reduction to hydrogen peroxide; 3) a "series" pathway with two- and four-electron reduction; 4) a "parallel" pathway that is a combination of (1), (2), and (3); 5) an "interactive" pathway in which diffusion of species from the "series" pathway into a "direct" pathway is possible.

It is now well established that the reaction rates of the oxygen reduction on different low index Pt surfaces are structure sensitive, due to structure sensitive adsorption of spectator species, such as O_{2ads}, $^\bullet OH_{ads}$, and $^\bullet OOH_{ads}$. The adsorption properties of the $^\bullet OH$ species are probably the most important in the process. In 0.05 M H_2SO_4 the ORR rate increases in the sequence Pt(111) < Pt(100) < Pt(110) [71]. An exceptionally large deactivation is observed at the (111) surface probably due to competition of the strongly adsorbing (bi)sulfate anion. In perchloric acid solution, the variation in activity at 0.8 - 0.9 V is relatively small between the three low index faces, with the activity increasing in the order (100) < (110) $\approx$ (111) [67]. A similar structural sensitivity is observed in 0.1 M KOH. In the potential range where O_2 reduction is under combined kinetic-diffusion control ($E > 0.75$ V), the activity increases in the sequence (100) < (110) < (111) [72]. The decrease of the (100) surface activity is related to a high affinity of (100) sites for the hydroxyl adsorption, leading to a lack of active centers for O_2 adsorption on Pt(100) as it is highly covered with $^\bullet OH_{ads}$. Markovic *et al.* suggested that the rate of O_2 reduction should be proportional to that part of the surface not covered by the hydroxyl species ($1 - \Theta_{OH}$). As is be shown below, our computational results also support a structure sensitivity of the oxygen molecule and the oxygen reduction intermediates adsorption, in particular through the strong adsorption of $^\bullet OH$ on Pt(100).

Theoretical studies of oxygen containing species adsorbed on the Pt surface yield detailed information about the adsorption and reaction properties on a molecular level. Because of the importance of the system, the adsorption of (molecular) oxygen species has been a key issue of theoretical investigations by a large number of specialists, but in most cases the studies were restricted to the (111) and (100) surfaces [73 - 75].

Using a single platinum atom for coordinating O_2, H_2O, $^\bullet OOH$, H_2O_2, and $^\bullet OH$ intermediates in the oxygen reduction Anderson and co-workers suggested the following lowest energy single-electron pathway for oxygen reduction [73]:

$$Pt + O_2 \rightarrow Pt - O_2 \tag{2-15}$$

$$Pt - O_2 + H^+(aq) + e^-(E) \rightarrow Pt - OOH \tag{2-16}$$

$$Pt - OOH + H^+(aq) + e^-(E) \rightarrow Pt - O + H_2O \tag{2-17a}$$

$$Pt - O + H^+(aq) + e^-(E) \rightarrow Pt - OH \tag{2-17b}$$

$$Pt - OOH + H^+(aq) + e^-(E) \rightarrow Pt - (HOOH) \tag{2-18}$$

$$Pt - (HOOH) + H^+(aq) + e^-(E) \rightarrow Pt - OH + H_2O \tag{2-19}$$

$$Pt - OH + H^+(aq) + e^-(E) \rightarrow Pt - OH_2 \tag{2-20}$$
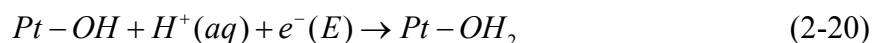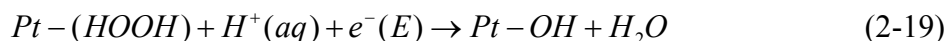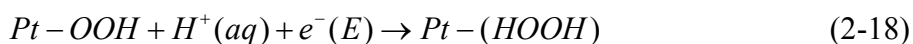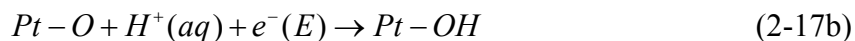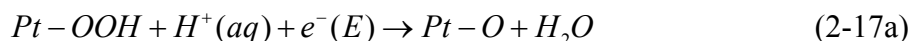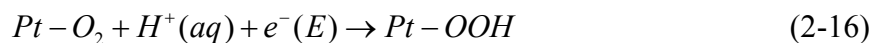
Compared to the uncatalyzed outer Helmholtz plane values, bonding to the platinum atom has the effect of decreasing the calculated activation energies for O_2 and H_2O_2 reduction. The activation energy for $^\bullet OH$ radical reduction to H_2O increases when $^\bullet OH$ is bonded to the Pt atom, and bonding to Pt decreases the activation energies of $^\bullet OOH$ reduction to H_2O_2. The activation energies are predicted to increase with increasing potential. Anderson's calculations predict an activation energy of 0.43 eV for oxygen reduction at the standard equilbrium potential. At 1.23 V the experimental activation energy is 0.44 eV on the three low index Pt surfaces in 0.05 M H_2SO_4 [76]. The rate-determining step appears to be the addition of the first electron to O_{2ads} [66]. Hartnig and Koper have recently modeled this electron addition as a Marcus-type outer-sphere electron transfer reaction using large-scale molecular dynamics simulations [77].

A reaction that interferes with the red-ox system is the oxidation of the water molecule:

$$Pt - OH_2 \rightarrow Pt - OH + H^+ + e^- \tag{2-21}$$
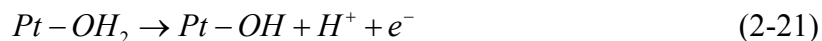
which leads to adsorbed hydroxyl radicals [78]. Reaction (2-21) is the main source of adsorbed $^\bullet OH$ in the system and therefore primarily responsible for the surface poisoning, i.e. the $(1 - \Theta_{OH})$ term mentioned above.

Radicals are deemed important in understanding the degradation effects in a working fuel cell [79]. It is therefore of key interest to explore the energetics of reaction intermediates on Pt surfaces. How strongly do the radicals adsorb and under which conditions do they leave the surface of the Pt catalyst to deploy their destructive nature? Under different fuel cell running conditions the catalyst experiences different electric potentials. Which influence can it have

on the adsorption/desorption of the oxygen species and on the catalytic reaction in general? The present work tries to provide insight into these issues (see section 4.3).

The main results of our computations are the potential-dependent adsorption properties of oxygen and intermediates of the reduction of oxygen on the three low index platinum surfaces (111), (110), and (100). It is now generally accepted that the slab geometry with periodic boundary conditions is the best model for obtaining accurate chemisorption energies and geometries on the surface. Therefore, such calculations have been used for the present purpose. Cluster models can describe local properties such as adsorbate geometries, vibrational frequencies, and bonding mechanism [80]. Moreover, it was shown recently that for CO and OH⁻ adsorbed on Pt, the cluster model can be successfully applied for the description of the Stark tuning rate [81 - 83]. Therefore, we have used a cluster model to describe properties of the adsorbed oxygen containing species as a function of an applied electric field, as this also leads to a significant reduction of computation time.

2.2.2 Background of the Oxygen Reduction Reaction

2.2.2.1 O_2

The adsorption of oxygen on Pt surfaces has been identified as a fundamental step of its reduction mechanism [84, 85]. Experiments at the platinum-UHV interface have shown that oxygen adsorbs both dissociatively and molecularly on the (111) surface. Adsorbed molecular oxygen is found at temperatures lower than 150 K, dissociation of adsorbed oxygen takes place at higher temperatures [69].

Previous spectroscopic studies identified three distinct chemisorbed states of oxygen on the Pt(111) surface. Two of them are adsorbed molecular species: the superoxolike (O_2^-) state is formed at bridge sites with an intramolecular bond order of 1.5 and a vibrational frequency of 870 cm^{-1}, and the peroxolike (O_2^{2-}) state formed at threefold hollow sites with an intramolecular bond order of 1.0 and a stretching frequency of 690 cm^{-1} [75, 86]. EELS and NEXAFS measurements have shown that at near-zero surface coverages, the peroxolike molecular precursor is observed exclusively, while both the superoxolike and peroxolike forms are detected at higher coverages [87, 88].

Because of an additional electron in the antibonding π^*-orbital of the molecule the peroxolike oxygen is often referred to as a precursor state for dissociation [89]. Dissociation on Pt(111) surface proceeds by sequential population of superoxolike and peroxolike precursor states [84]. Dissociation has been observed to result from heating to temperatures above 100 K or UV light irradiation.

Atomic oxygen is by far the energetically most stable configuration of oxygen on Pt surfaces. Upon heating to above 150 K, both molecular species disappear completely from the surface in favor of atomic oxygen that is observed in threefold hollow sites, featuring a Pt-O bond frequency of 471 cm^{-1} [90].

2.2.2.2 $^\bullet$OH radical

Hydroxyl adsorbates are key intermediates on the PEMFC cathode as they are generally held responsible for blocking adsorption sites for oxygen. Spectroscopic investigations of hydroxyl groups on low index Pt surfaces have been the focus of recent research in many groups. On Pt(111), Fisher and Sexton reported that $^\bullet$OH$_{ads}$ could be prepared by adsorption of H_2O on a layer of preadsorbed O atoms at 100 K and subsequent heating to above 150 K, leading to the formation of $^\bullet$OH groups [91]. It is a matter of debate and possibly depends on the method of preparation whether $^\bullet$OH$_{ads}$ is bound at atop [92] positions or in threefold hollow sites [93, 94].

Previous theoretical studies of the system have shown that at low coverages (from 1/9 of a monolayer (ML) to 1/3 ML) $^\bullet$OH binds preferentially at bridge and atop sites with a chemisorption energy of ~2.25 eV [95]. At high coverages (1/2 to 1 ML) hydrogen bonding between adjacent hydroxyl groups leads to: 1) an enhancement in $^\bullet$OH chemisorption energy by about 15%; 2) a strong preference for $^\bullet$OH adsorption at atop sites; and 3) the formation of $^\bullet$OH networks.

Koper and co-workers found that $^\bullet$OH has a tendency to adsorb upright in the hollow site [96, 97]. However, both in atop and bridge positions, a tilting of the molecule leads to significant lowering of the binding energy on platinum. More importantly, when coadsorbed with water on Rh(111), a DFT study by Vassilev et al. showed that $^\bullet$OH lies almost flat on the surface, with the oxygen coordinated to an atop surface atom [98].

2.2.2.3 H_2O_2

Depending on the properties of the Pt electrode surface H_2O_2 can be formed in appreciable amounts during the ORR. The yield of hydrogen peroxide on a typical fuel cell catalyst such as Pt/Vulcan amounts to ca. 15%, in a close agreement with the average value of H_2O_2 produced on Pt(100) (ca. 25%) and Pt(110) (ca. 2.5%) single crystal surfaces [66].

Hydrogen peroxide is unstable on low index Pt surfaces and decays into a water molecule and molecular oxygen [99]:

$$2H_2O_2 \rightarrow 2H_2O + O_2 \qquad (2\text{-}22)$$

The activation energy for the colloidal Pt catalyzed reaction requires about 49 kJ mol^{-1} [100]. Furthermore, H_2O_2 can dissociate on Pt surfaces into two hydroxyls. Another path that has been suggested includes the formation of $^\bullet$OOH radicals and $^\bullet$H atoms [101, 102]:

$$Pt - H_2O_2 \rightarrow Pt - OH + Pt - OH \qquad (2\text{-}23)$$

$$Pt - H_2O_2 \rightarrow Pt - OOH + Pt - H \qquad (2\text{-}24)$$
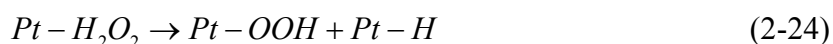
It has been proposed that $^\bullet$OH$_{ads}$ initiates the autocatalytic dissociative adsorption of hydrogen peroxide. Hydroxyl groups present at hollow sites of the Pt surface promote the adsorption of hydrogen peroxide with negatively polarized oxygen atoms of H_2O_2 directed to surface Pt atoms.

2.2.2.4 H_2O

When one speaks about the ORR on metal surfaces one has to take into account that the surface is not clean but always covered with adsorbed water molecules. Intermediates of the oxygen reduction are thus solvated on the surface. The water-metal interaction has been one of the most studied adsorption cases since the establishment of modern surface science some 20 years ago [103].

Ogasawara *et al.* found that water on the Pt(111) surface forms a nearly flat overlayer with both metal-oxygen and metal-hydrogen bonds formed to the surface [104]. A recent DFT study showed that whereas a single water molecule adsorbs flat on Pt(111) with a binding energy of ca. 0.30 eV, the binding energy in a bilayer (2/3 coverage) increases to ca. 0.53 eV due to hydrogen bond formation [105].

Chapter 3

3 EXPERIMENTAL AND THEORETICAL METHODS

This chapter consists of two subchapters. The first one characterizes the EPR and SQUID techniques which are employed in our studies. In the second one a brief introduction into the *ab initio* DFT approach used for our calculations is supplied.

3.1 Description of experiments

3.1.1 Electron Paramagnetic Resonance

The Electron Paramagnetic Resonance (EPR) deals with the interaction of electromagnetic radiation with magnetic moments which arise from the electrons. Electromagnetic radiation may be regarded classically as coupled electric (*E*) and magnetic (*B*) fields perpendicular to the direction of propagation. Both oscillate at some frequency *ν*. For EPR the commonly used frequency range is 10^9 - 5×10^{11} s^{-1} (1 - 500 GHz) [106, 107].

The EPR measurements owe their origin to the magnetic properties of the electron which, since it has a magnetic moment (associated with the electron spin), will interact with an external magnetic field. Simply, the electron can behave like a small bar magnet when placed in a magnetic field, trying to align itself with the external field. It is then possible to cause the electron to "flip" from alignment with the external field, to alignment against the field by irradiation with suitable (microwave, GHz) electromagnetic radiation. EPR is successful in obtaining structural information of molecules and details of electron density distributions.

The unique feature of EPR spectroscopy is that it is a technique applicable to systems in a paramagnetic state (or which can be placed in such a state), that is, a state having net electron angular moments (usually spin angular moments). Either the species exists in a paramagnetic ground state or it temporarily may be excited into a paramagnetic state, for instance by

irradiation. Thus, in principle, all atoms and molecules are amenable to study by EPR. Typical systems that have been studied include:

- free radicals in the solid, liquid, or gaseous phases;

- transition ions including actinide ions;

- various point defects (localized imperfections) in solids;

- systems with more than one unpaired electron (triplet-state systems, biradicals);

- systems with conduction electrons.

The interaction between the electron spin and the external magnetic field B_0 expressed in an arbitrary coordinate system is described by the **electron Zeeman** term:

$$H_{EZ} = \beta_e B_0 g S / \hbar \tag{3-1}$$

For a spin system with $S = 1/2$, H_{EZ} is the dominant term in the Hamiltonian at the usually applied static fields. g can be written as a symmetric tensor with six independent quantities. Usually the g principal axes frame is considered as the molecular frame and all interaction tensors are referred to this frame. For cubic symmetry, $g_x = g_y = g_z$; for axial symmetry $g_x = g_y = g_\perp$ and $g_z = g_\parallel$, and for orthorhombic and lower symmetry $g_x \neq g_y \neq g_z$ [108].

For spin systems with group spin $S > 1/2$ and non-cubic symmetry, the dipole-dipole coupling between the electron spins removes the $(2S + 1)$-fold degeneracy of the ground state. This interaction is field-independent and is therefore also called **zero-field splitting**. It can be expressed by the fine structure term:

$$H_{ZFS} = SDS \tag{3-2}$$

where D is the symmetric and traceless zero-field interaction tensor.

The **hyperfine** interaction between an electron and a nuclear spin described by the Hamiltonian:

$$H_{HF} = SAI \tag{3-3}$$

comprises one of the most important sources of information on EPR spectroscopy. The Hamiltonian can be written as the sum of the isotropic or Fermi contact interaction H_F and the electron-nuclear dipole-dipole coupling H_{DD}:

$$H_{HF} = H_F + H_{DD} \tag{3-4}$$

The coupling of a nuclear spin I to the external field B_0 is described by the **nuclear Zeeman** interaction:

$$H_{NZ} = -g_N \beta_N B_0 I / \hbar \tag{3-5}$$

The spin quantum number I and the nuclear g_N are inherent properties of a nucleus. For stable isotopes, I covers the range from 1/2 (e.g., ^{1}H, ^{13}C) to 6 (^{50}V). In most EPR experiments the nuclear Zeeman interaction can be considered to be isotropic. For protons the nuclear Zeeman interaction is only 1/658 of the electron Zeeman interaction, for all other nuclei it is even less.

Nuclear quadrupole interaction is possible for nuclei with spin ≥ 1 because of the non-spherical charge distribution described by a nuclear electrical quadrupole moment Q. The interaction of this charge distribution with the electric field gradient, caused by the electrons and nuclei in its close vicinity, is described by the Hamiltonian:

$$H_{NQ} = IPI \tag{3-6}$$

where P is the nuclear quadrupole tensor. In the EPR spectrum, nuclear quadrupole interactions manifest themselves as shifts of the allowed resonance lines and in the appearance of forbidden transitions. Both contributions represent small second-order effects which are difficult to observe.

The dipole-dipole interaction between two nuclear spins I_i and I_k (**nuclear spin-spin interaction**) can be written as:

$$H_{NN} = I_i d^{(i,k)} I_k \tag{3-7}$$

Nuclear dipole-coupling tensors $d^{(i,k)}$ provide one of the main sources of structural information in solid state NMR. In EPR spectra of solids this interaction is far too small to be resolved.

According to the discussed interactions the energies of states within the ground state of a paramagnetic species with an effective spin S and n nuclei with spins I are described by the static spin Hamiltonian:

$$H_0 = H_{EZ} + H_{ZFS} + H_{HF} + H_{NZ} + H_{NQ} + H_{NN} \tag{3-8}$$

EPR spectroscopy can be used for a complete structure characterization of a system which includes the chemical identity, geometrical structure, and dynamics of the system. The geometric structure can be inferred from distances between nuclei and angles between structure elements. Often the properties and function of a material or biological system cannot be fully explained on the basis of a static structure. EPR techniques can provide insight in dynamics of a system of interest.

In our experiments EPR spectra were recorded with Bruker EMX X-band spectrometer. g values were calculated relative to the Bruker® weak pitch sample (g = 2.0028). They are accurate to $\pm$ 0.0002 units. The microwave power was varied in the region 0.1 - 20.0 mW.

Modulation amplitude: 1 - 5 G. Low temperature experiments were performed in a special cooling unit, which can operate in the temperature range 1.8 - 300 K.

3.1.1.1   Spin trapping technique

EPR is considered to be the only method that we can use for directly observing the radicals formed during fuel cell operation. However, the direct detection of the radicals formed is not always possible with the EPR method. The radicals formed are usually very reactive and have short lifetimes. These properties result in a very low steady state radical concentration, below the limit of EPR detection.

Spin trapping, a technique developed in the 1970's [109], is considered to be a powerful tool to visualize short-lived radicals indirectly. In this technique, a diamagnetic compound, called a spin trap, reacts with a primary radical to form a more stable radical that can accumulate to a high enough concentration for an EPR study. There are two categories of compounds that are commonly utilized as spin traps: nitroso and nitrone compounds. Nitroso spin traps react with radicals in a way shown in Fig. 3a.
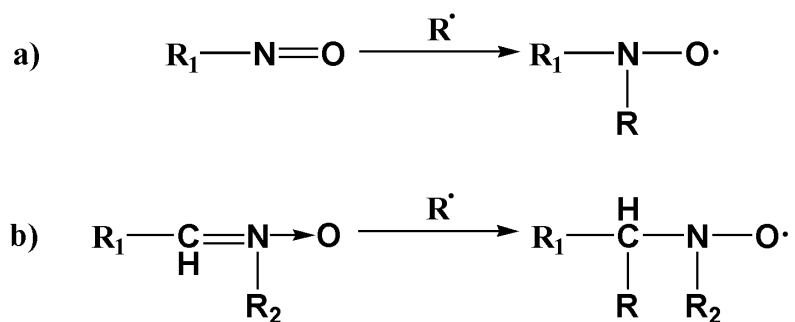
Fig. 3: Chemical reactions of the spin trap molecules with short-lived radicals; a) nitroso spin traps, b) nitrone spin traps.

The advantage of the nitroso spin adduct is that it can yield a lot of structural information about the primary radical. With the nitroso spin adducts, different primary radicals have different β-H, which will have different hyperfine splitting parameters.

Nitrone spin traps react with radicals according to scheme shown in Fig. 3b. The structural information that we can get from nitrone compounds will be less than that from nitroso compounds because the β-H is not from the trapped radical but from the nitrone compound.

However, the most popular nitrone compounds, such as DMPO and POBN still can provide information from the hyperfine splitting parameters [110].

The spin trapping technique opens numerous possibilities to study mechanisms of chemical reactions in which the formation of free radicals is involved. Using a proper spin trap it is possible to detect free atoms (e.g., ${}^\bullet$F, ${}^\bullet$Cl, ${}^\bullet$H, etc.), free radicals in the gas phase, radicals in solids and liquids, etc. [109].

Different spin traps show different selectivities in short-lived radical capture [111], so we used a range of spin traps including both nitrone and nitroso types of spin traps. The spin traps α-(4-pyridyl-1-oxide)-*N*-*tert*-butylnitrone (POBN), 5,5-dimethyl-1-pyrroline-*N*-oxide (DMPO), 3,5-dibromo-4-nitrosobenzene-sulfonic acid (DBNBS) were purchased from Aldrich®. The spin trap 5-diethoxyphosphoryl-5-methyl-1-pyrroline-*N*-oxide (DEPMPO) was purchased from Calbiochem®. Fig. 4 shows the spin traps used in the study.
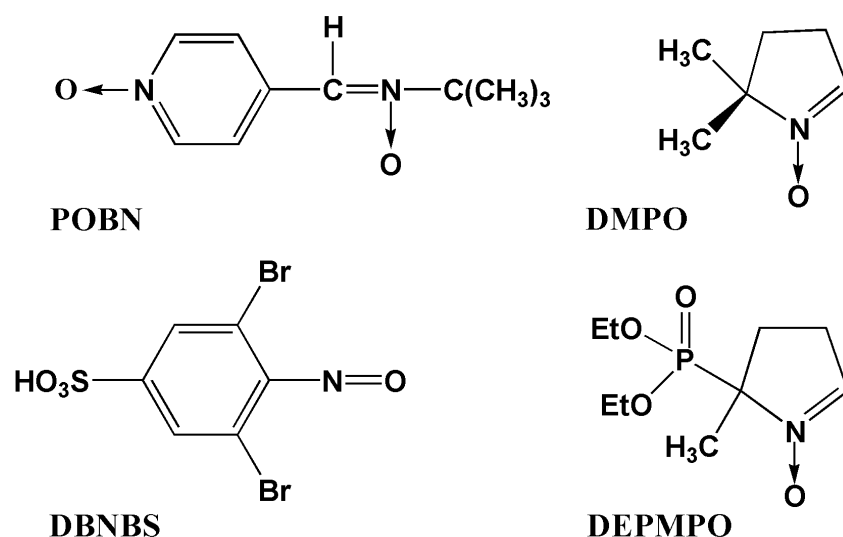
Fig. 4: Spin trap molecules POBN, DMPO, DBNBS, and DEPMPO.

The spin trap was prepared as an aqueous 1.0 M stock solution before use in the systems under investigation. These stock solutions were kept at -20°C (-70°C for DEPMPO) between the measurements. For the EPR measurements 10 µl of the stock solution was applied to the system of interest (water suspensions of the polymers, cathode or anode of the *in situ* EPR fuel cell).

In order to verify obtained hyperfine coupling constants obtained EPR spectra were simulated using WINEPR SimFonia program version 1.25 from the Bruker Analytische Messtechnik GmbH.

3.1.2 SQUID experiments

A Superconducting Quantum Interference Device (SQUID) consists of a closed superconducting loop, including one or two Josephson junctions in the loop's current path [112]. Because of the quantized state of the superconducting ring, and the extraordinary non-linear behavior of the Josephson junction, the SQUID is capable of resolving changes in external magnetic fields that approach 10^{-15} T, yet can be made to operate in fields as large as 7 T.

Although the SQUID in the Magnetic Property Measurement System (MPMS) is the source of the instrument's remarkable sensitivity, it does not detect directly the magnetic field from the sample. Instead, the sample moves through a system of superconducting detection coils which are connected to the SQUID with superconducting wires, allowing the current from the detection coils to inductively couple to the SQUID sensor. When properly configured, the SQUID electronics produces an output voltage which is strictly proportional to the current flowing in the SQUID input coil.

The highly sensitive SQUID magnetization measurements provide information about the magnetic properties of the samples and distinguish between diamagnetic, paramagnetic, antiferromagnetic and ferromagnetic or superparamagnetic states. In many cases the magnetic behavior is a superposition of more than one magnetic property [113]. In our samples, the diamagnetic part is mainly a property of the carbon framework and should thus be comparable with the diamagnetism of carbon black.

SQUID magnetization measurements were performed using a Quantum Design MPMS-5S instrument in the 0 to 6.5 T external magnetic field range and the 2 - 300 K temperature interval. Measurements were performed at a constant field varying the temperature or vice versa.

3.1.2.1 Relevant examples of magnetism in matter

Paramagnetism

Paramagnetic materials are those in which individual atoms, ions or molecules have some number of uncompensated spins and thus a permanent net spin magnetic moment. The key features for a paramagnet are that: 1) the dependence of magnetization on the applied

magnetic field is linear; 2) the produced line intersects zero; 3) the magnetization is reversible. Reversible means that the same curve is followed when going up in field as when going back down in field [114].

Pauli paramagnetism

It is usually seen in metals or other conductors. Conduction electrons have magnetic moments that can be aligned with an applied magnetic field. The key characteristics of Pauli paramagnetism are that the χ value is nearly independent of temperature and in most cases it has a very small positive value.

Curie paramagnetism

Two features are often used to determine the origin of the paramagnetism: the magnitude of χ and the temperature dependence of the susceptibility $\chi(T)$. A Curie-type paramagnet has a particular temperature dependence:

$$\chi(T) = \frac{C}{T} \qquad (3\text{-}9)$$

where C is a Curie constant given as:

$$C = b\rho_{eff}^2 N \qquad (3\text{-}10)$$

where ρ_{eff} is known as the effective magnetic moment, b is a universal constant, and N is the concentration of magnetic atoms with that moment. Thus, the constant C can be used to determine the product of the effective magnetic moment of an atom and the number of magnetic atoms present. The $1/T$ (or Curie) temperature dependence is a result of a competition between the force aligning the moments parallel to the field and the tendency for heat to disrupt the alignment. As the temperature increases, the associated increase in heat reduces the relative effect of the field.

Curie-Weiss paramagnetism

In addition to the interaction with the applied magnetic field, as it was in the case of Curie paramagnetism, there is an interaction between the magnetic moments on different atoms. This interaction between moments (exchange interaction) can help to align neighbouring moments in opposite directions. The Curie-Weiss susceptibility is given by:

$$\chi(T) = \frac{C}{T - \Theta} \qquad (3\text{-}11)$$

where Θ is called Curie-Weiss temperature. The Curie-Weiss Θ is related to the strength of the interaction between moments, and its sign depends on whether the interaction helps to align adjacent moments in the same direction or opposite to one another. Using the definition in equation (3-11), for $\Theta > 0$ the interaction helps to align adjacent moments in the same direction, and for $\Theta < 0$ the interaction helps to align adjacent moments opposite to each other. Another terminology is that for $\Theta > 0$ there is a net ferromagnetic interaction between moments, and for $\Theta < 0$ there is a net antiferromagnetic interaction between moments.

In the case of the ferromagnetic Θ, $T = \Theta$, also known as the Curie temperature (T_C), indicates the approximate location of a ferromagnetic transition. For an antiferromagnetic Θ, the system has an antiferromagnetic transition, known as the Néel transition (T_N), near $T = |\Theta|$.

Ferromagnetism

A ferromagnet has a spontaneous magnetization even in the absence of an applied field. All the magnetic moments lie along a single unique direction. In many ferromagnetic samples this is not true throughout the sample because of domains. In each domain there is a uniform magnetization, but the magnetization of each domain points in a different direction from its neighbours. Within the domain, the magnetic field is intense, but in a bulk sample the material will usually be unmagnetized because the many domains will themselves be randomly oriented with respect to one another. However, if a ferromagnet is placed in a strong enough external magnetic field, the domains will reorient in parallel with that field, and will remain reoriented when the field is turned off, thus creating a "permanent" magnet. This magnetization as a function of the external field is described by a hysteresis curve. As the temperature increases, thermal oscillation, or entropy, competes with the ferromagnetic tendency for spins to align. When the temperature rises beyond a certain point, called the Curie temperature, there is a second-order phase transition and the system can no longer maintain a spontaneous magnetization, although it still responds paramagnetically to an external field [115].

Superparamagnetism

If ferromagnetic particles are small enough, they will be single domain, because the energy cost of domain wall formation does not outweigh any saving in demagnetising energy. The magnetisation of a small, single-domain ferromagnetic particle is often constrained to lie parallel or antiparallel to a particular direction. Consider now a distribution of these small

particles in non-magnetic matrix and assume that the particles are separated far enough apart so that interparticle interactions can be neglected. At high temperatures the system will behave like a paramagnet, albeit one in which the independent moments are not atomic moments but large groups of moments, each group inside a ferromagnetic particle. The system is therefore called a superparamagnet. At high temperatures the moments on the particles are able to fluctuate rapidly. The fluctuations slow down as the sample is cooled. The system becomes static below the blocking temperature T_B, each magnetic particle appears to be locked into one of its two minima. If the particles in the superparamagnetic system have a range of sizes then they will "block" at different temperatures. Superparamagnetism is technologically important since many important recording materials are particulate [116].

Diamagnetism

Diamagnetic materials are materials in which the electron spin moments are compensated. For a diamagnetic substance, a magnetic field induces a magnetic moment which opposes the applied magnetic field that caused it [116]. The dependence of magnetization for diamagnets on the applied magnetic field is linear and reversible but has a negative slope. This means that χ is negative. When placed in a magnetic field, an extra torque is applied to the electron, resulting in an antiparallel alignment of the atomic moment. This accounts for the weak, negative magnetic susceptibility. Diamagnetism is found in all materials, however because it is so weak it can only be observed in materials that do not exhibit other forms of magnetism. Diamagnetism is also found in elements with unpaired electrons.

3.2   Theory description – the DFT approach

The basis for Density Functional Theory (DFT) is the proof by Hohenberg and Kohn that the ground state electronic energy is determined completely by the electron density $\rho(r_l)$ [117]. It is defined as the following multiple integral over the spin coordinates of all electrons and over all but one of the spatial variables [118]:

$$\rho(r_1) = N \int ... \int |\Psi(x_1, x_2, ... x_N)|^2 \, ds_1 dx_2 ... dx_N \qquad (3\text{-}12)$$

The significance of this is best illustrated by comparing to the wave function approach. A wave function for an N-electron system contains $3N$ coordinates, three for each electron (four if spin is included). The electron density is the square of the wave function, integrated over N-1 electron coordinates, it only depends on the three coordinates, independently of the number of electrons.

While the complexity of a wave function increases with the number of electrons, the electron density has the same number of variables, independently of the system size. $\rho(r_l)$ determines the probability of finding any of the N electrons within the volume element dr_l but with arbitrary spin, while the other N-1 electrons have arbitrary positions and spin in the state represented by Ψ.

Unlike the wave function, the electron density is an observable and can be measured experimentally, e.g. by X-ray diffraction. One of its important features is that at any position of an atom, $\rho(r)$ exhibits a maximum with a finite value, due to the attractive force exerted by the positive charges of the nuclei.

The main problem of DFT methods is that although it has been proven that the ground state electronic energy is determined completely by the electron density, the functional connecting these two quantities is not known. The goal is to design functionals relating the electron density to the energy. Comparing with the wave mechanics approach, the energy functional may be divided into three parts, the kinetic energy $T[\rho]$, attraction between the nuclei and electrons, $E_{ne}[\rho]$, and electron-electron repulsion, $E_{ee}[\rho]$. Furthermore, the $E_{ee}[\rho]$ term may be divided into a Coulomb and Exchange part, $J[\rho]$ and $K[\rho]$.

The foundation for the use of DFT methods in computational chemistry was the introduction of orbitals by Kohn and Sham (KS) [119]. The basic idea in the KS formalism is splitting the kinetic energy functional into two parts, one of which can be calculated exactly, and a small correlation term. The key to KS theory is thus the calculation of the kinetic energy

under the assumption of non-interacting electrons. In reality the electrons are interacting, however, the difference between the exact and kinetic energy and that calculated by assuming non-interacting orbitals is small. The remaining kinetic energy is absorbed into an exchange-correlation term, and a general DFT energy expression can be written as [120]:

$$E_{DFT}[\rho] = T_S[\rho] + E_{ne}[\rho] + J[\rho] + E_{XC}[\rho] \tag{3-13}$$

$T_S[\rho]$ is the exact kinetic energy functional and is given by the equation:

$$T_S[\rho] = \sum_{i=1}^{N} \left\langle \phi_i \mid -\frac{1}{2}\nabla^2 \mid \phi_i \right\rangle \tag{3-14}$$

$E_{ne}[\rho]$ is the nuclei-electron attraction functional given by:

$$E_{ne}[\rho] = -\sum_a \int \frac{Z_a \rho(r)}{|R_a - r|} dr \tag{3-15}$$

$J[\rho]$ is the Coulomb functional given by:

$$J[\rho] = \frac{1}{2}\iint \frac{\rho(r)\rho(r')}{|r-r'|} dr dr' \tag{3-16}$$

Using equation (3-13) the E_{XC} can be defined as a part which remains after subtraction of the non-interacting kinetic energy, and the E_{ne} and J potential terms.

$$E_{XC}[\rho] = (T[\rho] - T_S[\rho]) + (E_{ee}[\rho] - J[\rho]) = E_X[\rho] + E_C[\rho] \tag{3-17}$$

The first parenthesis term may be considered the kinetic correlation energy, while the second one contains both exchange and potential correlation energy. The exchange energy E_X is by far the largest contribution to E_{XC}.

The major problem in DFT is deriving suitable formulas for the exchange-correlation term. Since $J[\rho]$ and $E_{XC}[\rho]$ functionals depend on the total density, a determination of the orbitals involves an iterative sequence. The orbital orthogonality constraint may be enforced by the Lagrange method:

$$L[\rho] = E_{DFT}[\rho] - \sum_{ij}^{N} \lambda_{ij}[\langle \phi_i \mid \phi_j \rangle - \delta_{ij}] \tag{3-18}$$

Requiring the variation of L to vanish provides a set of equations involving an effective one-electron operators (h_{KS}).

$$h_{KS}\phi_j = \sum_j^N \lambda_{ij}\phi_j \tag{3-19}$$

Performing a unitary transformation which makes the matrix of the Lagrange multiplier diagonal, produces a set of canonical KS orbitals. The resulting pseudo-eigenvalue equations are known as the Kohn-Sham equations:

$$\left(-\frac{1}{2}\nabla^2 + \left\{-\sum_a \frac{Z_a}{|r-R_a|} + \int \frac{\rho(r')}{|r-r'|}dr' + V_{XC}(r)\right\}\right)\phi_i = \varepsilon_i\phi_i \qquad (3-20)$$

The potential $V_{XC}(r)$ is given as the derivative of the energy with respect to the density:

$$V_{XC}(r) = \frac{\delta E_{XC}[\rho]}{\delta\rho(r)} = \varepsilon_{XC}[\rho(r)] + \rho(r)\frac{\partial\varepsilon_{XC}(r)}{\partial\rho} \qquad (3-21)$$

If the exact $E_{XC}[\rho]$ was known, DFT would provide the exact total energy, including electron correlation. It is possible to prove that the exchange-correlation potential is a unique functional, valid for all systems, but an explicit functional form of this potential has been elusive. The difference between DFT methods is the choice of the functional form of the exchange-correlation energy. There is little guidance from theory how such functionals should be chosen, and consequently many different potentials have been proposed. Functional forms are often designed to have a certain limiting behavior (e.g., including the uniform electron gas limit) and fitting parameters to known accurate data. Which functional is the better will have to be settled by comparing the performance with experiments or high-level wave mechanics calculations.

Local Density Approximation (LDA)

At the center of the Local Density Approximation is the idea of a hypothetical uniform electron gas. This is a system in which electrons move on a positive background charge distribution such that the total ensemble is electrically neutral. It should be noted that this model system is pretty far from any realistic situation in atoms or molecules, which are usually characterized by rapidly varying densities. Central to this model is the assumption that we can write the exchange-correlation energy in a following way [118]:

$$E_{XC}^{LDA}[\rho] = \int \rho(r)\varepsilon_{XC}(\rho(r))dr \qquad (3-22)$$

Where $\varepsilon_{XC}(\rho(r))$ is the exchange-correlation energy per particle of a uniform electron gas of density $\rho(r)$. The exchange energy for a uniform electron gas is given by the Dirac formula [120]:

$$E_X^{LDA}[\rho] = -C_X \int \rho^{4/3}(r)dr \qquad (3-23)$$

$$\varepsilon_X^{LDA}[\rho] = -C_X\rho^{1/3} \qquad (3-24)$$

In the more general case, where the α and β spin densities are not equal, LDA has been virtually abandoned and replaced by the Local Spin Density Approximation (LSDA) (which is given as the sum of the individual spin densities raised to the 4/3 power). For closed-shell systems LSDA is equal to LDA.

The correlation energy ε_C of a uniform electron gas has been determined by Monte Carlo methods for a number of different densities. In order to use these results in DFT calculations, it is desirable to have a suitable analytic interpolation formula. This has been constructed by Vosko, Wilk, and Nusair (VWN) and is in general considered to be a very accurate fit [121].

In general, the LDA underestimates the exchange energy by $\approx 10\%$, thereby creating errors which are larger than the whole correlation energy. Electron correlation is furthermore overestimated, often by a factor close to 2, and bond strengths are as a consequence overestimated. Despite the simplicity of the fundamental assumptions, LDA methods are often found to provide results with an accuracy similar to that obtained by wave mechanics Hartree Fock (HF) methods.

Generalized Gradient Approximation (GGA)

Improvements over the LDA approach have to consider a non-uniform electron gas. A step in this direction is to make the exchange and correlation energies dependent not only on the electron density, but also on derivatives of the density. Such methods are known as Gradient Corrected or Generalized Gradient Approximation methods. GGA methods are also sometimes referred to as non-local methods, although this is somewhat misleading since the functionals depend only on the density and derivatives at a given point and not on a space volume. The GGA functionals can be generally written as [118]:

$$E_{XC}^{GGA}[\rho_\alpha, \rho_\beta] = \int f(\rho_\alpha, \rho_\beta, \nabla\rho_\alpha, \nabla\rho_\beta) dr \qquad (3\text{-}25)$$

In practice, E_{XC}^{GGA} is usually split into its exchange and correlation contribution:

$$E_{XC}^{GGA} = E_X^{GGA} + E_C^{GGA}, \qquad (3\text{-}26)$$

and approximations for the two terms are sought individually.

Gradient corrected methods usually perform much better than LSDA. In general it is found that GGA methods often give geometries and vibrational frequencies for stable molecules of the same or better quality than MP2, at a computational cost similar to HF. For systems containing multi-reference character, where MP2 fails badly, DFT methods are often found to generate results of a quality comparable to that obtained with coupled cluster methods [120].

The mostly used functionals employing this approach are the LYP correlation functional of Lee, Yang, and Parr, which includes both local and non-local terms [122], the PW91 Perdew and Wang's 1991 correlation functional [123], the B96 Becke's 1996 correlation

functional [124], the B88 exchange functional [125], the PW91 exchange functional [123] and some others.

Hybrid functionals

The exchange contributions are significantly larger in absolute numbers than the corresponding correlation effects. Therefore, an accurate expression, for the exchange functional in particular, is a prerequisite for obtaining meaningful results from density functional theory.

Since, the exact wave function in the case of non-interacting electrons is a single Slater determinant composed of KS orbitals, the exchange energy is exactly that given by HF theory [120]. If the KS orbitals are identical to the HF orbitals, the "exact" exchange is precisely the exchange energy calculated by HF wave mechanics methods.

$$E_X^{exact} = -\frac{1}{2}\sum_i^N\sum_j^N\left\langle \phi_i(r)\phi_j(r') \mid \frac{1}{|r-r'|} \mid \phi_j(r)\phi_i(r') \right\rangle \qquad (3\text{-}27)$$

A generalized solution may be defined by writing the exchange energy as a suitable combination of LSDA, exact exchange and a gradient corrected term. The correlation energy may similarly be taken as the LSDA formula plus a gradient corrected term.

The most prominent example of this class is B3LYP. This functional was employed in our calculations and is discussed in section 3.2.2. Among other DFT methods the hybrid functionals show the most satisfactory performance, sometimes with errors against the G2 set [126] of only slightly above 8.3 kJ mol^{-1}.

Plane waves basis set

The Kohn-Sham orbitals in equation (3-20) actually may be represented in terms of any complete basis set. Under certain circumstances, basis sets which do not comply with the LCAO scheme, i.e. plane waves, are employed in density functional calculations. The use of a plane wave basis set offers a number of advantages, including the simplicity of the basis functions, which make no preconceptions regarding the form of the solution, the absence of basis set superposition error, and the ability to efficiently calculate the forces on atoms. Plane waves are the solutions of the Schrödinger equation of a free particle and are simple exponential function of the general form [118]:

$$\eta^{pw} = \exp[ikr] \qquad (3\text{-}28)$$

Where the vector k is related to the momentum p of the wave through $p = \hbar k$. Plane waves are not centred at the nuclei but extended throughout space. They enjoy great

popularity in solid state physics and chemistry for which they are particularly adapted because they implicitly involve the concept of periodic boundary conditions.

The principle disadvantage of the use of a plane wave basis set is the number of basis functions required to accurately represent the Kohn-Sham orbitals. This problem may be reduced by the use of pseudopotentials, but several hundred basis functions per atom must still be used, compared with a few tens of basis functions for some atom-centered basis sets [127].

First-principles total energy calculations within the DFT framework were performed in our study. As mentioned in the INTRODUCTION, two geometrical models were used to study adsorption: the slab geometry and the cluster geometry. The former was studied using the VASP program; the latter using Gaussian 98.

3.2.1   VASP calculations

The calculations were carried out with the Vienna Ab-Initio Simulation Package (VASP) [128 - 130], which is an efficient density functional theory based code for systems with periodic boundary conditions.

The VASP represents the electron-ion core interaction via Blöchl's Projector Augmented Wave (PAW) approach [131, 132]. Generally, the PAW potentials are more accurate than the Ultra-Soft (US) pseudopotentials because the radial cutoffs (core radii) are smaller than the radii used for the US pseudopotentials, and because the PAW potentials reconstruct the exact valence wave function with all nodes in the core region. The PAW method yields converged total energy differences with a modest plane-wave basis set. The VWN [121] form of the local density approximation was used, in combination with the PW91 functional for the GGA [123]. In all cases, the plane-wave expansion was truncated at a cutoff energy of 400 eV, and a grid of $5 \times 5 \times 1$ Monkhorst-Pack special k-points was used to perform the Brillouin-zone integrations. These settings were found to give binding energies converged to within 0.02 eV with a minimum of computational cost. Adsorption energies were calculated as the difference between the energy of the composite system and the sum of the energies of the clean surface and uncoordinated adsorbate. For example, the chemisorption energy of atomic oxygen was calculated from:

$$E_{ads} = E_{Pt-O} - (E_O + E_{Pt}) \qquad (3-29)$$

where E_O, E_{Pt}, and E_{Pt-O} are the total energies of free O, Pt, and Pt-O.

The surfaces were modeled as four-layer slabs having four atoms in each layer, separated by five "layers of vacuum". All calculations were performed at the equilibrium lattice constant of 2.82 Å as found from the VASP geometry optimization. Pt atoms in the first layer were allowed to relax in the direction perpendicular to the surface. Fig. 5 shows three unit cells with adsorbed O_2 molecules repeated in x direction.
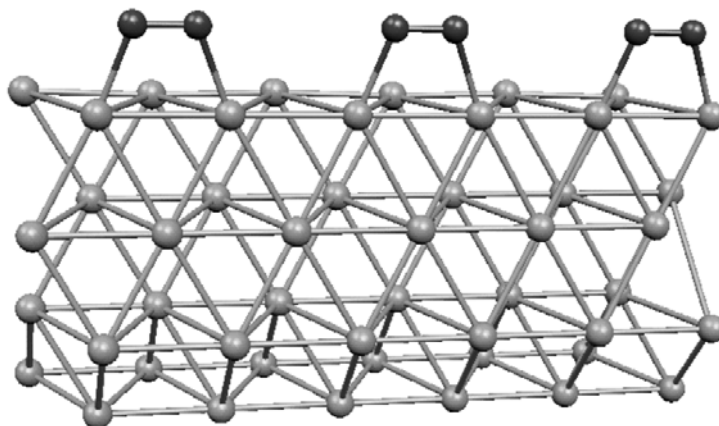
Fig. 5: 3 unit cells with adsorbed O_2 molecules repeated in x direction. The oxygen molecule is bound in the bridge position between two Pt atoms on the (111) surface.

3.2.2 Gaussian 98 calculations

In this part of the study we used a cluster model to simulate the interactions of oxygen containing species with different sites of the Pt(111) surface in presence of an applied electric field. Optimized geometries of adsorbed species were taken from the VASP results and re-optimized for the case of the Pt_9(111)-adsorbate system. The cluster geometry was fixed as in bulk platinum, with an experimental Pt-Pt distance of 2.77 Å. Fig. 6 shows the geometry of an adsorbed oxygen molecule at the hollow position on the Pt_9(111) cluster. The small size of the cluster provides only a limited representation of the metal conduction band. Therefore, one does not expect to obtain extremely accurate results. However, common trends, in particular in relation to bond distances and vibration properties, and the effect of an electric field on the binding energy should be sufficiently accurate to produce meaningful results [80, 133].
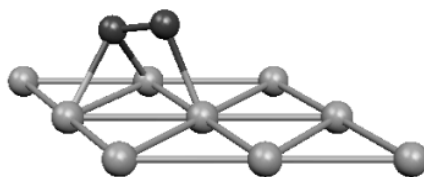
Fig. 6: Oxygen molecule adsorbed at the hollow position of a Pt_9(111) cluster.

We employed a 6-311G** basis set for the O and H atoms and a LANL2DZ, double-ς, basis set with an effective core potential derived by Hay and Wadt [134] for the Pt atoms as implemented in Gaussian 98 [135]. Using these basis sets and frozen core potentials, *ab initio* cluster model calculations were carried out in the framework of the B3LYP Density Functional Theory method with spin-unrestricted orbitals. The B3LYP hybrid method is known to provide very good results for transition-metal containing compounds including surface cluster models [136, 137]. The B3LYP functional is based on Becke's 3-parameter Adiabatic Connection Method (ACM) approach, and consists of a combination of Slater [138], HF [139], and B88 [125] exchange, with the VWN local [121] and the LYP [122, 140] non-local correlation functionals.

In order to investigate the electric field dependence of the properties of the adsorbed species, an electric field was applied to the system in a direction perpendicular to the Pt surface. Electric field intensities of -0.0100, -0.0075, -0.0050, -0.0025, 0.0000, 0.0025, 0.0050, 0.0075, 0.0100 a.u. were considered, and the sign of the electric field was chosen in such a way that a more negative field corresponds to a more negative adsorbate and more positive Pt substrate. The electric potential is the relevant experimental parameter, which determines the electrochemical properties of adsorbates, as reflected in particular in their vibrational characteristics [81, 141, 142]. Some of these vibrational characteristics may be measured experimentally by Surface-Enhanced Raman Spectroscopy (SERS), Sum Frequency Generation (SFG) and Infrared Reflectance-Absorption Spectroscopy (IRAS) [143 - 145]. Geometries of the adsorbates were optimized for each field using analytical gradients.

In general, the theoretical DFT studies give bond distances and vibrational frequencies close to the experimental values, both for slab and cluster models of the surface [75, 96, 97]. However, clusters of ≈ 28 atoms or more might be required for an accurate description of binding energies [74]. The adsorption energy is generally more sensitive to the size and shape of the cluster than the distances are, as the energy levels of the cluster orbitals play an important role in the bonding. However, in some cases, clusters as small as Pt_2 or even single Pt atoms provide reasonable estimates of metal-adsorbate bond strengths on extended Pt surfaces [68].

Chapter 4

4 RESULTS AND DISCUSSION

In this chapter experimental and theoretical results are presented. The experimental data are discussed in the first two subchapters, whereas the calculational results on oxygen and oxygen containing species adsorbed on Pt surfaces under conditions relevant for fuel cells are discussed at the end of the chapter.

4.1 Fuel cell components

The studies of the fuel cell components, i.e. electrodes which are GDEs based on the plane weave carbon with different Pt loadings, Vulcan XC-72 with different Pt content, pure Pt black, and membranes are discussed.

In GDEs Pt particles with the size of approximately 2 nm and the surface area of 140 m^2 g^{-1} are supported on carbon material Vulcan XC-72 with the surface area of 254 m^2 g^{-1} and the particle size of 30 nm which is then supported on the plane weave carbon (surface area 0.086 m^2 g^{-1}). In our investigations we studied 0.0 - 2.0 mg cm^{-2} Pt loadings that corresponds to 0 - 20% Pt content in Vulcan XC-72 material. Pt black has the particle size of 10 nm and the surface area of 28 m^2 g^{-1}. All these materials were purchased from E-TEK.

4.1.1 Gas Diffusion Electrodes

A typical EPR spectrum from the GDE is shown in Fig. 7. The signal was identified to originate from electrode material and belongs to electrons in carbon [146]. It was shown earlier that carbon materials have unpaired electrons which can be detected by means of EPR techniques. The concentration of free electron spins for carbon materials often lies in the range of 10^{19} - 10^{20} spins g^{-1} [146 - 148].
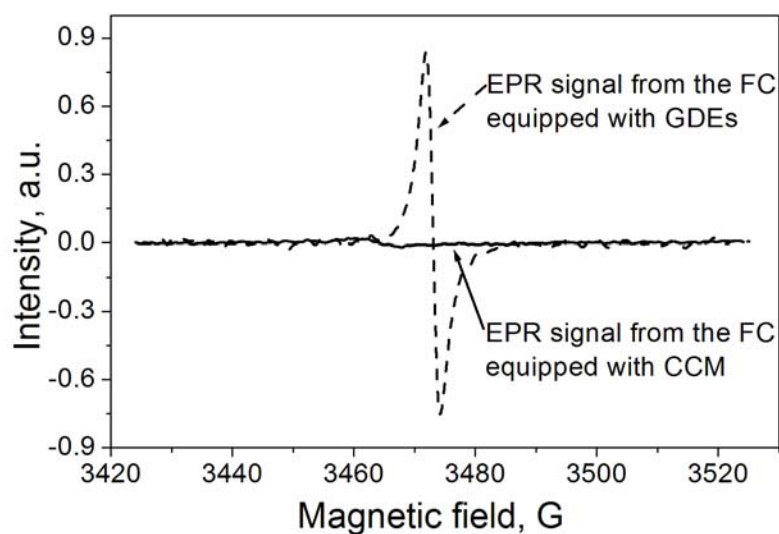
Fig. 7: EPR signal from the *in situ* fuel cell equipped with GDEs or CCM (that is a membrane with Pt electrodes deposited on both sides). In the case of the GDEs the signal belongs to electrode material.

The signal has a *g* value of 2.0030 and a peak-to-peak line width of approximately 3 G which is also typical for carbons materials (1.9950 - 2.0031) [146, 149], and it is almost symmetric. The small value for the line width and the small deviation of the *g* value from the free electron spin *g* value suggest that the observed spins originate not from transition metal magnetic impurities but from carbon-inherited spin species in the carbon material [150].
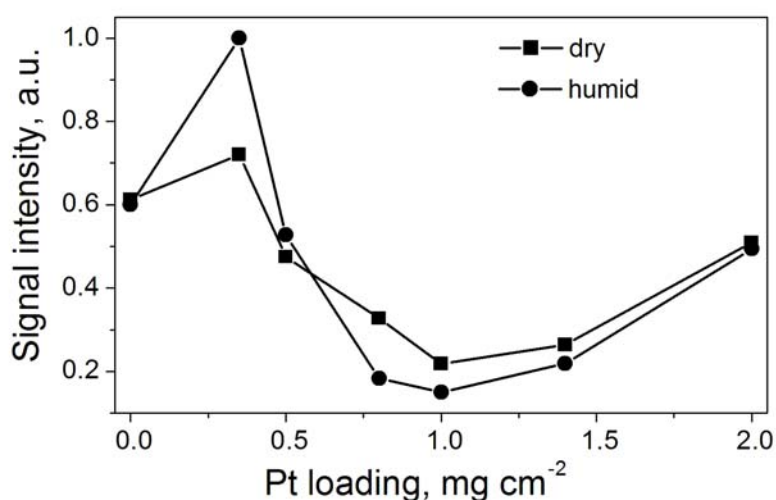
Fig. 8: EPR signal intensity as a function of Pt loading in dry and humid air.

To investigate how the signal depends on the nature of the material spectra from GDEs with different Pt loadings were recorded at room temperature. Fig. 8 shows the signal

intensity as a function of Pt loading and air humidity (humid air: air saturated with water vapour at 25°C).

The plane weave carbon itself without Pt has a significant number of unpaired electrons. With increasing Pt loading the signal intensity grows and has a maximum at a Pt loading of 0.35 mg cm^{-2} (Fig. 8). Then the intensity goes down.

The signal intensity shows a considerable dependence on the Pt loading and on the air humidity. The sample with 0.35 mg cm^{-2} Pt shows a more than five times greater spin content than the sample with 1.00 mg cm^{-2} Pt. For the samples with 0.35 and 0.50 mg cm^{-2} Pt loadings the signal grows in humid air conditions, whereas for the other materials water presence reduces the intensity.

Under fuel cell running conditions water is an inseparable and very important part of the system. Its presence has a great influence on the EPR signal from electrode material. Water in the sample can significantly reduce the sensitivity of an EPR spectrometer and cause a signal decrease. Another potential influence lies in the adsorption of water molecules on the catalyst surface and interaction with surface species. At present it is not clear what the interaction of water with the platinum clusters is that leads to the reduction of the signal. Water vapour increases the number of unpaired electrons in the system for the sample containing 0.35 and 0.50 mg cm^{-2} Pt, but for higher Pt loadings the intensity goes down in humid air.

Fig. 9 depicts the signal line width behavior as a function of temperature for GDEs with no Pt, and with 0.35 and 1.00 mg cm^{-2} Pt loadings.
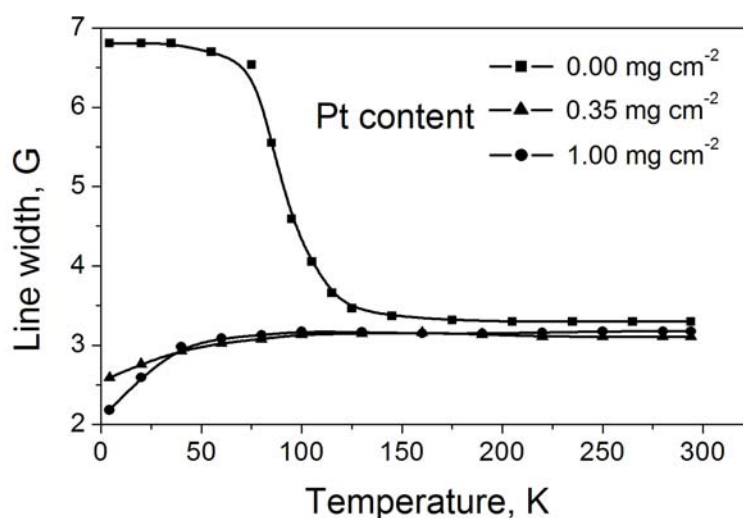
Fig. 9: Peak-to-peak line width for GDEs with no Pt, and with 0.35 and 1.00 mg cm^{-2} Pt loadings.

Samples with and without Pt show essentially different line width behavior as a function of temperature. The GDE carbon material without Pt has a broad line at temperatures up to 55 K. The signal narrows with increasing temperature from 6.808 G to 3.300 G. Line widths from the samples with Pt do not depend so strongly on the temperature and broaden with increase of temperature. For GDEs with Pt it becomes broader and reaches 3.176 G and 3.110 G for 0.35 and 1.00 mg cm^{-2} Pt loadings, respectively, at high temperatures. From 150 K up to room temperatures the line widths from all three samples are relatively close.

This behavior can be explained in terms of changing the nature of radical centers. In the case of carbon material its delocalized electrons in microcrystalline regions are responsible for the EPR signal [146], but in the presence of Pt clusters spins migrate to the surface and can be captured by these clusters, thus it is likely that electrons locate to a large extent in the Pt clusters. At low Pt loadings there are a number of small Pt clusters on the surface, and each cluster may have an unpaired electron. With increasing Pt loading particles grow and can merge. So its number decreases and unpaired spins recombine. In general, this leads to a decrease of unpaired spins and thus of signal intensity.

In order to study magnetic properties of the GDE material SQUID measurements were carried out on samples containing 0.00, 0.80 and 2.00 mg cm^{-2} Pt. It is expected that pure Pt shows Pauli paramagnetism [151]. For carbon materials, e.g. graphite, fullerenes, carbon nanotubes, etc. the susceptibility is defined mostly by the diamagnetic component [152, 153].

The magnetic susceptibility of the diverse forms of carbon strongly depends on the presence or absence of aromatic-like π electrons. The diamagnetism of the C^{4+} ion is -1.2×10^{-8} emu g^{-1} [154]. Diamond has a reported susceptibility of $\chi \approx -4.9 \times 10^{-7}$ emu g^{-1} due to diamagnetic contributions from core and valence electrons, and a Van Vleck paramagnetic term [155]. Graphite has an anisotropic diamagnetic susceptibility [156]. Bulk graphite has a c-axis diamagnetic susceptibility of $\chi_\perp = -(22 - 50) \times 10^{-6}$ emu g^{-1} which is caused by the itinerant π electrons in a semimetallic structure. It is very sensitive to the details of the band structure, and therefore to the degree of graphitisation, and it has been used as a tool to characterize graphitic materials [157]. Magnetic properties are different for the hexagonal and rhombohedral forms [158], the rhombohedral form being more anisotropic. As a matter of fact, it has been found theoretically, from an *ab initio* study, that the total energy of the rhombohedral graphite is slightly larger, by 0.11 meV atom^{-1}, than that of the hexagonal graphite [159]; this can explain why the rhombohedral phase is only observed to exist in combination with the hexagonal phase and in relatively smaller percentages. It is usually accepted that when the magnetic field is applied parallel to the basal plane, the graphite

susceptibility is also diamagnetic: $\chi_\parallel = -5 \times 10^{-7}$ emu g^{-1}. However, there is experimental evidence that this component is paramagnetic $\chi_\parallel = 2 \times 10^{-6}$ emu g^{-1} [156]. Negative experimental values of the in-plane susceptibility can be due to sample misalignment, since the c-axis component is strongly diamagnetic. Thorough experiments show that the low-field dependence of the moment on the field is non-linear not only for graphite and fullerene C_{60} [156, 160], but also for diamond, and carbon nanotubes [160]. The magnetic susceptibilities of C_{60} ($\chi \approx -3.5 \times 10^{-7}$ emu g^{-1}) and C_{70} ($\chi \approx -5.9 \times 10^{-7}$ emu g^{-1}) have been also measured [161, 162]. The small values compared with that of graphite are ascribed to an accidental cancellation between a diamagnetic and paramagnetic term.

However, it is known that electronic properties of finite graphene sheets are drastically different from that of bulk graphite [163]. If graphite has a stepped surface, a localized state at the Fermi level appears, which is caused by the cut-off graphene layer and is localized near the step. For the nanosized graphite edge states play a leading role. The edge of a graphite sheet can be described as a combination of two types of edge shapes: zigzag and armchair shapes for a graphene sheet. As the edge states produce a peak at the Fermi level, they contribute to the Pauli paramagnetic susceptibility which competes with the orbital diamagnetism: for nanographite ribbons with zigzag edges a low temperature Curie-like behavior changes to a diamagnetic behavior at higher temperatures [164].

We studied magnetic properties of the GDE material with different Pt loadings. Fig. 10 shows the magnetization of the GDE material as a function of applied magnetic field at 2.0 K.
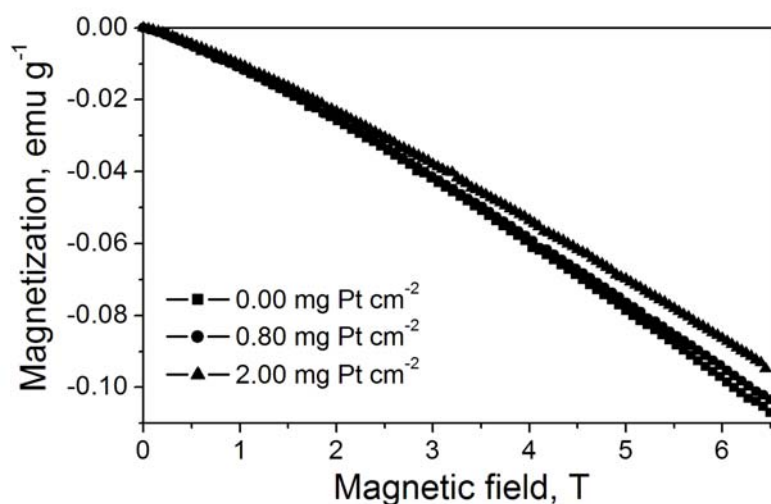
Fig. 10: Magnetic field dependence of the magnetization at 2.0 K for GDEs with various Pt loadings.

The magnetization curves show the absence of residual magnetization at $B = 0$ T and $T = 2.0$ K, suggesting the absence of ferromagnetic impurities. As shown in Fig. 10, the feature of magnetization curves at $T = 2.0$ K can be explained with the summation of a linear field-dependent term with a negative slope and a Brillouin-curve-type positive term [116, 150]. The linear term is associated with the combination of core diamagnetism, orbital diamagnetism, and Pauli paramagnetism. The Brillouin-curve-type term is explained with localized magnetic moments of $S = 1/2$. With increasing Pt loadings the negative term contribution associated with the diamagnetism of the plane weave carbon decreases and the magnetization becomes less negative at high fields.

The magnetic susceptibility is defined as:

$$\chi = M / B \qquad (4\text{-}1)$$

where M is the magnetization of the sample and B is the applied magnetic field.

Fig. 11 shows the magnetic susceptibility χ of the GDE material with various Pt loadings as a function of temperature measured by a constant magnetic field of 3300 G. The susceptibility decreases monotonically with decreasing temperature from 300 K to ~100 K [150, 163]. At around 65 K χ reveals a peak which can be assigned to the rhombohedral graphite [165]. At low temperatures below ~50 K, the susceptibility shows a Curie-like increase typical for graphite nanoparticles [163].
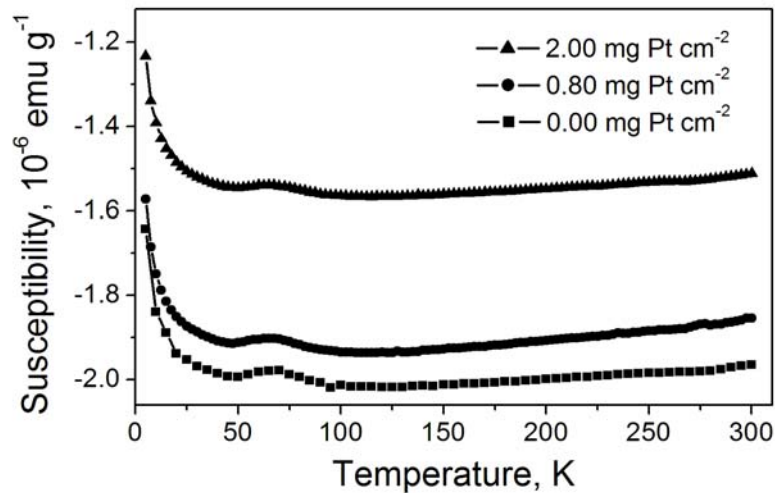
Fig. 11: Magnetic susceptibility of GDEs with various Pt loadings at a constant magnetic field of 3300 G.

With increasing Pt loading the susceptibility shifts to more positive values due to the additional Pauli paramagnetism from Pt. The total susceptibility is the sum of core

diamagnetism, Curie paramagnetism, orbital diamagnetism, and Pauli paramagnetism from the carbon material and Pauli paramagnetism from the Pt [163, 150]:

$$\chi = \chi_{core} + \chi_{Curie} + \chi_{orb} + \chi_{Pauli} \qquad (4\text{-}2)$$

The susceptibility can be described as a sum of temperature independent ($\chi_0 = \chi_{Core} + \chi_{orb} + \chi_{Pauli}$) and temperature dependent ($\chi(T) = \chi_{Curie}$) terms. A similar behavior of magnetic susceptibility is found for the graphitized nanodiamond [150] and for the pitch-based activated carbon fibers (ACF) with the dangling bond spins associated with 10 Å pores [166].

The magnetic susceptibility of the samples in the temperature range 4 - 50 K is well reproduced by the theoretical susceptibility $\chi(T)$ that includes paramagnetic and diamagnetic components:

$$\chi(T) = \chi_0 + \frac{C}{T - \Theta} \qquad (4\text{-}3)$$

where χ is a mass susceptibility of a sample (emu g^{-1}), χ_0 is a temperature independent part of the susceptibility (emu g^{-1}), C is a Curie constant (emu K g^{-1}), T is the temperature (K), and Θ is the Curie-Weiss temperature (K). Fitted parameters for the mass susceptibility equation are presented in Table 3.

Table 3: Fitted parameters for the magnetic susceptibility equation $\chi = \chi_0 + C/(T - \Theta)$ in temperature range 4 - 50 K for the GDEs with various Pt loadings.

Pt loading, mg cm^{-2}	χ_0, 10^{-6} emu g^{-1}	C, 10^{-6} emu K g^{-1}	Θ, K
0.00	-2.04	2.09	-0.33
0.80	-1.96	2.40	-1.13
2.00	-1.59	2.25	-1.30

Increase of the Pt loading leads to the reduction of the diamagnetic component of the total susceptibility due to the increasing term from the Pt Pauli paramagnetism; χ_0 increases. The concentration of the free spins increases slightly. From the Curie constants we estimated the concentration of free spins which is roughly 0.4×10^{18} spins g^{-1} (derived from equation (3-10)). The Curie-Weiss temperature Θ indicates that the adjacent moments try to align opposite to each other, there is a small net antiferromagnetic interaction in the sample [163].

The narrow EPR signal and the Curie tail in the temperature dependence of magnetic susceptibility, where the concentration of localized spins is estimated at 0.4×10^{18} spins g^{-1}

are considered to be assigned to localized spins associated with defects independent of the graphite π electrons [150].

4.1.2 Pt catalyst supported on Vulcan XC-72

Fig. 12 shows EPR spectra from the Pt catalyst supported on Vulcan XC-72 at room temperature. Without Pt the signal has a g value of 1.9980 and a peak-to-peak line width of approximately 78 G. With increasing Pt content the signal decreases and disappears at a Pt content of 20%. With increasing Pt content unpaired electrons tend to move to the surface of the carbon particles where they can be trapped by the platinum clusters, which is the main reason for the signal disappearance at high Pt content.
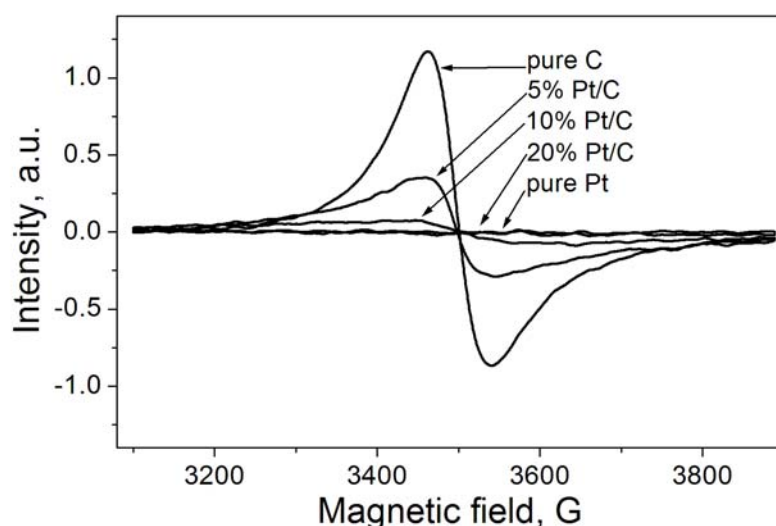
Fig. 12: EPR spectra from the Vulcan XC-72 material at room temperature and various Pt content.

For the preparation of GDEs with up to 2.0 mg cm^{-2} Pt loadings Vulcan XC-72 with 20 - 40% Pt content was used (according to the E-TEK declaration). As can be seen in Fig. 12 already for the 20% Pt content the EPR signal reduces dramatically in comparison to the pure Vulcan XC-72 material.

In order to understand better the nature of unpaired species measurements of magnetic properties of the Pt particles supported on the Vulcan XC-72 were performed using SQUID techniques.

Fig. 13 shows magnetization curves of the samples with various Pt content measured at 2.0 K. Increase of the applied magnetic field leads to the increase of magnetization for the

sample with Pt. However, this growth becomes slower as the Pt content decreases, and for Vulcan XC-72 without Pt the magnetization goes through a maximum and decreases at high fields.

As expected, pure Pt reveals Pauli paramagnetism arising from the fact that conduction electrons have magnetic moments and can be aligned with an applied field [151]. It is also known that isolated Pt nanoparticles having a diameter ranging from 2.3 to 3.8 nm can show superparamagnetic behavior in the magnetization process and enhanced magnetization compared to the paramagnetic moments in the bulk Pt [167]. For such Pt nanoparticles the magnetization can be as big as 0.9 emu g^{-1} at 5.5 T. All our samples have magnetic moments almost one order of magnitude smaller, giving proof of the fact that the superparamagnetic contribution is not predominant in magnetization and that the Pt black sample has magnetic properties similar to the bulk Pt.
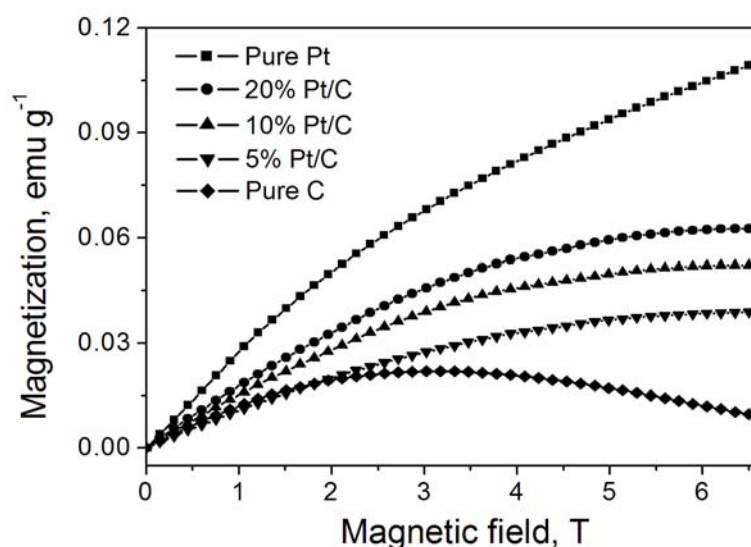
Fig. 13: Magnetic field dependence of the magnetization at 2.0 K for Vulcan XC-72 with various Pt content.

Magnetization components from the carbon material (core diamagnetism, Curie paramagnetism, orbital diamagnetism, and Pauli paramagnetism [150, 163]) admix additionally to the Pauli paramagnetism of the Pt black. This leads to the substantial reduction of the saturation magnetization with decreasing Pt content and simultaneous increase of Vulcan XC-72 content. Finally, for the pure Vulcan XC-72 the increase of the magnetization at low fields is followed by the negative slope of the magnetization curve, typical for diamagnetic materials, that is observed at high magnetic fields [156]. Increase of the magnetization is due to the increased Pauli paramagnetism in comparison to the GDE material. For the nanosized graphite edge states play a leading part in magnetic properties

[163]. The edge π states are suggested to be located between the π bonding and π^* antibonding bands as non-bonding states, where electrons in these states are localized around the peripheral region of a nanographene sheet. Consequently, the presence of the edge states on zigzag edges around the Fermi energy makes an additional contribution to the density of states, resulting in the enhancement in the Pauli paramagnetism. For graphite nanoparticles the Pauli paramagnetic susceptibility is one or two orders of magnitude larger than the Pauli contribution expected for bulk regular graphite, with $\chi_{Pauli} = 2 \times 10^{-8}$ emu g^{-1} [150]. Thus the diamagnetic component of the magnetization competes with the Pauli susceptibility in our samples [164]. For Vulcan XC-72 material the increase due to the Pauli term at low fields is suppressed by the growing negative diamagnetic term at high fields.

The temperature dependence of the susceptibility is presented in Fig. 14. It is known that at room temperature the magnetic susceptibility of bulk Pt amounts to 0.97×10^{-6} emu g^{-1} [168]. The total susceptibility is the sum of the Pauli paramagnetism from Pt and the core diamagnetism, Curie paramagnetism, orbital diamagnetism, and Pauli paramagnetism from the Vulcan XC-72 material as discussed before [150]. As it is known for the nanographites, the Pauli paramagnetic term can reveal Curie-like behavior at low temperatures [163, 164].
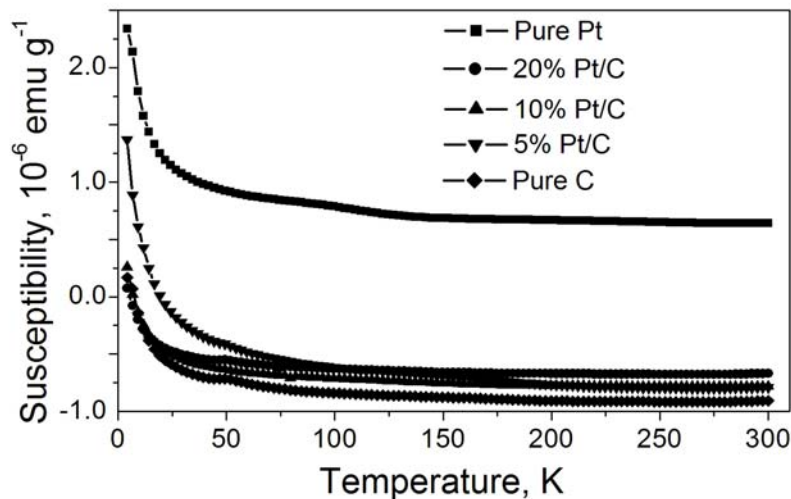
Fig. 14: Magnetic susceptibility of Vulcan XC-72 with various Pt content at a constant magnetic field of 3300 G. The order of the curves is the same as in the legend.

The magnetic susceptibility can be described by equation (4-3) in the whole temperature range 4 - 300 K. χ_0 is positive only for Pt black. The Pauli susceptibility of the Pt black reveals a Curie-like behavior at low temperatures, which can be attributed to the magnetic impurities [169]. The samples with carbon possess a negative temperature independent

susceptibility χ_0 arising from the carbon diamagnetic term. Increase of the Vulcan XC-72 content shifts the susceptibility curves towards more negative values. Fitted parameters for the mass susceptibility equation for the temperature range 4 - 50 K are presented in Table 4.

Table 4: Fitted parameters for the magnetic susceptibility equation $\chi = \chi_0 + C/(T - \Theta)$ in temperature range 4 - 50 K for the Vulcan XC-72 with various Pt content.

Pt on Vulcan XC-72	χ_0, 10^{-6} emu g^{-1}	C, 10^{-6} emu K g^{-1}	Θ, K
only Pt	0.60	20.00	-5.04
20% Pt	-0.69	6.19	-3.81
10% Pt	-0.80	8.56	-3.80
5% Pt	-0.79	20.00	-4.92
only Vulcan XC-72	-0.97	10.00	-6.00

The concentration of the free spins is estimated to 0.40×10^{19} spins g^{-1} (derived from equation (3-10)) for the Pt black. Pt on Vulcan XC-72 system has 0.12×10^{19} spins g^{-1}, 0.17×10^{19} spins g^{-1}, and 0.40×10^{19} spins g^{-1} for 20%, 10%, and 5% Pt, respectively. Vulcan XC-72 material has 0.20×10^{19} spins g^{-1}. The Curie-Weiss temperature Θ is slightly more negative in comparison to the GDE samples. As it was for the GDE material, Θ indicates that the adjacent moments try to align antiparallel to each other, there is a net antiferromagnetic interaction in the sample. The antiferromagnetic coupling is predicted for the nanocarbons with the zigzag edges, where the presence of almost flat bands leads to the electron-electron interactions which can lead to spontaneous magnetic ordering in nanometer-scale fragments of graphite [163].

The concentration of the free spins in the Pt/Vulcan XC-72 system is approximately one order of magnitude higher in comparison to the GDE material. The broad EPR signal is considered to be assigned to π electron spins, since the graphite electronic structure around the Fermi level is governed by π electron bands [150]. Taking into consideration the discontinuous shape at edge lines formed by crossing adjacent graphene sheets, graphene sheets in nanographite particle have open π bond edges. With increasing Pt content, Pt clusters tend to attach to such defects on Vulcan XC-72 nanoparticles, thus decreasing the concentration of free spins as can be seen for 20% Pt on Vulcan XC-72. However, in the GDEs, Pt/Vulcan XC-72 is present only as a small fraction (~1 wt%), and magnetic properties

of the system are determined to a large extent by the GDE basic component – the plane weave carbon as can be seen in section 4.1.1.

4.1.3   Membranes

As membranes, Nafion$^®$ 115 and different polyaryl-blend covalently (1025 with composition: sPEKH (67.3 wt%), PSU (32.7 wt%), and 1,4-diiodobutane crosslinker), ionically (504H with composition: sPEKH (91.8 wt%), PBI (4.1 wt%), PSU-C(OH)(4-diethylaminophenyl)$_2$ (4.1 wt%)) or covalent-ionically (1028 with composition: sPEKH (76 wt%), PSU (11.4 wt%), PSU-[C(OH)-CH3(4-pyridyl)]$_{1.5}$ (12.6 wt%)) cross-linked membranes, further quoted as F-free membranes, were employed. Details of preparation and electrochemical properties are described by Kerres *et al.* [170]. The novel membranes show promising chemical and thermal stability, good proton conductivity, and good performance in a direct methanol fuel cell due to reduced CH_3OH penetration.

Another type of ionically cross-linked membranes 1273, 1274 (composition: sPEKH, PBI, radical scavenger) [171] with improved stability against radical degradation was also studied. Details about radical scavenger's nature and its influence on radical formation are discussed later in this chapter. 1272 membrane was prepared analogically to the 1273 membrane, but without addition of a radical scavenger.

4.1.3.1   Degradation of membrane components

The F-free membranes can be fabricated from various polymers or their mixtures. In Fig. 2 only a few polymers used in membrane preparation were shown. However, for fuel cell applications the polymers should have some indispensable properties. Among them are the proton conductivity, mechanical, thermal, and chemical stability and some others (see section 2.1.2.1). As a general rule membranes that we use in our studies consist of several components in order to improve their essential properties. Most of the employed membranes are prepared on the basis of the following three components: sPEKH, PBI, and A 501 (Fig. 15).
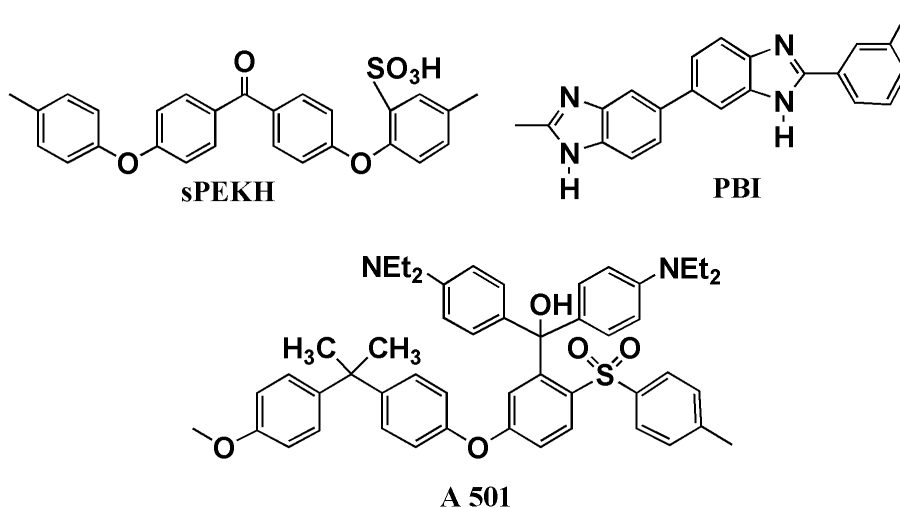
Fig. 15: Components used in membrane preparation.

Membranes based on sPEKH are promising for fuel cell applications as they possess good thermal stability and mechanical properties, and the proton conductivity can be controlled by the degree of sulfonation [172]. The sPEKH membranes with a degree of sulfonation of around 50% exhibit performances comparable to or exceeding that of Nafion$^{®}$ due to lower methanol crossover, but the operating temperature must be limited to < 65°C. Membranes with high degrees of sulfonation experience huge swelling at higher temperatures (80°C) and undergo failure. The performance of the sPEKH membranes could be improved further by blending with other polymers such as PSU, PBI, and some others [170], or by incorporating hydrated inorganic oxides such as SiO_2 [19], which can suppress the swelling behavior and increase the operating temperature [172].

PBI is a thermally resistant and insulating material. However, the sulfonated PBI which is a proton conductor can be prepared by sulfuric acid treatment on pre-formed PBI membranes [173]. The proton conductivity is not sufficiently high since the protonation of nitrogen in the imidazolium ring lowers the proton mobility. However, introduction of the PBI into blend membranes improves their mechanical and thermal properties and should be considered for the membrane development in the future [14]. Its presence considerably increases the thermal stability of membranes which are used in fuel cells operating at temperatures as high as 185°C [174]. In ionically cross-linked membranes the PBI is used as a basic component [170, 171].

A 501 material is based on a PSU polymer. PSUs are chemically stable, main-chain arylene polymers with broad applications as basis materials for both porous and dense polymeric membranes [20]. Sulfonation with chlorosulfonic acid or the SO_3/triethylphosphate complex leads to sulfonated PSU, which can be used as a cation-exchange membrane [175]. Membranes based on pure PSU are known to be very brittle. However, covalently cross-

linked blend membranes from sulfinated PSU with sulfonated sPEKH show a markedly reduced dry-brittleness, compared to covalently cross-linked blend membranes from the sulfinated PSU and sulfonated PSU [170]. For the preparation of the A 501 polymer the lithiated PSU was mixed with 4,4′-bis-(diethylamino)benzophenone as described by Kerres *et al.* [170]. In ionically cross-linked membranes the A 501 polymer is used as a basic component [170, 171].

It was of great interest for us to study degradation aspects of these species to make some predictions about their behavior and stability in membranes prior to the degradation studies of the membranes itself. These studies are performed *ex situ* using hydrogen peroxide as a source of $^{\bullet}$OH radicals which are known to be the most important degradation agents in low temperature fuel cells [29, 34].

The polymers of interest in pure form are powders which are almost insoluble in water at room temperatures. In order to make them accessible to $^{\bullet}$OH radical attack water suspensions were prepared. To the water suspension hydrogen peroxide and POBN spin trap were added subsequently (to 20 μl of the suspension 10 μl of 3% H_2O_2 and 10 μl of 1 M POBN solution were added). 10 μl of this mixture was filled into a quartz ESR tube and subsequently irradiated with UV light for two minutes. Hydrogen peroxide is unstable under UV light irradiation and decays into two $^{\bullet}$OH radicals [24]. These react with polymer molecules in the suspension to form different radicals on polymer surface. The POBN spin trap molecules react with the formed organic radicals ($^{\bullet}$R) to form POBN radical adducts.
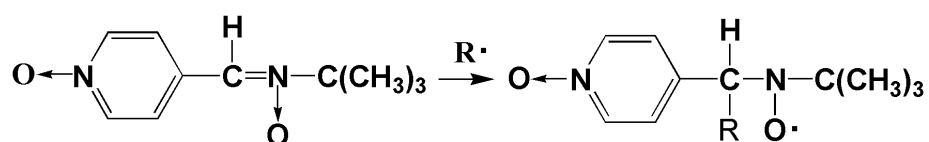
All three samples were treated equally and EPR spectra were recorded under identical conditions. As it will be shown the studied polymers show different behavior in radical formation processes. Possible reasons for this and consequences for the fuel cells are also discussed.

The degradation of sPEKH is considered first. Fig. 16 shows the spectrum from the POBN-$^{\bullet}$sPEKH adduct recorded after two minutes of the UV light irradiation. The signal from the POBN-$^{\bullet}$sPEKH radicals has a very low intensity. In the experimental time range sPEKH is quite stable against $^{\bullet}$OH radical attack and does not undergo degradation to a large extent. However, one should utilize such data very carefully.
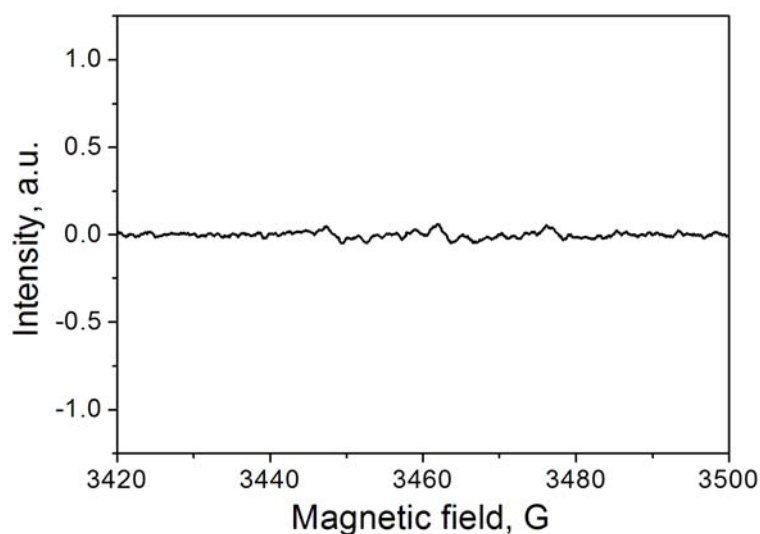
Fig. 16: EPR spectrum of the radical adduct POBN-•sPEKH in water suspension.

Experimental conditions do not reproduce conditions in a real fuel cell and the polymer is not in contact with a catalyst where radical species can be formed during the oxygen reduction in a working fuel cell, although the possible presence of •OH radicals is provided by the H_2O_2 decomposition. One should also keep in mind that the employed sPEKH polymer is water insoluble and the surface of polymer particles could be not or very weakly moistened, so the access of •OH radicals to the polymer is hindered. Extensive previous studies of the degradation aspects of the monomers used in sPEKH and PSU polymers preparation revealed that •OH radicals react with the dissolved molecules causing their degradation [24].
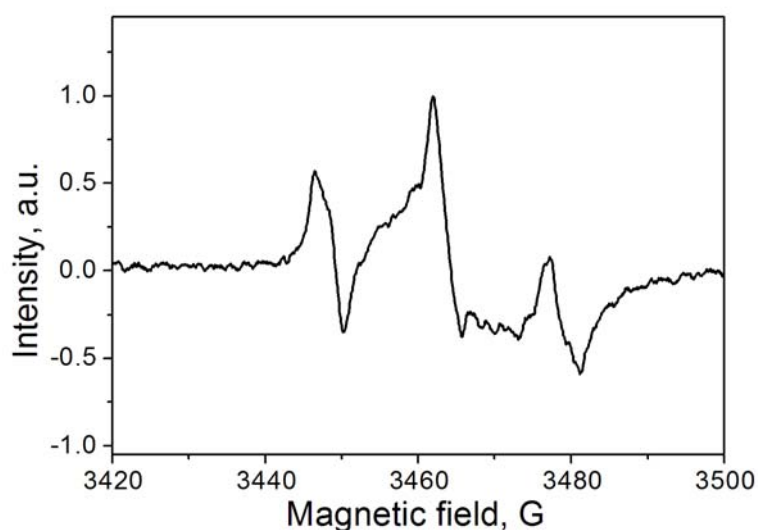
Fig. 17: EPR spectrum of the radical adduct POBN-•PBI in water suspension.

In contrast to the sPEKH, the PBI polymer reveals a distinct anisotropic signal from the POBN-•PBI radicals (Fig. 17). The spectrum consists of the three lines due to the splitting of the ^{14}N nucleus in the POBN molecule. The anisotropy can be explained in terms of the restricted mobility of the radicals because they are bonded to the water insoluble PBI polymer particles. An EPR signal implies that the PBI polymer is labile towards radical degradation. The •OH radicals can reach the polymer surface and attack it to form different organic radicals. The POBN molecules react with these radicals under formation of immobilized POBN-•PBI adducts.

The studies of the A 501 polymer degradation in water suspensions in the presence of POBN result in the spectrum shown in Fig. 18. The spectrum has narrow lines corresponding to the spitting of the ^{14}N nucleus and subsequent splitting of the ^{1}H nucleus in the POBN molecule typical for the POBN adducts with the C-centered organic radicals [176, 177].
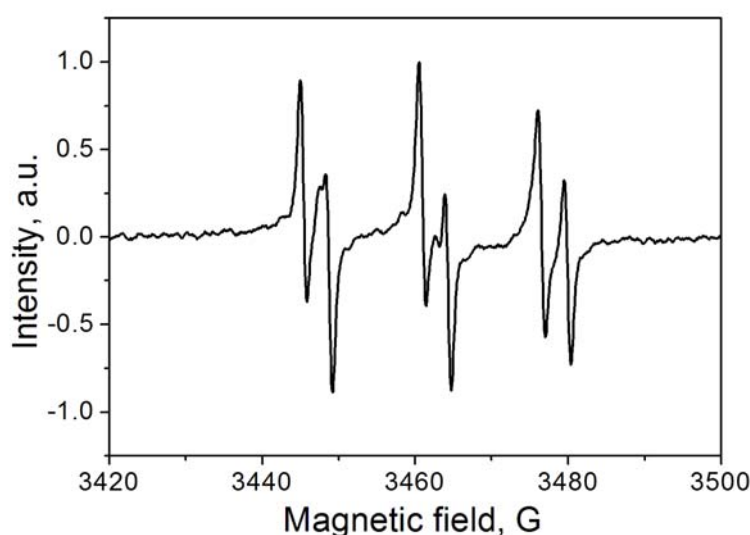
Fig. 18: EPR spectrum of the radical adduct POBN-•A 501 in water suspension.

In contrast to POBN-•PBI radicals, POBN-•A 501 adducts have much narrower lines indicating that the anisotropy is averaged out. The formed POBN-•A 501 radicals are mobile in the system. The A 501 polymer is accessible for •OH radicals even though it is not water soluble.

In general, studies of membrane components demonstrate that •OH radicals formed at the cathode side of the fuel cell are dangerous and can manifest their destructive nature by destroying the membrane material. In the present *ex situ* studies we were able to demonstrate the formation of organic radicals via •OH radical attack for the PBI and A 501 polymers, but

the sPEKH polymer revealed only a weak EPR signal. Previous studies of the system imply that sPEKH should also be involved in reactions with •OH radicals [24]. The observed weak signal can be explained in terms of poor accessibility of the water insoluble polymer particles for the •OH radicals. However, it is well known that in a working fuel cell the membrane is saturated with water and the polymer is accessible for the •OH radicals, at least in the hydrophilic regions [178], and can be attacked. In view of this, in order to increase the long term stability, polymers with improved stability against radical attack should be employed in membrane manufacturing for low temperature fuel cells. One of the attempts to diminish the membrane radical degradation is discussed in section 4.2.3.2.

The applied spin trapping technique is proved to be suitable to investigate the degradation of membrane components via radicals and will be utilized further to study membrane degradation *in situ* in a working fuel cell.

4.2 *In situ* fuel cell

A miniature fuel cell which can operate in a resonator of an X-band EPR spectrometer (maximum diameter 11 mm) was constructed [179]. Some indispensable requirements to fuel cell material are:

- inertness and stability;

- low dielectric losses under fuel cell running conditions.

According to these requirements Teflon was chosen as a body material for the cell. Despite some very useful properties Teflon has also a disadvantage: the material is relatively soft and cannot be pressed too hard.

The *in situ* fuel cell consists of two half-cylinders (Fig. 19).

1. Teflon half-cylinder (body)
2. Gas channel
3. Gas distribution (Pt mesh)
4. E-TEK Gas Diffusion Electrode
5. Polymer electrolyte membrane
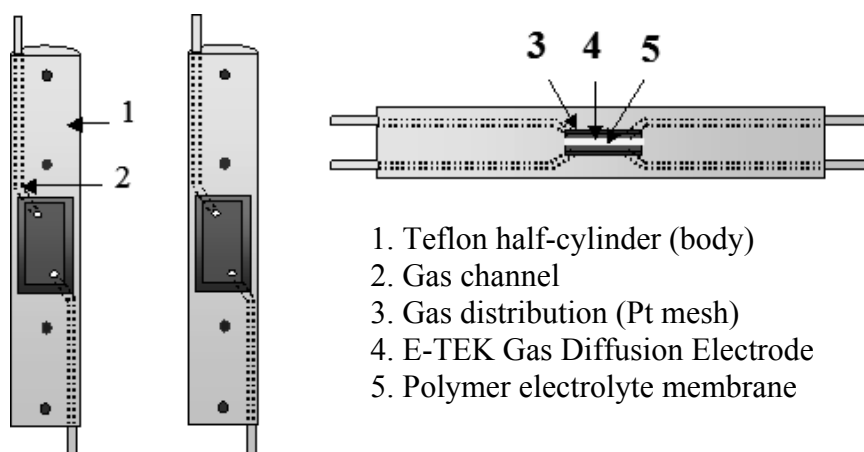
Fig. 19: Schematic drawing of the *in situ* fuel cell.

Each half-cylinder has an indentation where the active part of the fuel cell is situated. This active part includes GDEs, polymer electrolyte membrane, and Pt mesh as a spacer to allow gas distribution and at the same time provides electrical contact.

A second type of experiments was performed with CCMs. For the CCM production the dry Pt powder (grain size ca. 30 nm) is blown onto the membrane. This results in a uniformly distributed catalyst which is fixed to the membrane in a rolling process by passing it through a calender [180]. The Pt loading corresponds to 0.77 mg cm^{-2}. As membranes Nafion$^{®}$ 115 and different F-free membranes were employed.

Fig. 20 shows several investigated membranes coated with Pt on both sides. The squares with Pt were cut out and introduced into the fuel cell.
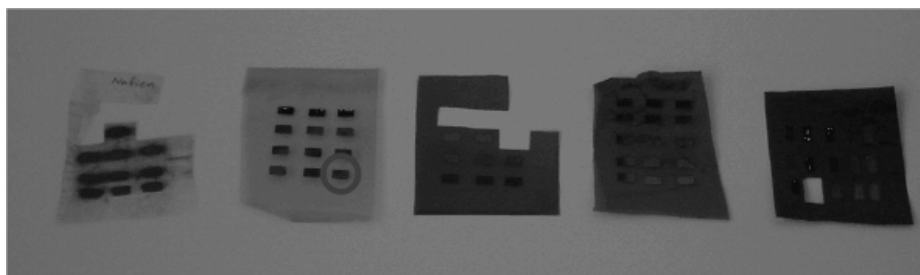
Fig. 20: Different membranes coated with Pt.

There are gas feeding channels inside the half-cylinder in order to provide the cell with oxygen and hydrogen.

The periphery for the fuel cell consists of gas sources (H_2 and O_2), gas flow control system (MKS 247 C) and humidifiers in order to moisten gases before entering the cell. Gas velocities were $10\,cm^3\,min^{-1}$, and $20\,cm^3\,min^{-1}$ for oxygen and hydrogen, respectively. To control current and voltage the electrodes were connected with a potentiostat (LB 95AR) by silver wires located in the gas channels. Fig. 21 shows a photo of the *in situ* fuel cell and the resonator of an X-band EPR spectrometer.
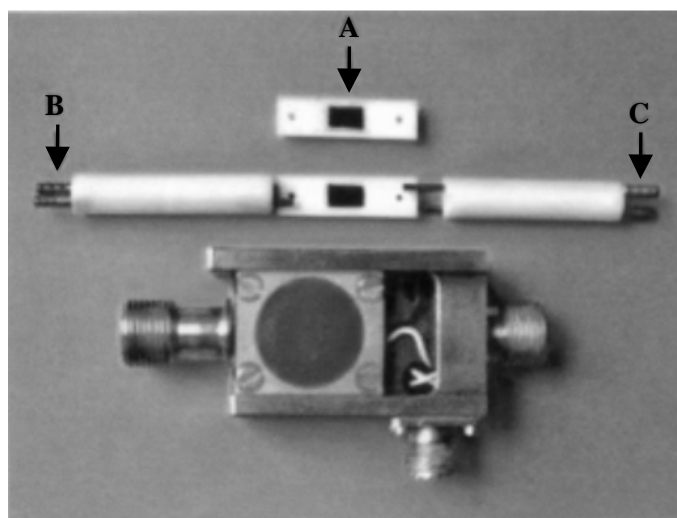
Fig. 21: *In situ* fuel cell and resonator of X-band EPR spectrometer. A - active area (fuel cell part); B - gas feeding (O_2 and H_2 channels); C - gas exhaust.

Fig. 22 depicts the *in situ* fuel cell connected to the gas suppliers and the magnet of the X-band EPR spectrometer. One can also see that the gas feeding lines are thermostatically isolated in order to control the temperature of the feeding gases.
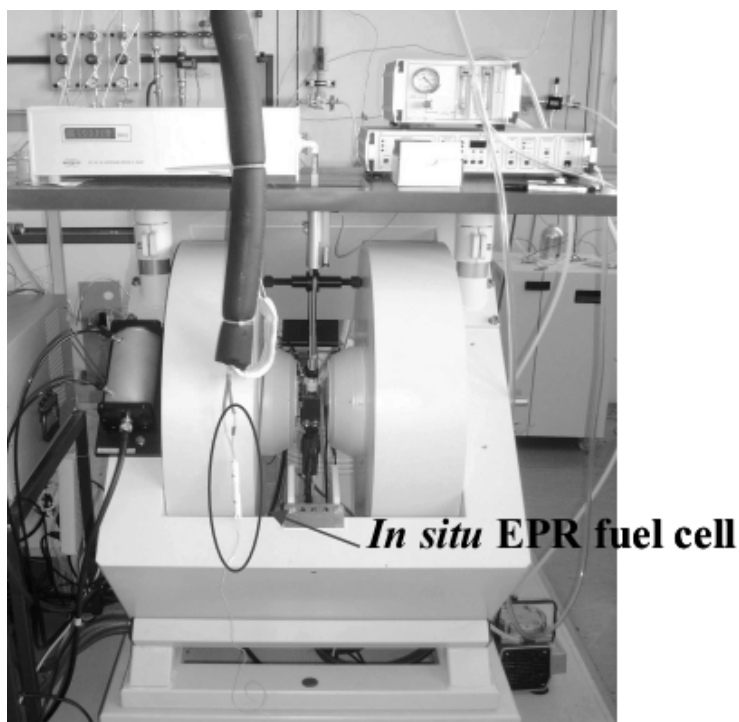
Fig. 22: *In situ* fuel cell and the magnet of the X-band EPR spectrometer.

4.2.1 Electrochemical characterization of the fuel cell

The *in situ* fuel cell was characterized electrochemically by recording polarization curves for CCMs based on 1272, 1273, 1274 [171], and Nafion® 115 membranes. The voltage was controlled by the Wenking LB 95L potentiostat (Intelligent Controls GmbH). Each point was recorded after 2 minutes of fuel cell conditioning under a given potential. Fig. 23 depicts corresponding polarization curves. All membranes show a similar behavior, but the performance of the 1272 membrane is poorer, especially at high current densities. For all membranes the *in situ* fuel cell delivers current densities approximately 50 times lower than currently used fuel cells with optimized parameters [181]. Our fuel cell is not optimized for operation under high current densities mainly because of the poor contact between membrane and catalyst particles. However, the processes in the working *in situ* fuel cell are valid for all low temperature fuel cells. Thus, it can be used for studies of different processes involving free radicals and the information derived is applicable for other fuel cells.
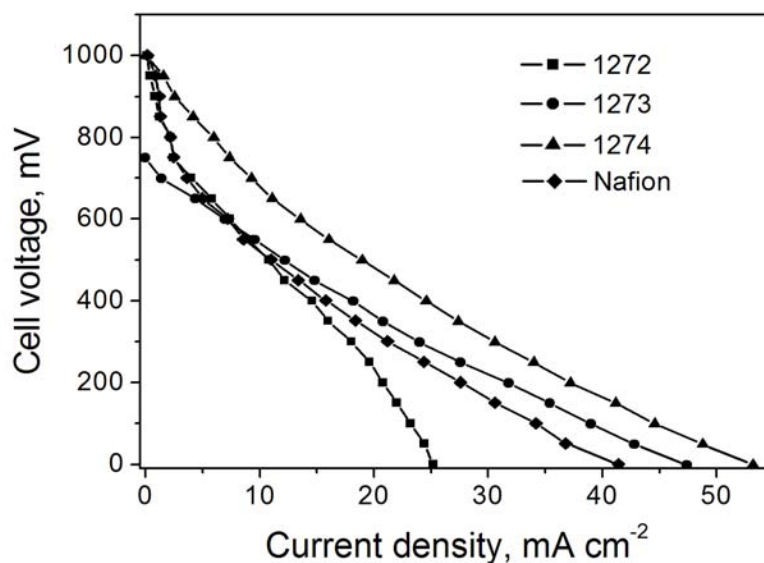
Fig. 23: Polarization curves of the *in situ* fuel cell for F-free and Nafion® 115 membranes.

Another characteristic parameter which is often used for comparing fuel cell performance is the power density which can be acquired from the cell. Fig. 24 presents power densities for the *in situ* fuel cell equipped with different membranes. The curves show characteristic behavior with a maximum after which the further increase of current density does not compensate the reduction of voltage.
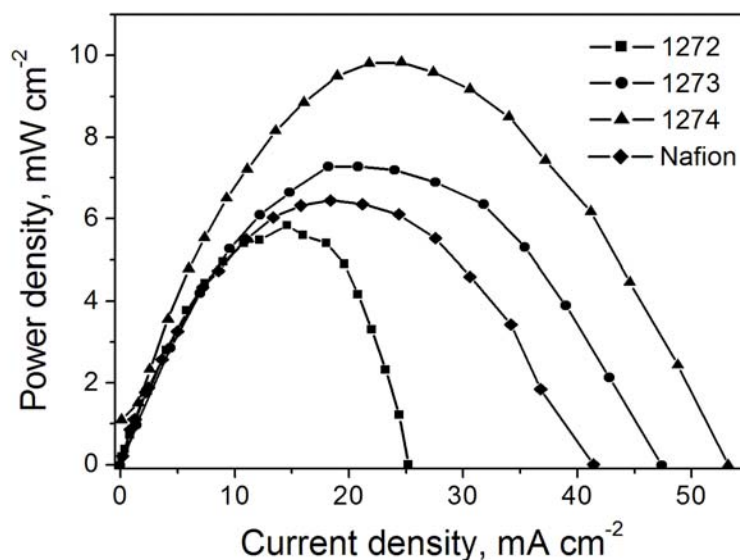
Fig. 24: Power density of the *in situ* fuel cell equipped with F-free and Nafion® 115 membranes.

Due to the fact that our fuel cell components are not optimized, it is not possible to get more than 10 mW cm^{-2}. However, modern fuel cells are able to produce very high current densities that makes them very attractive as power sources in portable and mobile applications [1, 2]. Thus the Ballard MK5-E Proton Exchange Membrane Fuel Cell Stack is capable of continuous production of 4 kW of electrical power. The power density amounts to 0.48 W cm^{-2} in this case [182].

4.2.2   Water management

EPR spectra from the *in situ* fuel cell at different running conditions are shown in Fig. 25. In this case GDEs have 0.60 mg cm^{-2} Pt. The behavior of the signal depends strongly on the fuel cell conditions. The cell was fed with both hydrogen and oxygen, only with hydrogen, only with oxygen, or with no gases. These changes in feeding conditions demonstrate great influence on the signal. The signal intensity goes down unexpectedly during fuel cell operation under both open circuit and closed circuit conditions.

This surprising result can be explained at least partly in terms of water formation in the fuel cell during its operation. Water vapor also enters the fuel cell with feed gases which are moistened in humidifiers. As it was shown in section 4.1.1 water significantly influences the signal from the electrode material.
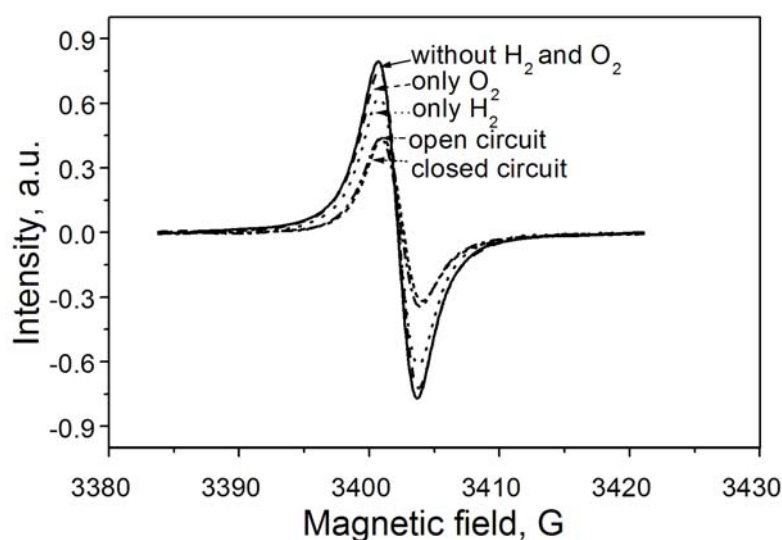
Fig. 25: EPR signal from the *in situ* fuel cell at different running conditions. GDEs contain 0.6 mg Pt cm^{-2}.

In order to investigate the influence of water on the signal experiments with dry and humid feed gases were carried out. The fuel cell was fed with humid hydrogen and oxygen until a stationary state of the signal was achieved. As a rule the necessary time for this was approximately one hour or a bit more. Later-on the gases were switched off and the signal behavior was observed further for two hours. Then the experiment was repeated once again but this time with another set of parameters. Fig. 26 shows the signal intensity behavior for deferent cases of feeding.
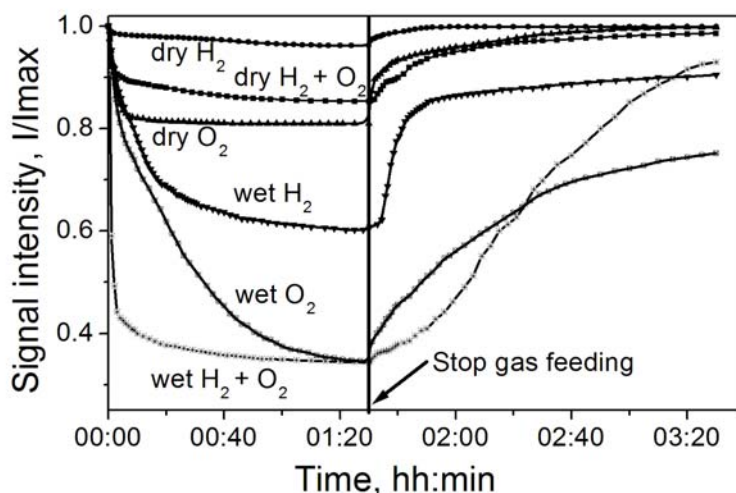
Fig. 26: Signal behavior of the *in situ* fuel cell equipped with GDEs during and after operation at different feeding conditions.

Under humid conditions the signal looses up to 65% of its intensity, whereas under dry conditions it looses only 15%. It should be noted that the position and the shape of the signal do not change.

On starting the gas feeding the intensity goes down rapidly, and approximately in 60 minutes it reaches a steady state level. When the gases are switched off the signal recovers over approximately two hours. The intensity behavior presented in Fig. 26 is quite common for the different types of membranes and may be attributed to the electrode properties (see section 4.1.1, Fig. 8).

4.2.3 *In situ* spin trap studies

The long term stability of the membrane is an important issue limiting the fuel cell lifetime [29, 31]. During extended use the membrane degrades, probably via reactions with

hydroxyl and superoxide radicals originating during oxygen reduction at the cathode [34]. Here we present a novel method for monitoring radical formation and membrane degradation *in situ* in a working fuel cell which is placed in the microwave resonator of an EPR spectrometer. By introduction of a spin trap molecule at the cathode the formation of immobilized organic radicals on the membrane surface is observed, revealing the onset of oxidative degradation which is more pronounced for F-free membranes than for Nafion®. At the anode, free radical intermediates of the fuel oxidation process are observed. No traces of membrane degradation are detected at this side of the fuel cell.

Hydroxyl and superoxide radicals are regular intermediates of the cathode reaction. This is unproblematic as long as they remain attached to the catalyst surface, but becomes dangerous for the membrane when they desorb into the water solution. Hydrogen peroxide is formed at low index Pt surfaces at the cathode. It is set free in trace amounts and found in product water [70]. In the presence of noble metals and at elevated temperatures H_2O_2 decays into hydroxyl radicals which attack the membrane. It is known that because of partial oxygen crossover through the membrane degradation can take place also at the anode. A PEM based on an inert aliphatic perfluorocarbon sulfonic acid known as Nafion® has an inherent advantage over alternative membranes based on aromatic hydrocarbons. The perfluorinated membrane should show no significant degradation on the experimental time scale [183], but serious disadvantages include its high price and high methanol permeability in cells using methanol as a fuel, leading to severe reduction of the performance [178].

Conventional *in situ* analysis of fuel cells is limited mostly to static and dynamic electrochemical methods, in particular current-voltage characteristics and impedance spectroscopy or cyclovoltammetry. They cannot easily differentiate between cathode and anode. Aiming at complementary and more selective information we developed a cell capable of operating in the resonator of an X-band EPR spectrometer [179]. It is shown that it permits the direct observation and monitoring of radical formation. The work aims at an understanding of the pathways of oxidative degradation of membranes, and it wants to provide guidance in the choice of favorable fuel cell operating conditions and in the preparation of alternative membranes with improved durability.

The concentration of free radicals produced in a fuel cell is extremely low and their lifetime is relatively short, so that it is not possible with conventional methods to observe them directly. We therefore employed the spin trapping technique, using the spin trap molecules POBN, DMPO, DBNBS, and DEPMPO. It allows the trapping of short-lived radicals under formation of relatively stable nitroxide radicals (the spin adducts) which are

detectable by EPR [184]. The spin trap solution is applied separately at the anode or the cathode side, permitting selective investigation of radical formation and of degradation reactions.

4.2.3.1 Anode side

First we study possible radical formation at the anode side of the fuel cell. The investigation is made with DMPO, POBN, and DEPMPO spin traps.

DMPO

10 μL of 1.0 M aqueous stock solution of DMPO is deposited at the electrode. After five minutes of fuel cell operation under closed circuit conditions the DMPO-$^•$H adduct is detected (Fig. 27).
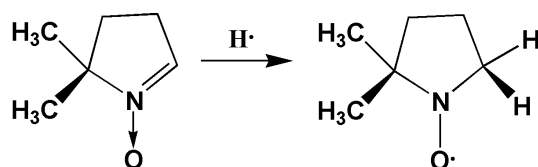
The spectrum is characterized by a *g* value of 2.0054, and it consists of a triplet of triplets due to 1:1:1 and 1:2:1 splittings by one ^{14}N ($a_N = 16.35$ G) and by two equivalent ^1H ($a_H = 22.18$ G) nuclei, respectively. The peak-to-peak line width ΔH_{pp} amounts to 1.21 G.

Fig. 27: EPR spectrum obtained with an aqueous DMPO solution at the anode side of the *in situ* fuel cell equipped with the CCM based on the 1025 membrane. H_2O was used as a solvent for the spin trap.

The result does not depend on the membrane nature. Experiments with fuel cells equipped with CCMs based on Nafion® 115 or F-free membranes with different compositions result in the same spectrum shown in Fig. 27. The mechanism of a hydrogen atom addition to a spin trap molecule is discussed in the following section.

POBN

With the spin trap POBN at the anode side, the spectrum shown in Fig. 28 was recorded after 5 minutes of closed circuit operation.

Fig. 28: EPR spectrum obtained with an aqueous POBN solution at the anode side of the *in situ* fuel cell equipped with the CCM based on the 1025 membrane. H_2O was used as a solvent for the spin trap.

The spectrum is characterized by a *g* value of 2.0056 that is typical for POBN radical adducts, and it also consists of a triplet of triplets due to 1:1:1 and 1:2:1 splittings by one ^{14}N ($a_N = 15.10$ G) and by two equivalent ^{1}H ($a_H = 9.82$ G) nuclei, respectively. The peak-to-peak line width ΔH_{pp} amounts to 0.83 G. The result does not depend on the nature of the membrane either.

The mechanism of formal H atom addition to the spin trap molecule is studied further in the following set of experiments: the fuel cell is fed with H_2 or D_2, and the POBN solution is applied. Both results in the spectrum shown in Fig. 28. No influence of D_2 was observed. Then, the two experiments are repeated, but now using a heavy water solution of the spin trap. As a result the formal D adduct to POBN was observed, as revealed by the additional splitting (Fig. 29).

Fig. 29: EPR spectrum obtained with an aqueous POBN solution at the anode side of the *in situ* fuel cell equipped with the CCM based on the 1025 membrane. D_2O was used as a solvent for the spin trap. The spectrum represents a superposition of the D adduct and, from residual protons, the H adduct.

This is clear-cut evidence of a mechanism involving reduction of POBN at the electrode surface followed by protonation by solvent molecules, H_2O or D_2O:
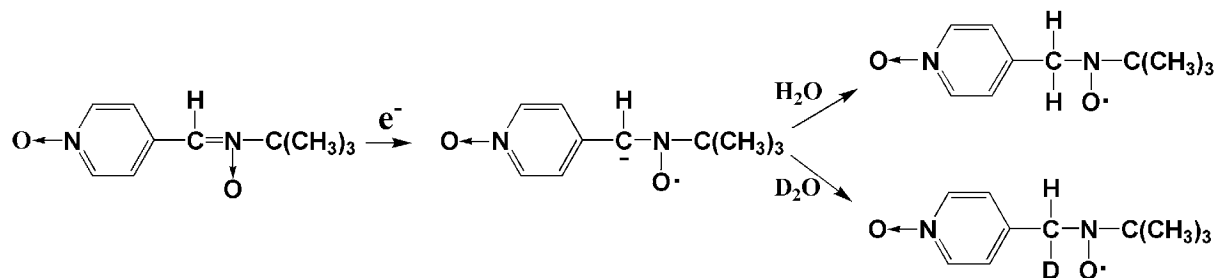
Alternatively, a fast isotope exchange could take place on the catalyst surface before the atom is trapped by POBN.

It is well known that methanol can be utilized as a fuel instead of hydrogen for low temperature fuel cells. In order to study the alcohol oxidation at the anode side of the fuel cell, ethanol-water solution was applied at the anode side of our *in situ* fuel cell. Ethanol was used because it is known to form stable and well detectable radical adducts with the POBN spin trap [176, 177]. Before the *in situ* studies we performed *ex situ* radical oxidation of the ethanol in a water solution in the presence of H_2O_2 under UV light irradiation. Absorption of UV light by the H_2O_2 molecule leads to dissociation of the molecule [24]. Fig. 30 shows a spectrum obtained after two minutes of UV irradiation of the $C_2H_5OH/H_2O/H_2O_2/POBN$ system.
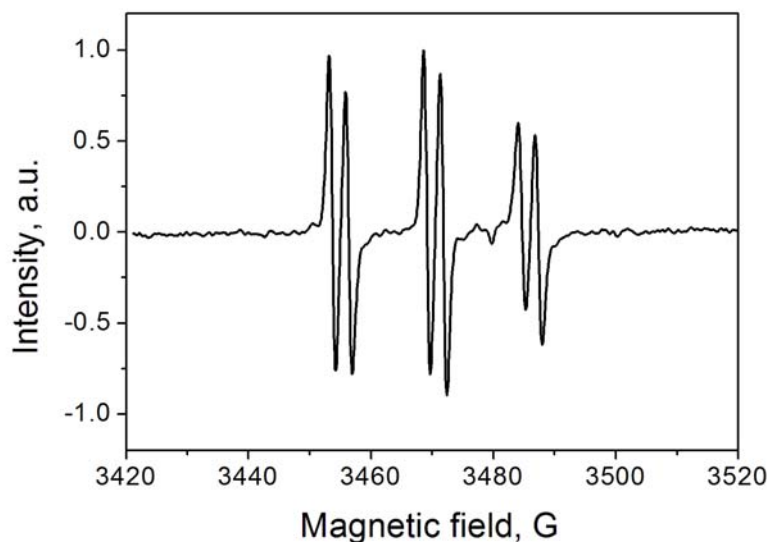
Fig. 30: EPR spectrum from the $^\bullet C_2H_4OH$ adduct to POBN in a water solution.

H_2O_2, decays into two $^\bullet OH$ radicals. These react by hydrogen abstraction with CH_3CH_2OH molecules to form $CH_3{}^\bullet CHOH$ and $^\bullet CH_2CH_2OH$ radicals (thereafter denoted $^\bullet R$). These short-lived radicals are scavenged by POBN, resulting in a stable POBN-$^\bullet R$ adduct radical. Its spectrum consists of the characteristic triplet of doublets shown in Fig. 30 and has the following parameters: $g = 2.0057$, $a_N = 15.45$ G, $a_H = 2.70$ G, $\Delta H_{pp} = 1.00$ G. While the H adduct (Fig. 28) is well distinguished from that of a trapped organic radical the splittings due to nuclei further remote than the one which makes the bond to the spin trap are normally too small to be resolved so that a distinction between different organic radicals is not normally possible.

Depositing an ethanol-water solution of POBN on the anode side of the fuel cell equipped with the Nafion$^\circledR$ 115 based CCM, and operating the cell for five minutes under closed circuit conditions results in the spectrum shown in Fig. 31.

It is a superposition of the H adduct spectrum shown in Fig. 28 and, interestingly, the R-adduct from Fig. 30. In the absence of $^\bullet OH$ the latter must arise from partial oxidation of ethanol which can also serve as a fuel in a PEMFC. This very important observation can be used for studies of oxidation mechanisms of different fuels which can be interesting for the fuel cell applications. Employment of other spin traps, e.g. nitroso compounds, may also clarify the structure of a primary radical center.

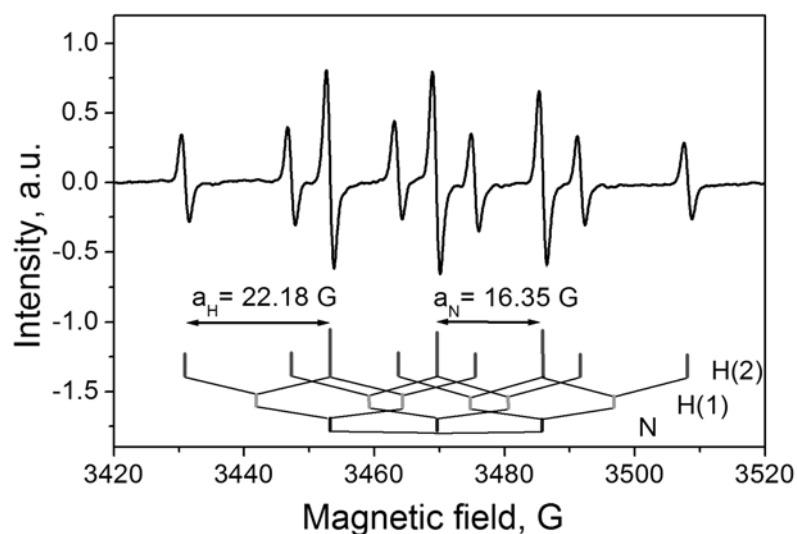**Fig. 31:** EPR spectrum obtained with POBN ethanol-water solution at the anode side of the *in situ* fuel cell equipped with the CCM based on the Nafion® 115 membrane.

DEPMPO

With the DEPMPO spin trap at the anode side the spectrum shown in Fig. 32 was recorded after 5 minutes of closed circuit operation.
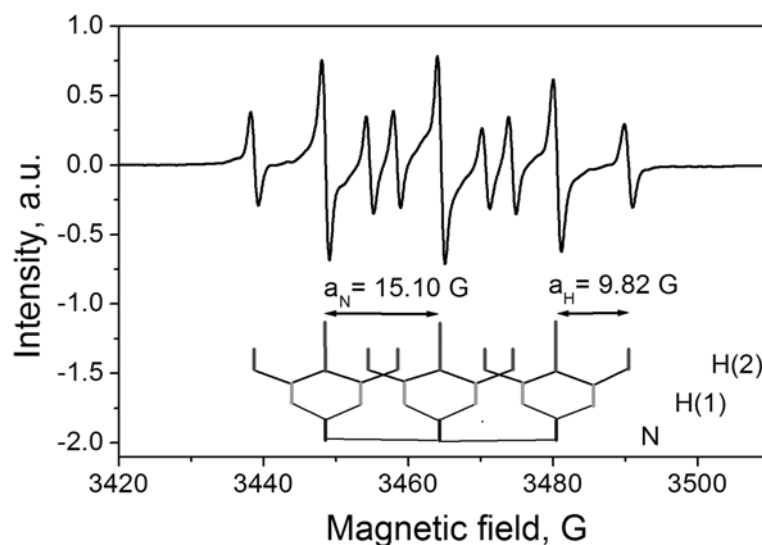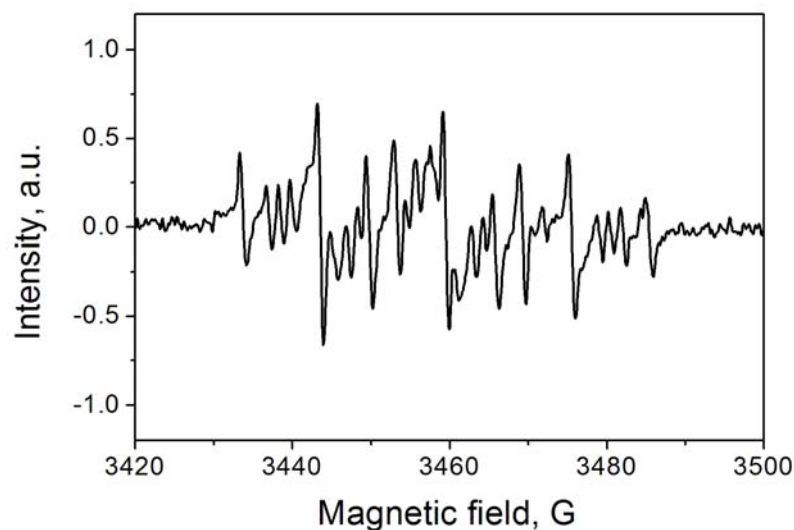

Fig. 32: EPR spectrum obtained with an aqueous DEPMPO solution at the anode side of the *in situ* fuel cell equipped with the CCM based on the 1025 membrane; a) experimental spectrum; b) simulation.

The spectrum belongs to the DEPMPO-$^\bullet$H adduct which is produced by the reduction of the DEPMPO molecule to anion-radical and consecutive addition of H$^+$ from the aqueous environment (formal addition of hydrogen atom).
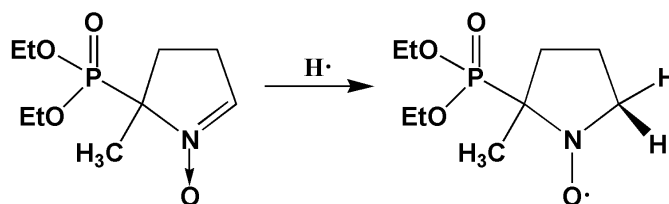
The spectrum is characterized by a *g* value of 2.0062. Compared to the DMPO spin trap, DEPMPO has additional splitting of 50.41 G due to ^{31}P. The splittings by ^{14}N and ^{1}H are 15.10 G and 20.41 G, respectively. The peak-to-peak line width ΔH_{pp} amounts to 1.49 G. The result does not depend on the nature of the membrane.

Some authors proposed possible membrane degradation at the anode side of the fuel cell [17, 29, 30], however, using the spin trapping technique neither organic radicals originating from membrane degradation nor inorganic radicals ($^\bullet$OH, $^\bullet$OOH) which could cause the degradation were detected at the anode side for any membrane being under investigation.

4.2.3.2 Cathode side

In this section we investigate the formation of organic and inorganic radicals at the cathode side of the fuel cell. The main objectives are the demonstration of membrane degradation via organic radicals on the membrane surface and the observation of radical intermediates of the oxygen reduction process during fuel cell operation. The spin traps DMPO, POBN, DBNBS, and DEPMPO are employed.

POBN

In order to study membrane degradation 10 µL of 1 M aqueous solution of POBN was deposited on the cathode equipped with Nafion$^\circledR$ 115 or F-free membranes based CCMs. The current circuit was closed for five minutes before the EPR spectra were recorded under open circuit conditions. The experiment using a Nafion$^\circledR$ 115 membrane has a very weak signal (Fig. 33).

The signal in Fig. 33 may originate from almost negligible degradation of the Nafion$^\circledR$ 115 membrane and/or from traces of POBN partial oxidation products. Numerous attempts to

accumulate the spectra in order to improve the signal to noise ratio did not lead to any remarkable improvements.
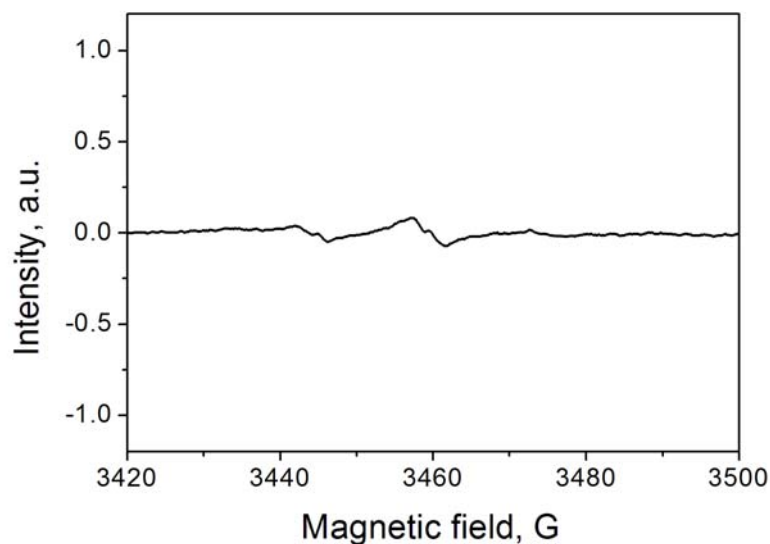
Fig. 33: EPR spectrum obtained with POBN water solution at the cathode side of the *in situ* fuel cell equipped with the CCM based on the Nafion[®] 115 membrane.

F-free membranes (1025, 504H, 1028), in contrast, exhibit a strong six-line spectrum corresponding to nitroxide radicals immobilized at the membrane surface with $g = 2.0055$ (Fig. 34).
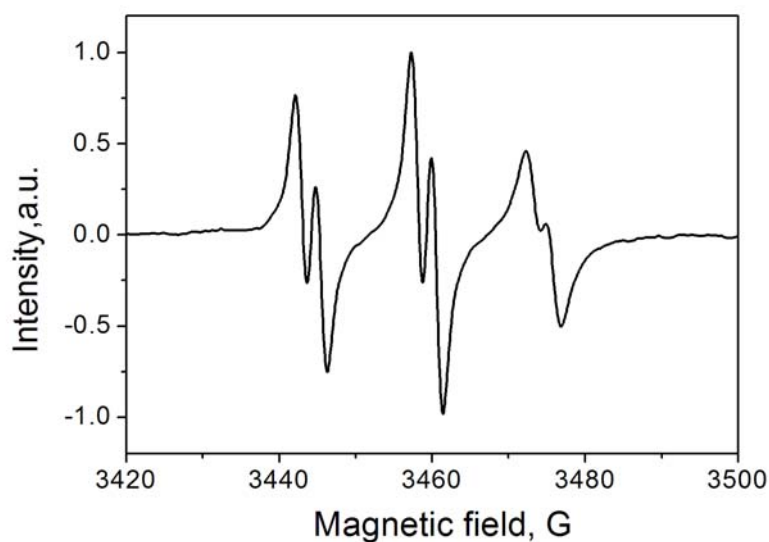
Fig. 34: EPR spectrum obtained with POBN water solution at the cathode side of the *in situ* fuel cell equipped with the CCM based on the 1025 membrane.

The splitting due to the ^{14}N nucleus ($a_N = 15.10$ G) is accompanied by the additional splitting by ^{1}H ($a_H = 2.68$ G). The line width behavior is totally different to what we observed at the anode side. $\Delta H_{pp} = 1.51$ G is found for the first four lines and 1.91 G for the doublet at high field.

During oxygen reduction at the cathode $^{\bullet}$OH radicals as intermediates of the process are formed on the Pt surface [67]. In the presence of water a small fraction of the radicals may leave the electrocatalyst and attack the membrane [36]. The dominating reaction is addition to the aromatic rings (Fig. 2). After several consecutive reactions this can lead to the loss of -SO$_3$H groups (Fig. 1) [34, 185]. Such losses are critical for the membrane performance since they lead to the reduction of proton conductivity [31].

$^{\bullet}$OH radical attack leads to organic radicals which are immobilized on the membrane surface. POBN reacts with these radicals to form stable adducts which are detectable by means of EPR and which we observe in Fig. 34:
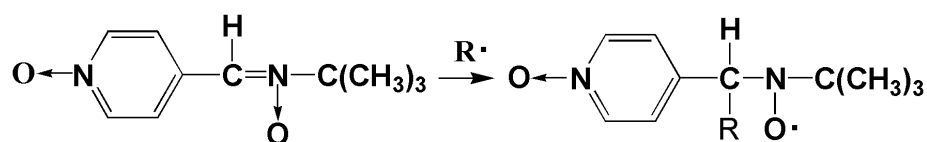
Such a spectrum is typical for POBN radical adducts with immobilized carbon centered radicals as known from previous spin trap studies [110, 186].

The key point is that immobilized radicals at the membrane surface cannot reorient isotropically, and hyperfine anisotropy is not fully averaged out. They thus reveal a spectrum with much broader lines than in water solution where they can tumble freely and average isotropically (compare Fig. 34 with Fig. 30). This additional line width is not attributed to spin exchange with oxygen, as shown in experiments with ethanol-water solution at the cathode side of the fuel cell where the spectrum has much narrower lines under similar conditions (Fig. 35). The lines in Fig. 34 are not fully resolved, especially for the doublet at high field. The broad lines provide the first direct evidence that a membrane is degraded via radical reactions in a working fuel cell [187].

For comparison an experiment with a POBN spin trap was performed with a CCM based on the Nafion$^{\circledR}$ 115 membrane in the presence of ethanol. $^{\bullet}$OH radicals formed during oxygen reduction abstract $^{\bullet}$H from ethanol molecules under formation of $^{\bullet}$C$_2$H$_4$OH radicals. These radicals are captured by POBN molecules to form POBN-$^{\bullet}$C$_2$H$_4$OH adducts having a spectrum shown in Fig. 35.
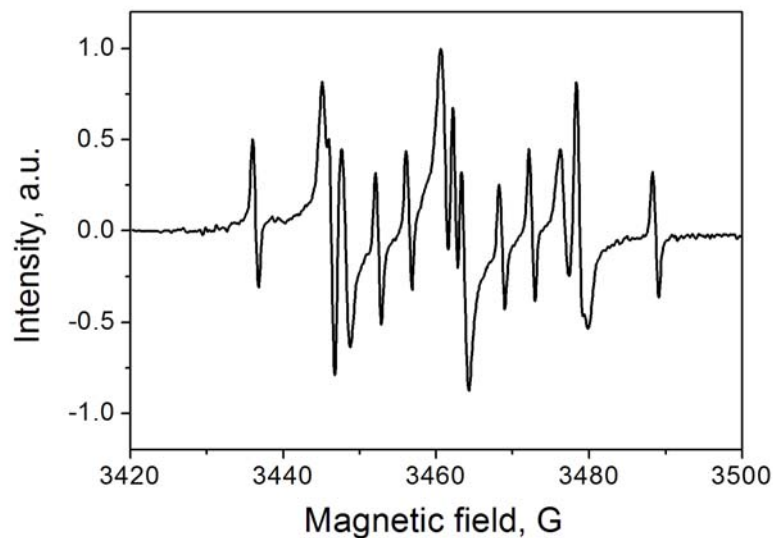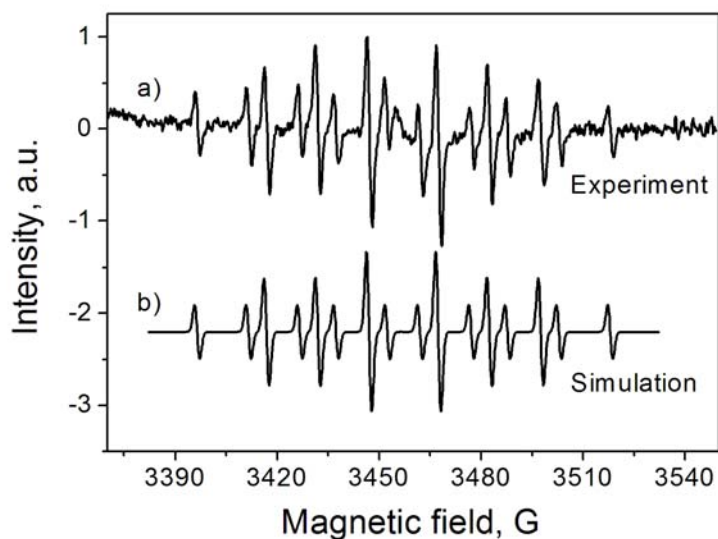
Fig. 35: EPR spectrum obtained with POBN ethanol-water solution at the cathode side of the *in situ* fuel cell equipped with the CCM based on the Nafion® 115 membrane. The spectrum belongs to the POBN-•C_2H_4OH adduct.

The spectrum consists of a triplet of doublets characteristic for the POBN-•C_2H_4OH radical adduct (Fig. 30). The lines are thinner than those from immobilized radicals (compare Fig. 34 and Fig. 35).

Introducing the radical scavenger into the membrane

It is obvious that radical attack is involved in the (thermal) decomposition of polymers, especially when the decomposition is taking place in an oxygen-containing atmosphere, the O_2 molecule being also a very aggressive radical. Because of this, a study as to whether or not integration of radical scavengers into the blend ionomer membrane can delay the thermal decomposition of the membrane was undertaken [171]. The following membranes were investigated by the authors: a ternary ionically cross-linked membrane containing sPEKH and a 1:1 molar mixture of PBI and the radical scavenger (membrane 1273), a binary ionically cross-linked membrane consisting of sPEKH and the radical scavenger (membrane 1274). As the scavenger, a commercially available compound, poly(N,N'-bis-(2,2,6,6-tetramethyl-4-piperidinyl)-1,6-diamino-hexane-co-2,4-dichloro-6-morpholino-1,3,5-triazine), which is also used as a UV stabilizer in polymers, (Aldrich No. 41,324-0, average molecular weight $M_w = 1,600$ g mol^{-1}, Fig. 36), was selected.

But the thermal stability studies revealed that the SO_3H-detachment in the blend membranes is slightly facilitated by the basic groups of the radical scavenger blend

component, probably because of the insufficient thermal stability of the radical scavenger, while the PBI blend component has no influence on the SO_3H-splitting-off temperature [171].
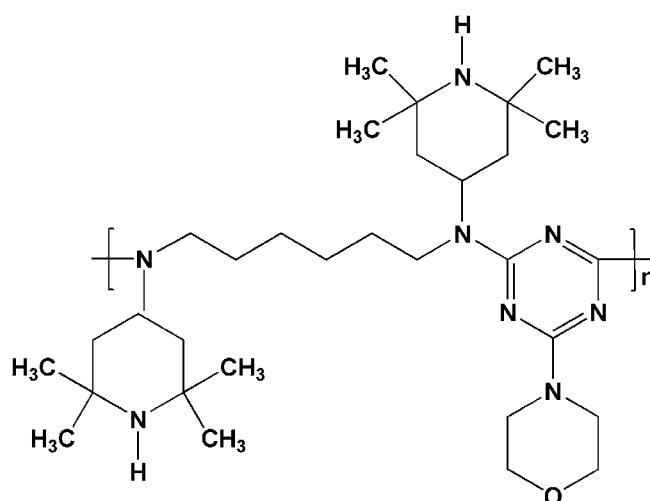
Fig. 36: Structural formula of poly(N,N'-bis-(2,2,6,6-tetramethyl-4-piperidinyl)-1,6-diamino-hexane-co-2,4-dichloro-6-morpholino-1,3,5-triazine).

On account of these data we performed studies of the membrane stability in a working fuel cell using the spin trapping technique. For this the current circuit was closed for twenty minutes before the EPR spectra were recorded under open circuit conditions. The signals from the *in situ* fuel cell equipped with CCMs based on 1273 and 1274 membranes are very weak, as can be seen in Fig. 37, which is comparable with similar tests made on CCMs based on Nafion® 115 membrane (see Fig. 33).
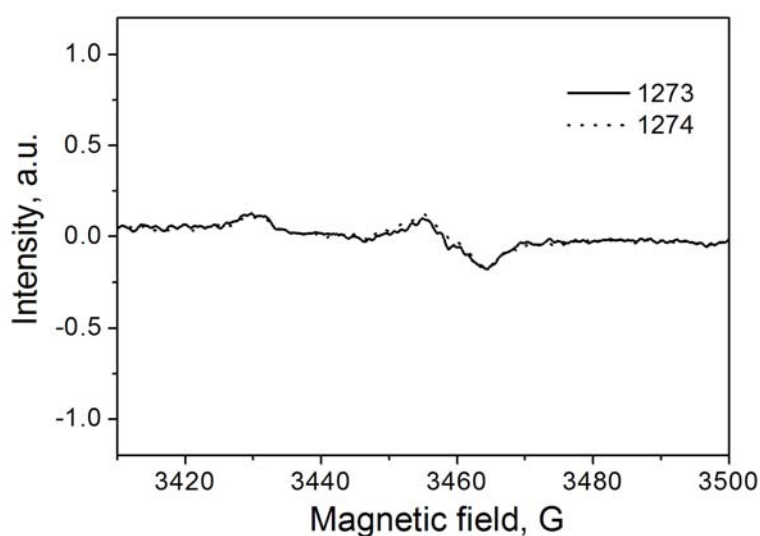
Fig. 37: EPR spectra from the *in situ* fuel cell with POBN water solution at the cathode side. CCMs based on membranes 1273 and 1274 are used.

The presence of a radical scavenger reduces the concentration of the radicals produced on the membrane surface due to the fact that radical scavengers trap them. After 20 min of closed circuit operation the concentration of the produced radicals is still very low. These studies show that introduction of a radical scavenger into a membrane leads to the reduction of membrane degradation via radical processes and improves its stability. Thus, it should be considered in designing new membrane materials for low temperature fuel cell applications with improved long term stability. However, the tested radical scavenger doesn't improve the thermal stability of a membrane [171]. For this other approaches are necessary.

DMPO

For the purpose of distinction of $^\bullet$OH radicals formed during the oxygen reduction DMPO water solution was applied at the cathode side of the fuel cell [188]. In this experiment the CCM was based on a Nafion$^\circledR$ 115 membrane. As it is already known from studies with POBN spin traps the Nafion$^\circledR$ membrane is stable against radical degradation in a working fuel cell and only gives rise to a very weak EPR signal. Fig. 38 depicts the spectrum corresponding to the DMPO-$^\bullet$OH adduct [189, 190] recorded after five minutes of closed circuit operation.

Fig. 38: EPR spectrum obtained with DMPO water solution at the cathode side of the *in situ* fuel cell equipped with the CCM based on the Nafion$^\circledR$ 115 membrane. Lines marked with squares belong to the DMPO-$^\bullet$OH adduct. a_N and in particular a_H are quite different for adducts of organic radicals [189].

The spectrum of DMPO-$^\bullet$OH radical adduct consists of triplet of doublets corresponding to the splitting of the ^{14}N nucleus ($a_N = 14.8$ G) and ^{1}H nucleus ($a_H = 14.8$ G) in the DMPO

molecule. Due to the equal splitting of the ^{14}N and ^{1}H nuclei the spectrum has only 4 lines with relative intensities 1:2:2:1. The DMPO-$^\bullet$OH can also originate from the spontaneous decay of a DMPO-superoxide adduct (DMPO-$^\bullet$OOH) [191].

The formed $^\bullet$OH (and $^\bullet$OOH) radicals attack the membrane causing its degradation via radicals. As it was in the case of POBN, by using the DMPO spin trap to study radical degradation one expects to observe anisotropic EPR spectra with relatively broad lines from the immobilized DMPO radical adducts on the membrane surface. Indeed, after 5 min of operation under closed circuit conditions with a CCM based on a F-free membrane (504H) we recorded the EPR spectrum shown in Fig. 39 which is typical for immobilized DMPO radical adducts [192].

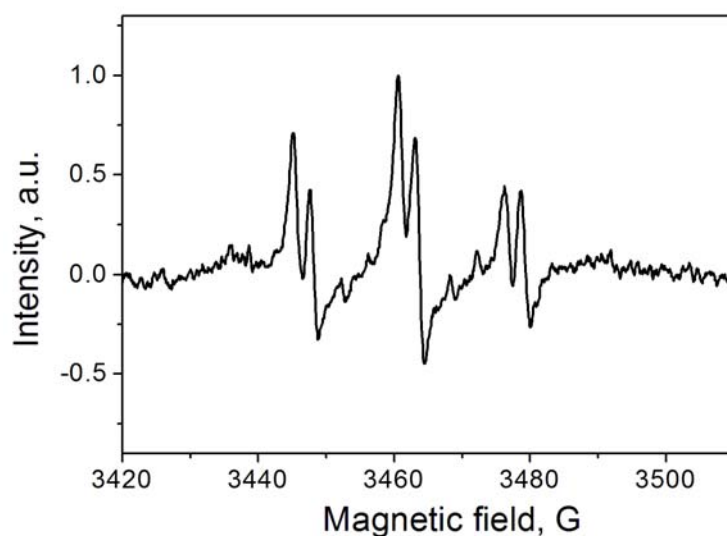**Fig. 39:** EPR spectrum obtained with DMPO water solution at the cathode side of the *in situ* fuel cell equipped with the CCM based on the 504H membrane.

The DMPO molecules react with the formed organic radicals on the membrane surface according to the following scheme:
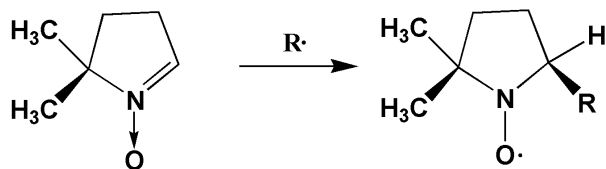
The formed DMPO-$^\bullet$R radical adducts give rise to the EPR signal (Fig. 39). The spectrum is anisotropic because the mobility of the radicals is limited. It consists of three main lines corresponding to the splitting by the ^{14}N nucleus ($a_N \approx 14.9$ G) in the DMPO molecule. A splitting due to ^{1}H is not resolved. $^\bullet$OH radical attack can produce several radical centers on the membrane surface which subsequently react with DMPO molecules. The produced DMPO-$^\bullet$R species have slightly different hyperfine constants a_N and a_H and this causes additional broadening of the lines.

It is interesting to note that after extended fuel cell operation under closed circuit conditions with CCMs based on F-free membranes (usually in the order of 1 hour for the 504H membrane and several minutes for the 1025 and 1028 membranes), subsequent introduction of the DMPO water solution at the cathode side and operation for 5 minutes under closed circuit conditions we obtain a spectrum as shown in Fig. 40.

Fig. 40: EPR spectrum obtained with DMPO water solution at the cathode side of the *in situ* fuel cell equipped with the CCM based on the 504H membrane after extended operation. Lines marked with squares belong to the DMPO-$^\bullet$OH adduct. The crosses indicate two lines which were also observed with Nafion$^\circledR$ 115 membrane.

This spectrum has two remarkable features. As it was for the Nafion$^\circledR$ 115 membrane the DMPO-$^\bullet$OH adduct is now the main product (compare with Fig. 38). But now we have

additional signal in the region 3462 - 3472 G which belongs to the DMPO immobilized radical adducts or products of DMPO adducts partial decomposition.

DBNBS

As another spin trap DBNBS was employed to membrane degradation studies in order to prove observations with POBN and DMPO. DBNBS represent a different class of nitroso spin traps. The advantage of the nitroso spin adduct is that it can yield a lot of structural information about the primary radical.

In order to study membrane degradation 10 µL of 20 mM aqueous solution of DBNBS was deposited on the cathode equipped with a F-free membrane (1025) based CCM. The current circuit was closed for five minutes as it was done for other spin traps before the EPR spectra were recorded under open circuit conditions. Fig. 41 shows a spectrum corresponding to the DBNBS-$^\bullet$R radical adduct. The spectrum is anisotropic due to the low mobility of the radicals and has very broad lines, typical for immobilized DBNBS adducts [193, 194].
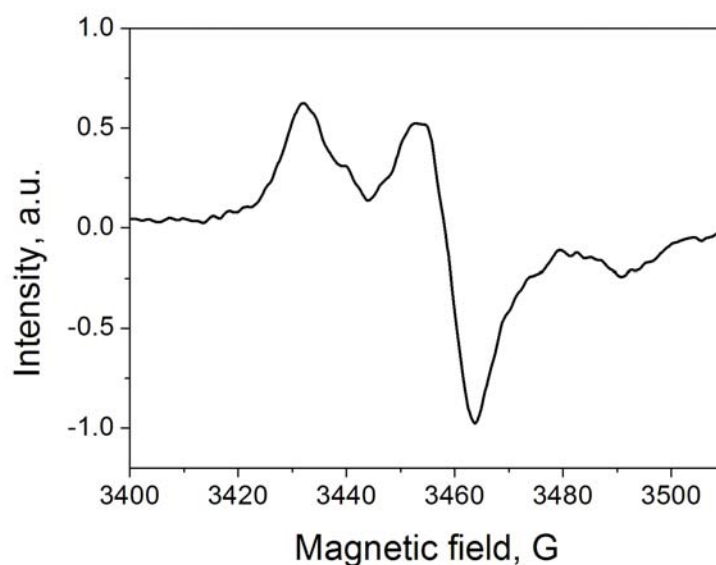
Fig. 41: EPR spectrum obtained with DBNBS water solution at the cathode side of the *in situ* fuel cell equipped with the CCM based on the 1025 membrane.

During fuel cell operation $^\bullet$OH radicals produce organic radicals on the membrane surface. DBNBS molecules react with these radicals to form stable adducts according to the following scheme:
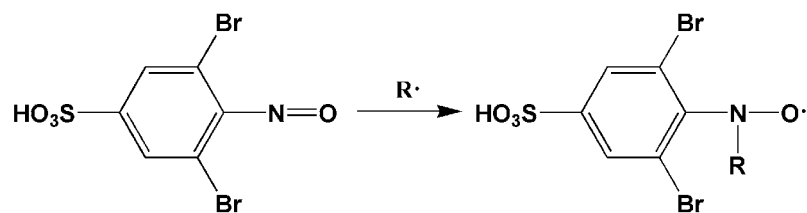
Due to the fact that DBNBS-$^{\bullet}$R radical adducts are immobilized and reveal a spectrum with very broad lines it is very difficult to get any information about the primary radical centers $^{\bullet}$R on the membrane surface and the nature of neighboring groups near the radical center. The same result was obtained with the CCM based on the 504H and 1028 membranes.

DEPMPO

A spin trap DEPMPO water solution was employed at the cathode side of the fuel cell in order to gain additional information about formed radicals and to study the possible formation of DEPMPO-$^{\bullet}$OOH radical adduct during oxygen reduction. DEPMPO molecule is known to form the DEPMPO-$^{\bullet}$OOH adduct with a characteristic spectrum well distinguishable from other radicals and stable for at least several tens of minutes [195, 196]. However, in our studies this radical species was not detected after any time of closed circuit operation. The concentration of the $^{\bullet}$OOH radicals was too low to be detected due to its low stability on Pt surfaces as it will be shown below in section 4.3.

Instead of $^{\bullet}$OOH radicals we were able to capture other radicals after 5 minutes of closed circuit operation with the CCM based on the 504H membrane. Fig. 42 shows a typical spectrum.

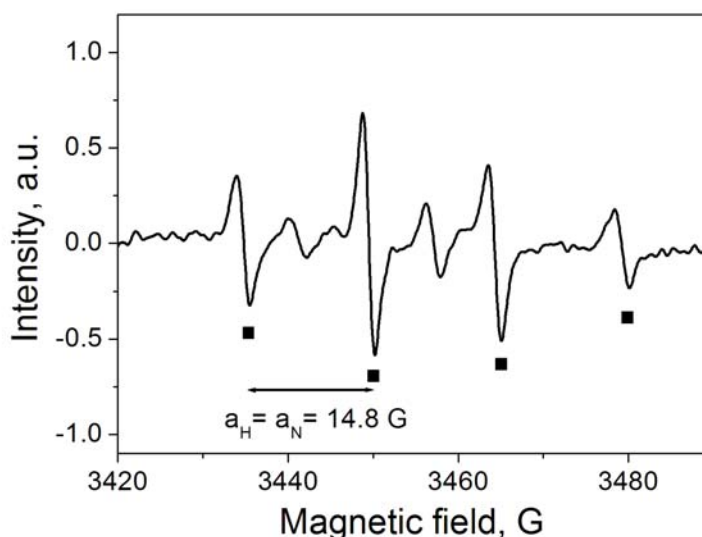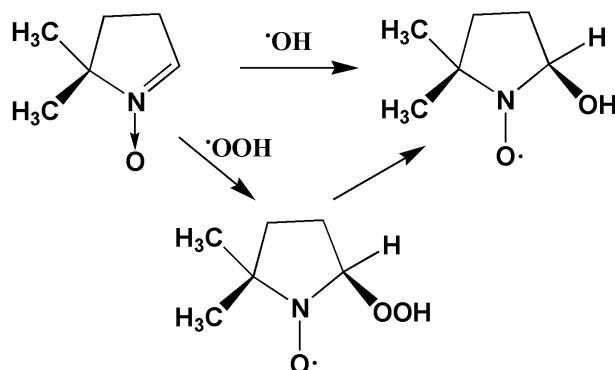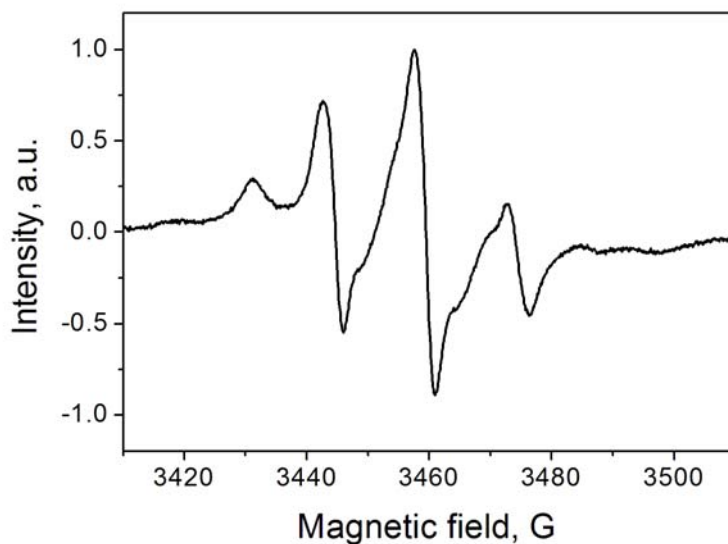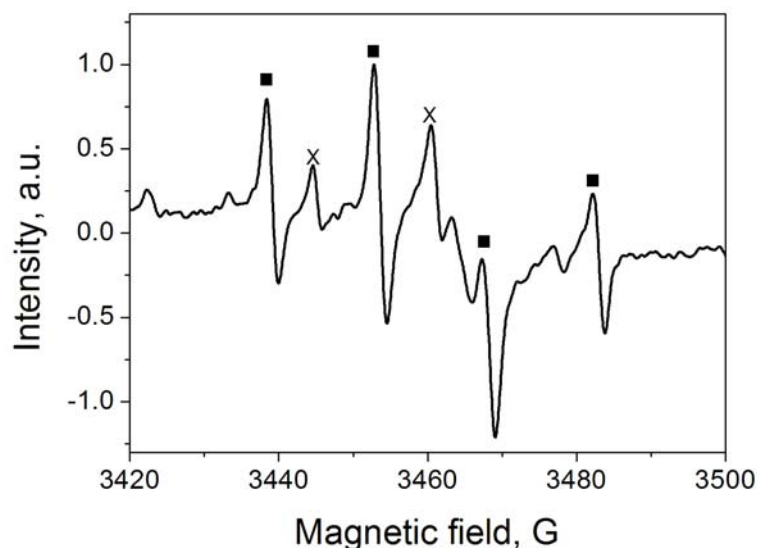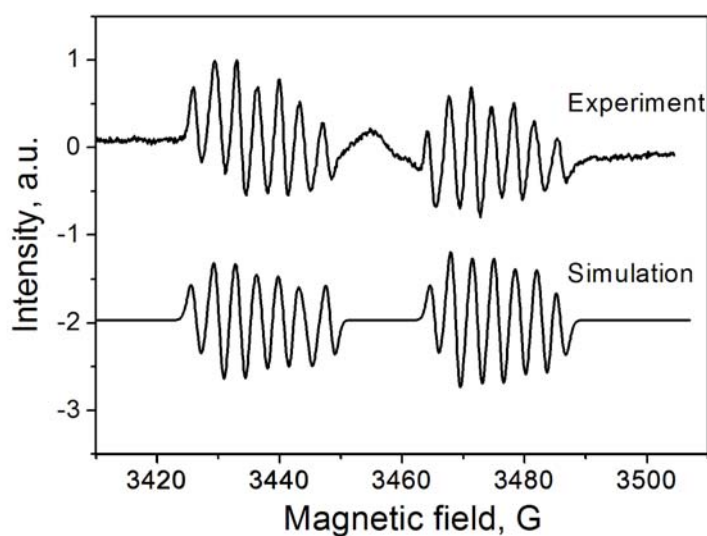**Fig. 42:** EPR spectrum obtained with DEPMPO water solution at the cathode side of the *in situ* fuel cell equipped with the CCM based on the 504H membrane.

95

The spectrum is simulated as a superposition of two radicals in equal ratio with the following parameters: peak-to-peak line width $\Delta H_{pp} = 1.4$ G, $a_N = 7.2$ G, $a_H = 3.5$ G, $a_P = 34.9$ G for the first radical and $\Delta H_{pp} = 1.4$ G, $a_N = 6.9$ G, $a_H = 3.4$ G, $a_P = 42.3$ G for the second radical, respectively. The broad central line which belongs to the immobilized species with more restricted mobility is not considered in the simulation.
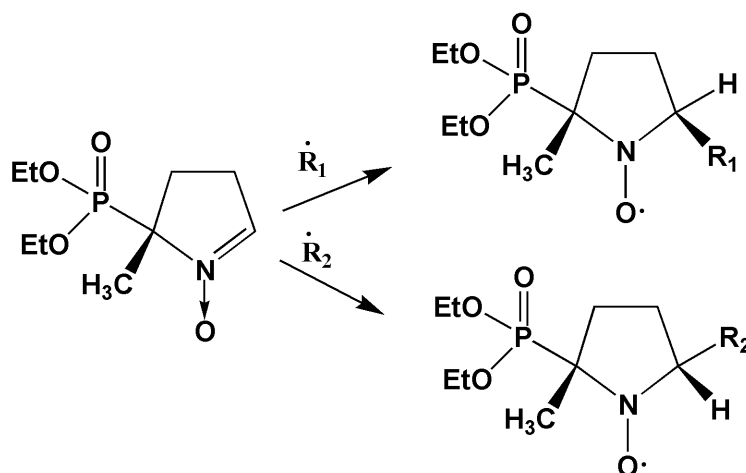
The hyperfine constant values used in this simulation are quite untypical for the DEPMPO based radicals. For example, the DEPMPO-$^\bullet$CH$_3$ radical adduct has following coupling constants: $a_N = 14.10$ G, $a_H = 20.31$ G, $a_P = 46.85$ G, and the DEPMPO-$^\bullet$OCH$_3$ radical has $a_N = 12.64$ G, $a_H = 6.61$ G, $a_P = 47.71$ G [197]. For the S-centered radical adducts DEPMPO-$^\bullet$SR$_N$ the reduction of the a_P value to 32 - 33 G is possible [198].

Couplings to β-protons and β-phosphorous (β to the N nucleus) have a geometry dependence. The determining factor is the dihedral angle, Θ, between the plane containing N-C-H (N-C-P) bonds and that containing the N-C bond and the z-axis (the axis lying along the p-orbital with the unpaired electron) [199]. The coupling constant a_H (a_P) is proportional to $\cos^2\Theta$. The maximum of a_H (a_P) should occur when $\Theta = 0°$ or $180°$; $\cos^2\Theta = 1$ (optimal hyperconjugation), whereas a_H (a_P) should vanish when the bond lies in the nodal plane of the atomic orbital ($\Theta = 90°$ or $270°$; $\cos^2\Theta = 0$; no hyperconjugation). For a freely rotating group, e.g. methyl group, the effective value $\langle\cos^2\Theta\rangle = 0.5$ corresponds to $\Theta = 45°$. Bulky substituents R in DEPMPO-$^\bullet$R adducts can have a remarkable influence on the molecular conformation leading to considerable changes of the hyperconjugation of the unpaired electron with β-H (β-P).

DEPMPO adducts in water solution are known to form diastereomers with different coupling constants by the ^{1}H, ^{14}N, and ^{31}P nuclei due to the angular dependence of the a_P and a_H. For the DEPMPO-$^\bullet$R radical adduct the formation of both *trans*- and *cis*-diastereomers is

possible. The *trans*-diastereomer results from addition of $^{\bullet}$R to the less hindered face of the molecule, and the *cis* – from the addition of $^{\bullet}$R to the face where -P(O)(OC$_2$H$_5$)$_2$ substituent is. As it is known for DEPMPO spin trap adducts with alkylperoxyl radicals, the differences between the diastereomers in the a_P coupling constant can be larger than 10 G. Differences in a_N and a_H coupling constants are smaller, but also considerable [200]. For small R both diastereomers can be formed in similar ratio, however, for balky R the formation of *cis*-diastereomer is hindered due to the steric hindrance and basically *trans*-diastereomer is formed.

For the DEPMPO-$^{\bullet}$R adducts on the membrane surface the group R is situated on the surface, thus R can be considered as a bulky substituent. It is reasonable to assume that mainly the *trans*-diastereomer will be formed. The two identified DEPMPO-$^{\bullet}$R species (DEPMPO-$^{\bullet}$R$_1$ and DEPMPO-$^{\bullet}$R$_2$) can belong to the two conformers within the five-membered ring which exhibit significantly different mean values of the coupling constants. Present structural hindrances can prevent the fast conversion from one conformer to another [201, 202]. The structural hindrances can also lead to the increase of the dihedral angle Θ described above, resulting in the decrease of the hyperconjugation of the unpaired electron with β-H and subsequently decrease of the a_H. The magnitude of the hyperfine constants is influenced by the nature of the radical center as well. With increasing electrophilicity of the R group the a_N and a_H for DEPMPO-$^{\bullet}$R radical adducts become smaller [197]. All these facts should be kept in mind when analyzing our small coupling constants for H considered in the simulation.

4.3   Oxygen reduction

In this subchapter aspects of the O_2 and its reduction intermediates adsorption on Pt(111), Pt(100), and Pt(110) surfaces, modeled by the four-layer slabs, are studied. The correct description of the system is confirmed by the comparison of the uncoordinated species with available experimental and theoretical data. The influence of the applied electric field on the properties of the adsorbed species is investigated employing a $Pt_9(111)$ cluster as a substrate. The impact of two coadsorbed water molecules on the adsorption properties of the O_2 and $^\bullet OH$ are studied. The relevance of the obtained data for the oxygen reduction reaction in low temperature fuel cells is also discussed.

4.3.1   Uncoordinated O-containing species

In order to validate the methods used for the calculations of the oxygen and oxygen containing species adsorbed on low index Pt, calculations of O_2, $^\bullet OOH$, and H_2O_2 were performed with the VASP and Gaussian 98 packages.

Table 5 summarizes bond lengths and stretching frequencies of the oxygen and products of consecutive one-electron additions to the O_2 molecule in the gas phase. The computational approaches applied in this study are known to yield reasonable results for the oxygen containing species on Pt clusters [74, 83] and extended surfaces [75, 96, 97]. In our surface calculations we neutralize the oxygen reduction intermediates with protons to $^\bullet OOH$, H_2O_2, and $^\bullet OH$, and we believe that these species play the principal role in understanding the process of oxygen reduction in a running fuel cell under acidic conditions.

Both the VASP (PW91-GGA/PAW) and Gaussian 98 (B3LYP/6-311G**) computations describe the oxygen molecule, superoxide radical and hydrogen peroxide in the gas phase reasonably well, although VASP slightly overestimates the O-O bond length for O_2, and Gaussian 98 underestimates the bond for the $^\bullet OOH$ and H_2O_2 species that causes corresponding shifts of the vibrational frequencies.

However, it is well known that DFT methods can fail in accurately describing electron affinities and ionization potentials of weakly bound anions, in particular oxides. High-level methods, e.g. MRCI or CCSD(T) using large basis sets are necessary to obtain quantitative

agreement with experiment [203]. Calculations at these levels have not been carried out for the surface-adsorbate system due to the large amount of CPU time necessary.

Table 5: Bond lengths and stretching frequencies of the O_2, $^\bullet OOH$, and H_2O_2 obtained by experiment, VASP, and Gaussian 98.

	O-O		$^\bullet$O-OH		HO-OH	
	Bond length, Å	Frequency, cm^{-1}	Bond length, Å	Frequency, cm^{-1}	Bond length, Å	Frequency, cm^{-1}
VASP (PW91-GGA/PAW)	1.24	1516	1.35	1174	1.48	994
Gaussian 98 (B3LYP/6-311G**)	1.21	1578	1.33	1163	1.45	943
Experiment [204 - 209]	1.208	1580	1.372	1098	1.490	890

4.3.2 Adsorption properties of the O-containing species in the absence of water

In this section properties of the (radical) intermediates of the oxygen reduction adsorbed on the (111), (100), and (110) surfaces are studied. Five species are considered: O_2, O, $^\bullet OH$, $^\bullet OOH$, and H_2O_2.

4.3.2.1 O_2 molecule

The adsorption of oxygen on platinum surfaces is a fundamental step in its reduction mechanism. Full optimization of adsorbed oxygen molecules was performed for several possible sites on the Pt surface, yielding the adsorption energy, the adsorption geometry, and the charge transfer. In agreement with previous studies of the system [75, 86] we found three favorable positions for molecular oxygen adsorption on Pt(111). Two of them are almost identical and correspond to the hollow position (fcc and hcp) between three Pt atoms

(Fig. 43a) with adsorption energies of -0.52 eV and -0.46 eV, respectively, whereas the third so-called bridge position between two Pt atoms (Fig. 43b) is the most stable. The O-O bond length is stretched from its gas phase value of 1.24 Å to 1.38 Å and 1.36 Å for the hollow and bridge positions, respectively. It is interesting to note that the O-O bond length for the most stable adsorption state (bridge position) is the shortest one on the (111) surface.
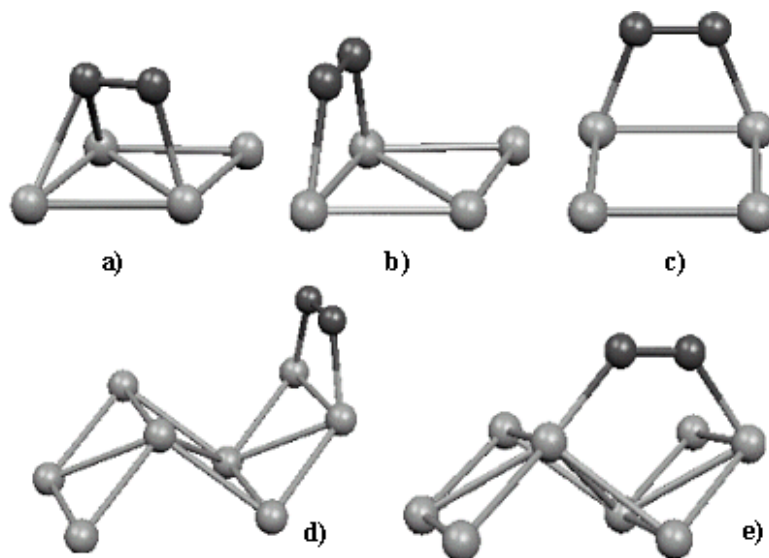
Fig. 43: Oxygen molecule adsorbed on low index Pt surfaces; a) hollow position on (111); b) bridge position on (111); c) bridge position on (100); d) short bridge position on (110); e) long bridge position on (110).

In order to evaluate the extent of consistency between the VASP calculations with periodic boundary conditions and the Gaussian 98 calculations on the isolated $Pt_9(111)$ cluster (Fig. 6) we performed a test calculation with VASP for O_2 adsorbed on the $Pt_9(111)$ cluster as the repetitive element with Pt-Pt bond length of 2.77 Å, resulting in adsorption energies of -0.17 eV and -0.32 eV for the hollow and bridge positions, respectively. The decrease of the adsorption energy is caused by the fact that Pt-Pt optimized distance is calculated to be 0.05 Å longer, and therefore the cluster is under stress. Moreover, Pt atoms in the cluster were not allowed to relax in the presence of the adsorbed oxygen molecule. The O-O bond length on the $Pt_9(111)$ cluster was calculated to be 1.31 Å and 1.30 Å for the hollow and bridge positions, respectively, compared with 1.39 Å and 1.29 Å for the results for the same systems calculated by Gaussian 98. The molecule moved away from the surface from 2.03 Å and 2×2.07 Å from the Gaussian 98 results to 2.11 Å and 2×2.45 Å Pt-O distances for the hollow position and from 2.11 Å from the Gaussian 98 results to 2.15 Å for the bridge position. The cluster studies of the adsorption characteristics deliver the right trend in energies

and geometries, but a four-layer slab model is essential for obtaining reasonable results that compare favorably to STM and EELS experiments on extended Pt(111) surfaces [87, 88].

On the (100) surface we found one site of preferential molecular adsorption. The oxygen molecule lies between two Pt atoms (Fig. 43c).

On the (110) surface we found two favorable states of oxygen adsorption, which are the different bridge positions between two neighboring Pt atoms in the first layer (Fig. 43d, Fig. 43e). At the short bridge position the O-O bond is stretched to 1.38 Å, whereas at the long bridge site the bond is computed to be slightly shorter. Some selected properties of the adsorbed O_2 are given in Table 6. Note that the short bridge position on the (110) surface is the most favorable adsorption site for the oxygen molecule among the three low index planes of platinum, suggesting that it is the preferred adsorption site on a polycrystalline Pt substrate.

Table 6: Selected properties of the O_2 molecule adsorbed on low index Pt surfaces derived from the VASP (PW91-GGA/PAW) results for the four-layer slab.

Adsorption site		Adsorption energy, eV	Pt-O bond length, Å	O-O bond length, Å
Hollow (111)	hcp	-0.46	1) 2.31 × 2	1.38
	fcc	-0.52	2) 2.05	
Bridge (111)		-0.63	2.06 × 2	1.36
Bridge (100)		-1.02	2.02 × 2	1.37
Short bridge (110)		-1.58	1.99 × 2	1.38
Long bridge (110)		-1.07	2.03 × 2	1.37

In addition to obtaining geometries and total energies, DFT results also include the electron charge density, $\rho_e(z)$, which has the sign convention of being more positive where the density of electrons is higher. Fig. 44 shows the electron charge density of the O_2-Pt system with oxygen adsorbed at the hollow position. The two oxygen atoms are both contained in the peak at 13.5 Å.
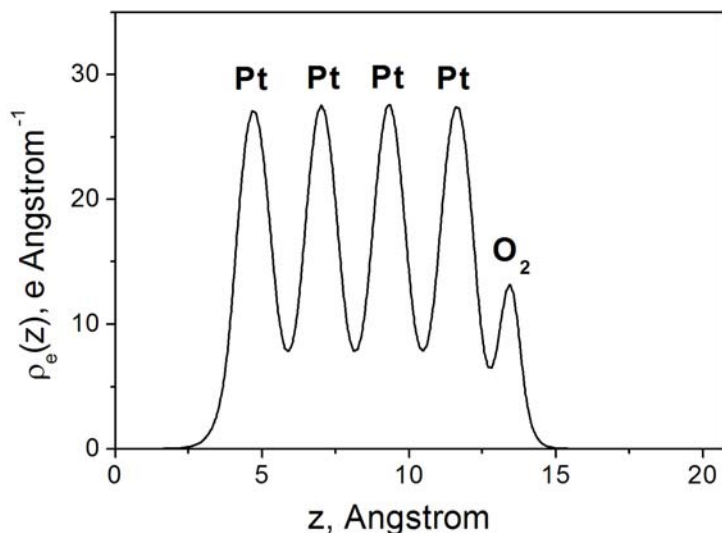
Fig. 44: Electron charge density of the O_2-Pt system with the oxygen molecule adsorbed on the Pt(111) surface at the hollow position.

For a better understanding of the charge transfer and distribution and the formation of the bond it is useful to subtract the charge densities for the slab and isolated species from the charge densities of the adsorbed systems. For example, for the oxygen molecule the charge transfer function is defined as:

$$\Delta\rho_e(z) = \left\{ \rho_e(z)/O_2Pt_{(111)} - \rho_e(z)/O_2 - \rho_e(z)/Pt_{(111)} \right\} \tag{4-2}$$

where $\rho_e(z)/O_2Pt_{(111)}$ is the electron density of the system with the adsorbed oxygen molecule, $\rho_e(z)/O_2$ is the electron density of isolated O_2 with its positions fixed to these in its adsorbed state, and $\rho_e(z)/Pt_{(111)}$ is the electron density of the Pt(111) slab.
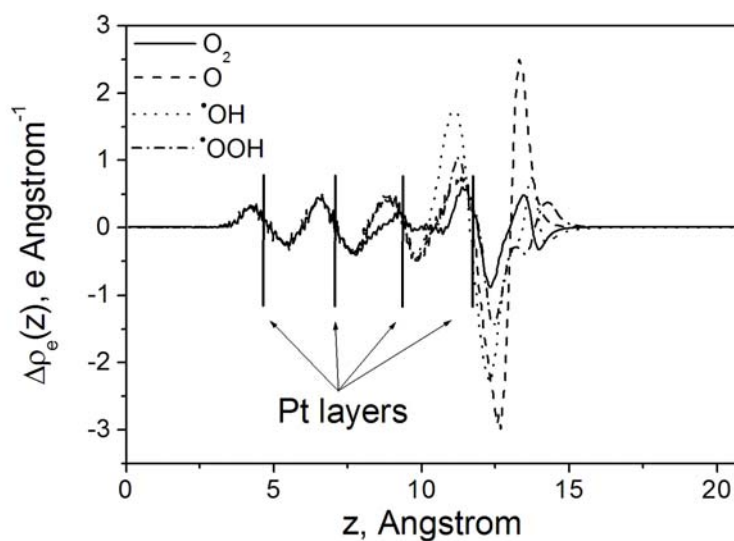
Fig. 45: Charge transfer functions for O_2, O, •OOH, and •OH adsorbed on Pt(111) surface. Adsorbed species are observed at 13.0 - 14.0 Å, the Pt slab at 4.7 - 11.9 Å.

Fig. 45 shows the charge transfer functions for several oxygen containing species on the Pt(111) surface. For all species the charge is transferred from the Pt slab to the adsorbed species and shows a polarization and an oscillatory behavior that is considerably but not completely damped out over four layers. It is expected that oscillations would damp out the further we enter the metal. The oscillation damping behaves equally for all species after the third Pt layer, but in contrast to other adsorbates, the oscillation order for the adsorbed oxygen molecule is broken in the first two layers.

In order to investigate the dependence of the system properties on the electric field, optimized geometries were taken from the VASP results and applied to those on a Pt_9(111) cluster and reoptimized again. Fig. 46 displays the O-O bond length of O_2 adsorbed on the Pt_9(111) cluster at the hollow and bridge positions as a function of applied electric field. As expected, the O-O bond length decreases with increasing field for both, the hollow and bridge positions, but the dependence is more pronounced for the bridge adsorption site, where O_2 is more strongly adsorbed.
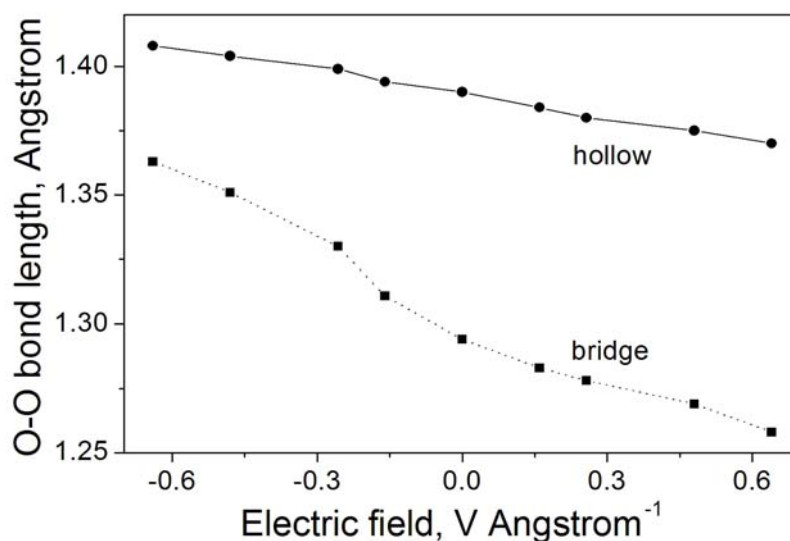
Fig. 46: Bond length in the O_2 molecule adsorbed on a Pt_9 cluster at the hollow and bridge positions as a function of the applied electric field.

The distances between oxygen atoms of the adsorbed O_2 molecule and the nearest Pt atoms of the Pt_9(111) cluster are plotted as a function of applied electric field in Fig. 47. The increasing electric field pushes the molecule away from the surface. This field dependent displacement is relatively moderate for the hollow position, but the bridge position, by contrast, reveals a much more pronounced field dependence.

Fig. 47: Pt-O distances in the system Pt$_9$-O$_2$ for the hollow and bridge adsorption sites as a function of the applied electric field. O(2) lies closer to the Pt surface between two Pt atoms, O(1) is further away and is connected to only one Pt atom.

Fig. 48 shows natural atomic charges of the oxygen atoms for the O$_2$ molecule adsorbed at the hollow and bridge positions on the Pt$_9$(111) cluster as a function of applied electric field. In general, the oxygen molecule at the hollow position bears more negative charge than at the bridge position, suggesting that oxygen in the hollow position is more polarized. This is in a good agreement with associating the O$_2$ at the hollow position to a peroxolike (O$_2^{2-}$) state and O$_2$ at the bridge position to a superoxolike (O$_2^-$) state. The charge from the *d*-orbitals of the Pt atoms is transferred mostly to the $2\pi^*$-orbital of the adsorbed O$_2$ molecule. Without an applied electric field the difference between the 2*p*-populations of the oxygen atoms in a O$_2$ molecule in the gas phase and adsorbed on the Pt surface amounts to -0.19 a.u. for the bridge position per O atom and -0.31 and -0.26 a.u. for the O atoms in O$_{2ads}$ at the hollow position. The more negative value corresponds to the O atom lying closer to the Pt surface.

The electric field dependence of the charge transfer in the case of the bridge position is more pronounced than for the hollow position, showing that the polarizability of O$_2$ at the bridge position is higher. For the peroxolike oxygen at the hollow position it is apparently more difficult to accept more electrons with decreasing electric field, which may be related to the fact that the $2\pi^*$-orbital is saturated for this species, but the superoxolike oxygen at the bridge position can still accept charge.
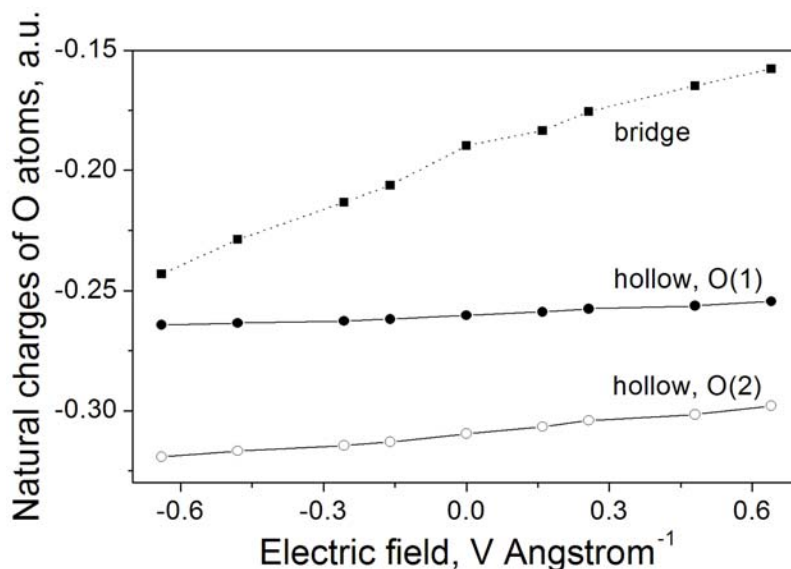
Fig. 48: Natural atomic charges of the O atoms in the O_2 molecule adsorbed on a Pt_9 cluster at the hollow and bridge positions as a function of the applied electric field.

Decreasing the electric field leads to an electron transfer to the adsorbed O_2 molecule and to an increase of the antibonding $2\pi^*$-orbital population. As a result, the O-O bond weakens, and finally the O_2 molecule would dissociate on the surface. Fig. 49 shows the O-O stretching frequency in the O_{2ads} molecule at the hollow and bridge positions on the $Pt_9(111)$ cluster.
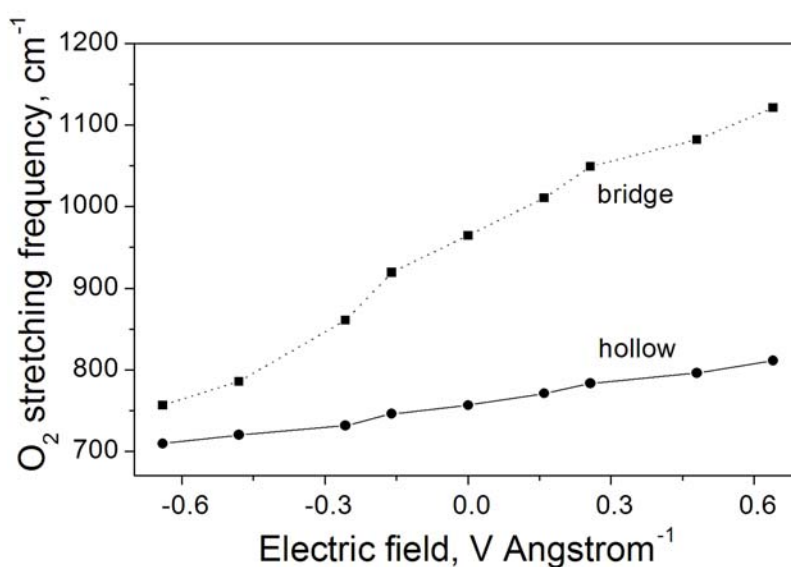
Fig. 49: O-O stretching frequency of the O_2 molecule adsorbed on a Pt_9 cluster at the hollow and bridge positions as a function of the applied electric field.

A more negative field weakens the internal O-O bond, shifting the frequency to lower values for both adsorption sites. Again the field dependence for the bridge position is

stronger, which we ascribe to the $2\pi^*$-orbital not being saturated for the superoxolike species adsorbed in the bridge position. The experimental values in the absence of an electric field are 690 and 870 cm^{-1} for the hollow and bridge positions, respectively [86], which compares reasonably well with our values on the Pt$_9$(111) cluster, ca. 740 and 960 cm^{-1}, respectively (Fig. 49). Previous VASP calculations of the adsorbed oxygen molecule gave 690 and 850 cm^{-1}, respectively [75].

4.3.2.2   O atom

The product of oxygen molecule dissociation in the gas phase under UHV conditions, atomic oxygen, is the most stable configuration of oxygen on Pt surfaces. On the (111) surface atomic oxygen prefers the threefold hollow sites (Fig. 50a).
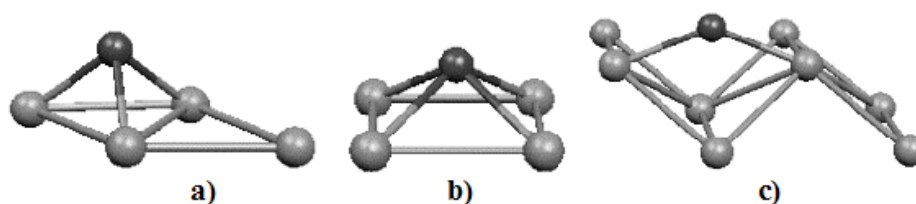
Fig. 50: Atomic oxygen adsorbed on low index Pt surfaces; a) hollow position on (111); b) hollow position on (100); c) bridge position on (110).

On the (100) surface, the atom lies in the fourfold hollow between four Pt atoms (Fig. 50b), and only on the (110) surface the bridge position between 2 Pt atoms of the first layer (Fig. 50c) is preferred. Note that, interestingly, Pt(100) is the surface with the lowest affinity for atomic oxygen, although the difference with Pt(111) is small. Binding energies and distances of the adsorbed O atom in its most stable adsorption sites on the three low index Pt surfaces are given in Table 7.

Atomic oxygen serves as an acceptor of electron density from the Pt surface. The charge transfer function shows a high polarization in the region of the Pt-O bond (Fig. 45), providing evidence for the fact that the bond has predominantly ionic character, which is consistent with previous theoretical studies of the system [210-212]. In comparison to the gas phase, the oxygen atom on the Pt$_9$(111) cluster loses 0.04 a.u. of charge of its $2s$-population, but accepts 0.58 a.u. to its $2p$-population.

Table 7: Selected properties of the atomic oxygen adsorbed on low index Pt surfaces derived from the VASP (PW91-GGA/PAW) results for the four-layer slab.

Adsorption site		Adsorption energy, eV	Pt-O bond length, Å
Hollow (111)	hcp	-3.78	2.06×3
	fcc	-4.08	2.04×3
Hollow (100)		-3.70	2.25×4
Bridge (110)		-4.47	2.16×2

The electric field dependence of the O_{ads} properties were investigated for the $Pt_9(111)$-O system, where atomic oxygen lies in the threefold hollow position. The dependence of the Pt-O distance on the applied electric field is shown in Fig. 51.
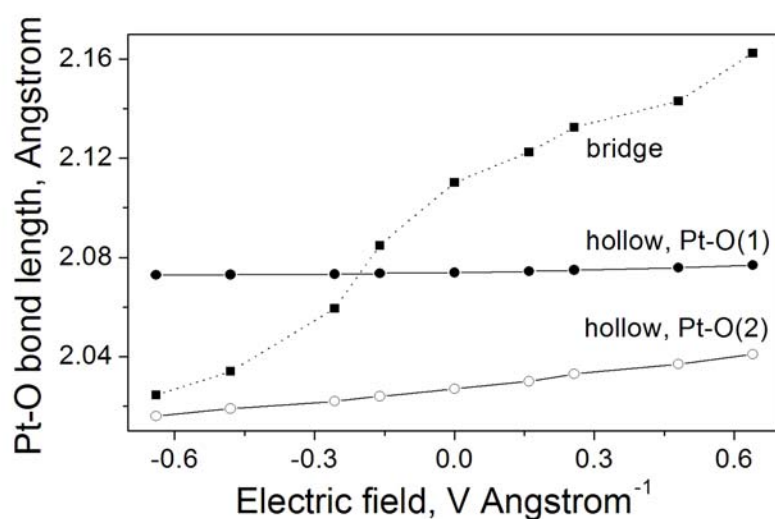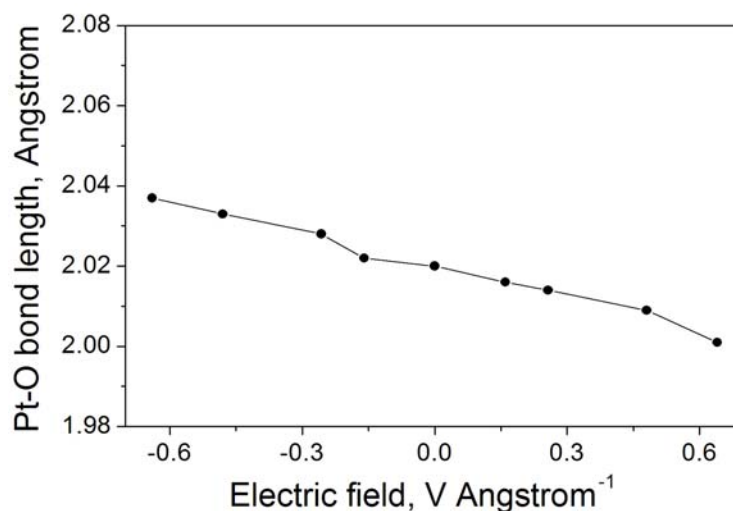

Fig. 51: Pt-O distance in the system Pt_9-O for the hollow adsorption site as a function of the applied electric field.

Negative electric fields lead to an elongation of the surface-O distance, in good agreement with previous studies [210, 213]. The decrease of the applied field from +0.64 to -0.64 V Å^{-1} has a small influence on the geometry of the O_{ads} on the Pt_9 cluster and is accompanied by a moderate increase of the natural atomic charge, which reaches a value of -0.65 a.u. for -0.64 V Å^{-1} (Fig. 52).

107
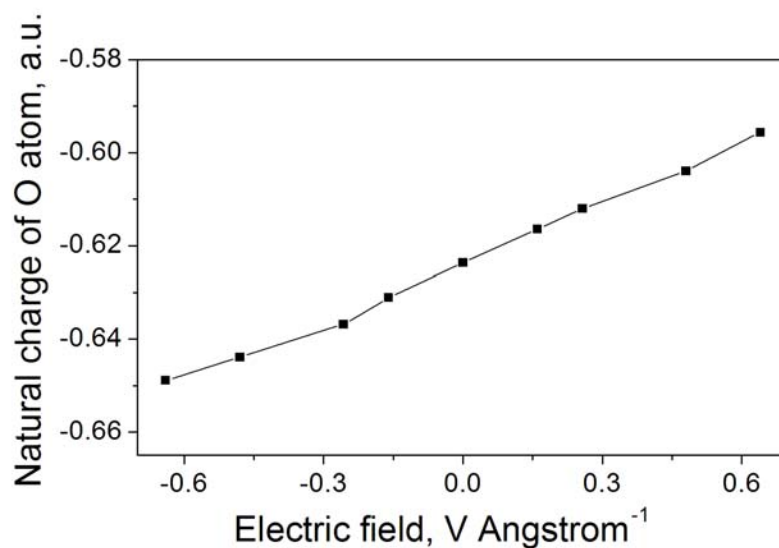
Fig. 52: Natural atomic charge of the O atom adsorbed on a Pt$_9$ cluster at the hollow position as a function of the applied electric field.

The Pt-O stretching frequency is shown in Fig. 53. The frequency increases with decreasing field, but the shift is relatively moderate and lies within 15 cm^{-1}. The negative slope of Fig. 53 also indicates that O forms an anionic bond to the platinum surface [214, 215]. The smallness of the slope is presumably related to the small polarizability of the bond.
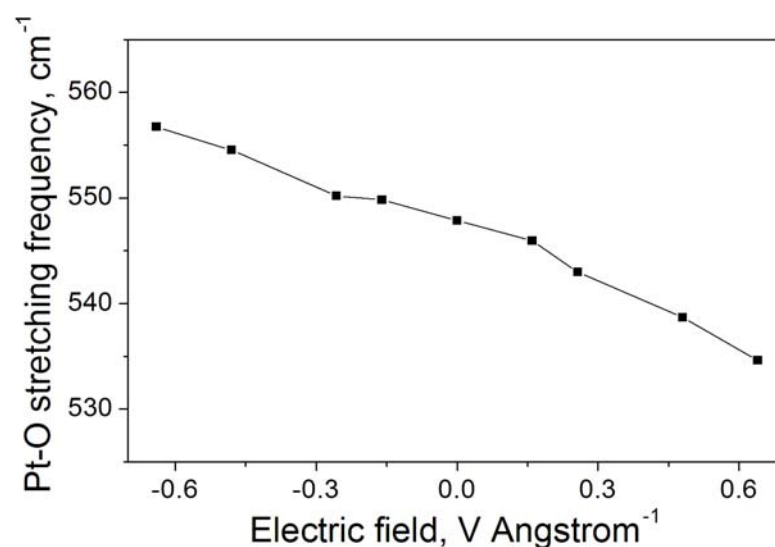
Fig. 53: Pt-O stretching frequency for the O atom adsorbed on a Pt$_9$ cluster at the hollow position as a function of the applied electric field.

4.3.2.3 •OH radical

The •OH radical is one of the most important intermediates of the ORR and is formed in large amounts during the processes of oxygen reduction and water oxidation. Hydroxyl chemisorption was examined at a surface coverage of 1/4 ML for all three low index Pt surfaces. Earlier theoretical studies of the system showed that •OH binds quite strongly at coverages from 1/9 to 1 ML and has an adsorption energy between -2.20 eV and -2.53 eV [95]. At 1/4 ML coverage •OH adsorbs preferentially at the atop and bridge positions (Fig. 54a, Fig. 54b). The third site, with •OH bound between 3 Pt atoms in the hollow position (Fig. 54c), is less favorable.
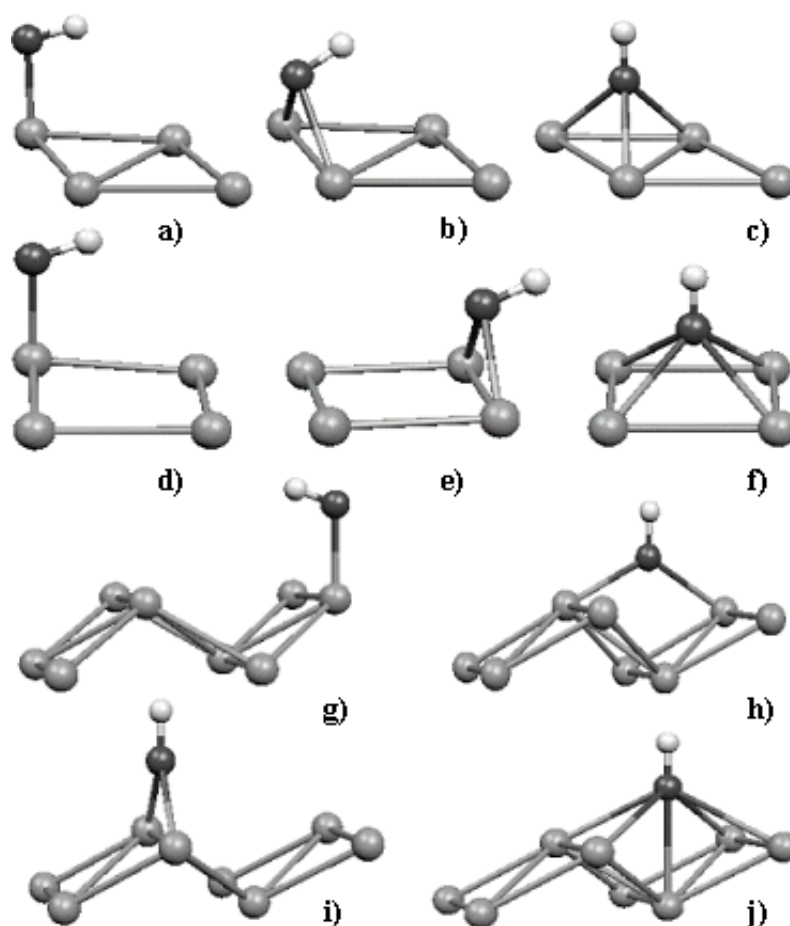
Fig. 54: Hydroxyl adsorbed on low index Pt surfaces; a) atop on (111); b) bridge on (111); c) hollow on (111); d) atop on (100); e) bridge on (100); f) hollow on (100); g) atop on (110); h) long bridge on (110); i) short bridge on (110); j) hollow on (110).

On the (100) surface three adsorption sites were studied. In this case the most stable one is the bridge position between two Pt atoms (Fig. 54e) followed by the atop and hollow positions (Fig. 54d, Fig. 54f).

On the (110) surface, four sites for $^\bullet$OH adsorption were studied. As with the (111) surface, the atop position (Fig. 54g) has the highest adsorption energy of -2.71 eV. $^\bullet$OH adsorbs also between two Pt atoms of the first layer at the long bridge and short bridge positions (Fig. 54h, Fig. 54i). The hollow position between four Pt atoms in the first layer and one Pt atom in the second layer (Fig. 54j) is less stable with an adsorption energy of -1.55 eV. Some selected properties of the adsorbed $^\bullet$OH radicals are given in Table 8.

Table 8: Selected properties of the hydroxyl adsorbed on low index Pt surfaces derived from the VASP (PW91-GGA/PAW) results for the four-layer slab.

Adsorption site	Adsorption energy, eV	Pt-O bond length, Å	O-H bond length, Å
Atop (111)	-2.23	1.99	0.983
Bridge (111)	-2.14	2.19×2	0.983
Hollow (111)	-1.80	2.23×3	0.976
Atop (100)	-2.38	1.98	0.980
Bridge (100)	-2.74	2.11×2	0.981
Hollow (100)	-2.02	2.41×4	0.983
Atop (110)	-2.71	1.98	0.980
Long bridge (110)	-2.25	2.28×2	0.980
Short bridge (110)	-2.53	2.09×2	0.975
Hollow (110)	-1.55	1) 2.76×4 2) 2.63	0.984

A remarkable conclusion from the results in Table 8 in comparison to Table 7 is that whereas the oxygen atom adsorbs weakest on Pt(100), the hydroxyl species adsorbs strongest on Pt(100). As mentioned in the FUNDAMENTALS, Pt(100) is also the surface which is the least active for the ORR in alkaline and perchloric acid media.

Fig. 45 shows the charge transfer function for the hydroxyl radical adsorbed at the atop position of the (111) surface. Here, $^\bullet$OH is predicted to act as an acceptor of electron density from Pt.

In the cluster calculations, the $^\bullet$OH radical adsorbed on the $Pt_9(111)$ cluster accepts a charge of 0.26 a.u. from the Pt atoms, with the hydrogen atom losing 0.07 a.u. of its 1s-population, the 2s-population of the O atom decreasing by 0.06 a.u., and the 2p-population, in contrast, increasing by 0.39 a.u. The molecular orbital involved in the charge transfer is $1\pi^*$ of the $^\bullet$OH [210].

The electric field dependence of the Pt-OH bond is shown in Fig. 55.
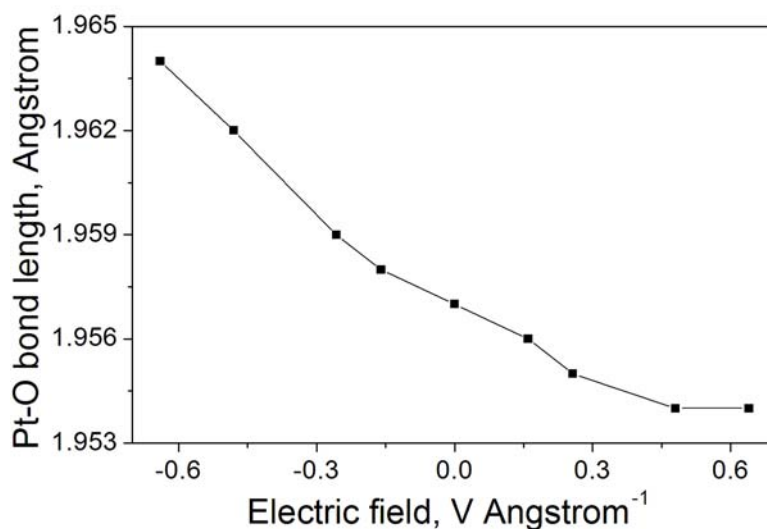
Fig. 55: Pt-O distance in the system Pt_9-OH for the atop adsorption site as a function of the applied electric field.
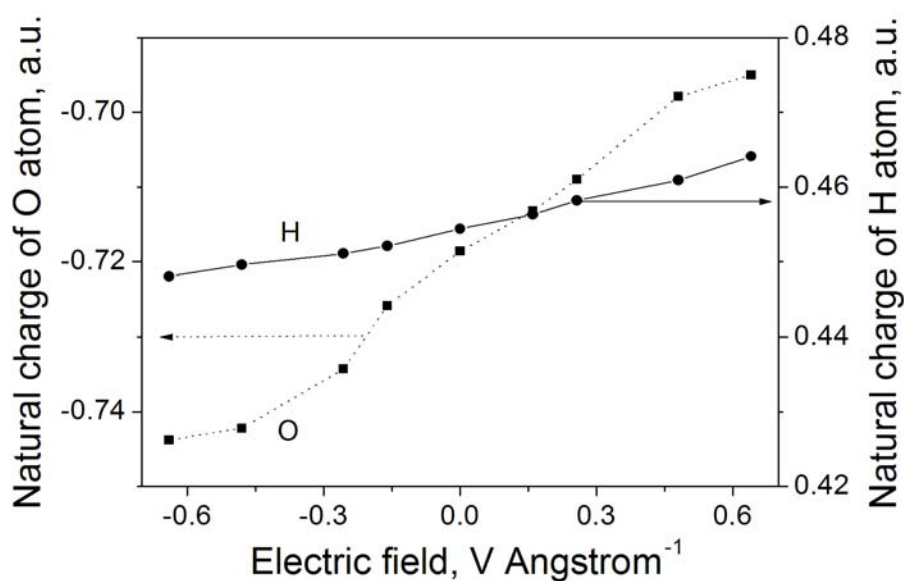
Fig. 56: Natural atomic charges of the O and H atoms in hydroxyl adsorbed on a Pt_9 cluster at the atop position as a function of the applied electric field.

In contrast to the Pt_9-O_2 system, in the case of adsorbed $^\bullet$OH the Pt-OH bond becomes longer for more negative fields (Fig. 55). Both, the O and H atoms become more negatively charged (Fig. 56).

Fig. 57 shows O-H and Pt-(OH) stretching frequencies of the hydroxyl adsorbed on a Pt_9(111) cluster as a function of applied electric field. At zero electric field O-H stretching frequency in the $^\bullet$OH radical adsorbed on Pt(111) surface is ca. 3722 cm^{-1}, in a good agreement with an experimental value of 3735 cm^{-1} [91]. The increase of the electron transfer from the Pt to $^\bullet$OH$_{ads}$ with more negative field weakens the internal O-H bond, and as a result the O-H frequency decreases. The Pt-(OH) stretching frequency decreases as well, as the $^\bullet$OH$_{ads}$ is pushed away from the surface.
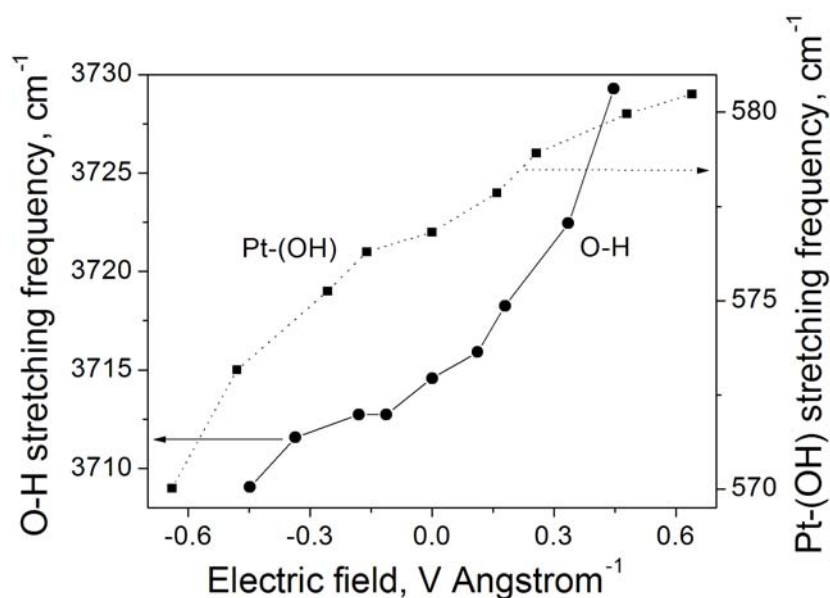
Fig. 57: O-H and Pt-OH stretching frequencies of the $^\bullet$OH adsorbed on a Pt_9 cluster at the atop position as a function of the applied electric field.

4.3.2.4 $^\bullet$OOH radical

The adsorption properties of another intermediate of oxygen reduction, the $^\bullet$OOH superoxide radical, were also studied. Sidik *et al.* calculated an activation energy for $^\bullet$OOH dissociation on Pt_2 of 0.06 eV. The activation energy remains small for larger Pt clusters [68].

It was found that on a (111) surface the only stable configuration is the bridge position between two Pt atoms (Fig. 58). $^\bullet$OOH has an adsorption energy of -1.07 eV. The Pt-O distances are 2.03 and 2.64 Å. The larger distance corresponds to the H-bonded O atom. The

O-O and O-H bond lengths are 1.45 and 0.99 Å, respectively. On (100) and (110) surfaces the radical was found to be unstable and dissociated into $^\bullet OH_{ads}$ and O_{ads}.

Fig. 58: $^\bullet$OOH adsorbed at the bridge position on the Pt(111) surface.

The charge transfer function of the superoxide radical adsorbed on the (111) surface is shown in Fig. 45. The charge is transferred from the Pt slab to the adsorbed radical which acts as an acceptor of electron density.

The properties of the adsorbed superoxide radical on the $Pt_9(111)$ cluster as a function of the applied electric field are similar to those of the oxygen molecule. The O-O bond length in the adsorbed radical increases with decreasing electric field up to almost 1.39 Å (Fig. 59), compared to 1.33 Å for the uncoordinated species in the gas phase. At the same time the radical moves closer to the Pt surface, i.e. the Pt-O bond length decreases. The field dependence of the O-H bond length is not so pronounced. With decreasing field from +0.64 to -0.64 V Å^{-1} the O-H bond shortens from 0.99 to 0.98 Å compared to 0.98 Å in the gas phase.
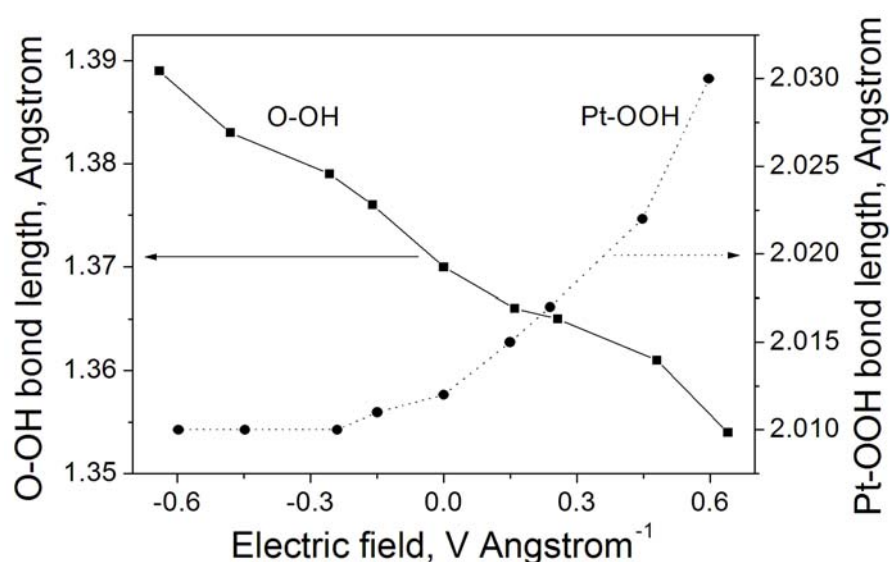
Fig. 59: O-OH and Pt-OOH distances in the system Pt_9-OOH for the bridge adsorption site as a function of the applied electric field.

Adsorption of the superoxide radical on the Pt surface causes charge transfer and redistribution in the whole system. The charge is transferred from the *d*-orbitals of the Pt atoms mostly to the 2*p*-orbitals of the O atoms. Compared to the gas phase the population of 2*p*-orbitals of the oxygen atoms without applied electric field increases by 0.15 a.u. and 0.04 a.u., the latter value corresponding to the H-bonded O atom. At the same time the hydrogen atom loses 0.05 a.u. of its 1*s*-population and becomes more positively charged.
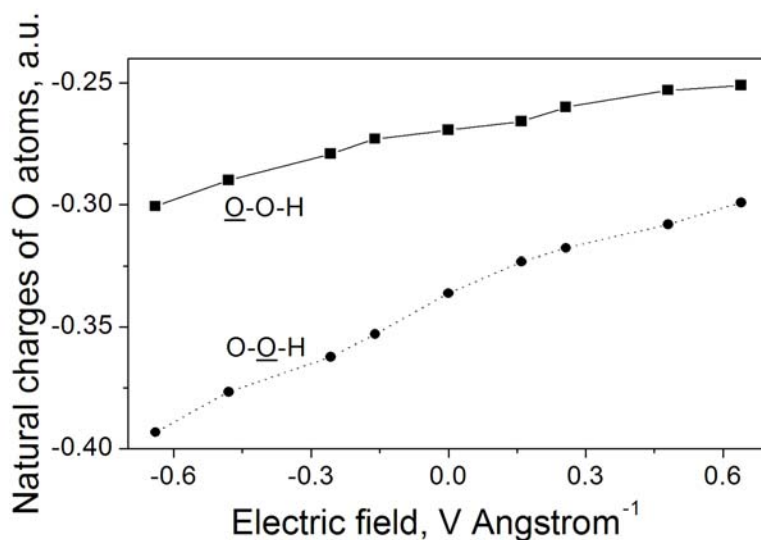
Fig. 60: Natural atomic charges of the O atoms in the superoxide radical adsorbed on a Pt_9 cluster at the bridge position as a function of the applied electric field.
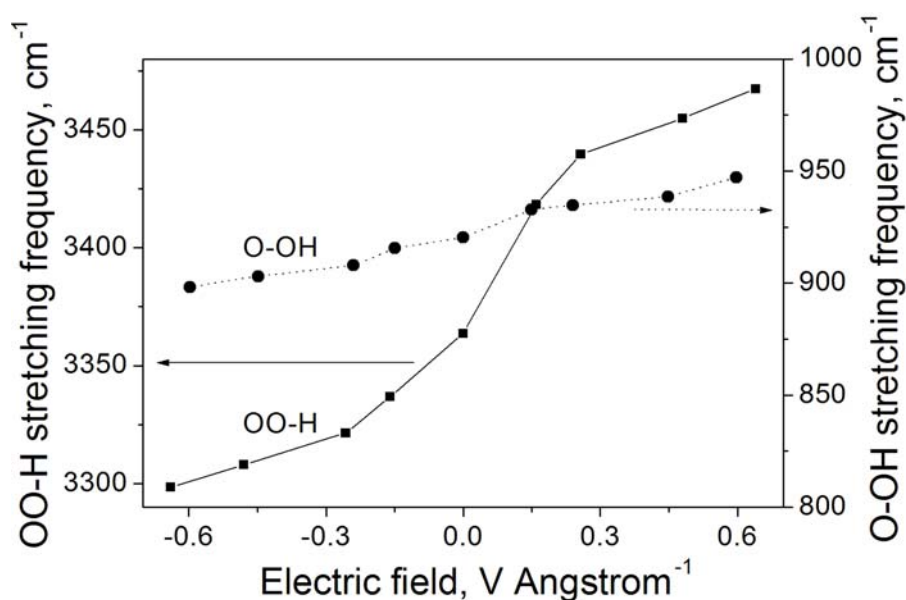
Fig. 61: OO-H and O-OH stretching frequencies of the superoxide radical adsorbed on a Pt_9 cluster at the bridge position as a function of the applied electric field.

Fig. 60 depicts the natural atomic charges of the O atoms in the adsorbed superoxide radical as a function of applied electric field. The H-bonded oxygen atom bears more negative charge than the other oxygen and has a more pronounced field dependent charge transfer.

As a result of the charge transfer the O-O and O-H stretching frequencies decrease with more negative field (Fig. 61). These frequencies for the uncoordinated species in the gas phase have been calculated to be 1163 and 3467 cm^{-1}, respectively (experimental values are 1097.6 and 3436.2 cm^{-1} [207]).

4.3.2.5 H_2O_2

It is well known that during oxygen reduction hydrogen peroxide can be formed as a product or intermediate product on low index Pt surfaces [70, 101]. Therefore, adsorption properties of H_2O_2 on (111), (100), and (110) surfaces were investigated, but in our calculations H_2O_2 was unstable and dissociated into two adsorbed hydroxyls on all three low index Pt surfaces. A second possibility for H_2O_2 decomposition is the formation of a water molecule and an O atom. Both paths and their relevance for fuel cells are discussed in section 4.3.4.

4.3.3   Influence of coadsorbed water

As it was already mentioned in the previous sections, water is an indispensable component of the processes on Pt surfaces in real electrochemical systems. Its presence affects the properties of adsorbed species dramatically.

The adsorption of water on metal surfaces is complex. Previous theoretical studies of the water adsorption on Pt surfaces showed that the water molecule interacts strongly with the Pt surface through the higher energy level lone pair of the water molecule and takes a parallel orientation. For the applied positive electric fields the charge transfer interaction between the water molecule and the Pt surface dominates and the water molecule is adsorbed at the top site on Pt(111). For negative fields the interaction between the dipole moment of the water molecule and the electric field is dominant over the charge transfer interaction [216].

It is well known that water does not adsorb as isolated molecules at temperatures at which the molecules are sufficiently mobile, but tends to form clusters in which water molecules are

connected by hydrogen bonds [217]. The value of these hydrogen bonds is of the same order of magnitude as the water adsorption energy. Hydrogen bonding leads to electron transfer from the proton donor to the acceptor in the bonding region between the water molecules participating in the hydrogen bond formation [105]. This charge redistribution is greatly enhanced in the adsorbed water layer, indicating that the hydrogen bonds are strengthened in the adsorbed phase. The enhancement of the hydrogen bonds upon adsorption is dramatically different from the usual picture of adsorbate-adsorbate interaction, which should, according to Pauling's principle, be reduced when they make bonds with other atoms at the surfaces.

In order to study the influence of coadsorbed water on physical and chemical properties of oxygen molecules and hydroxyl, calculations of these species were performed in the presence of two water molecules per unit cell. For this a new unit cell consisting of two layers with 8 Pt atoms in each layer was built. The extension of a layer size allows coadsorption of two H_2O molecules to the adsorbed O_2 (or $^\bullet OH$) and satisfies periodic boundary conditions. But in order to have reasonable calculation times we had to omit two layers of Pt and consider only two layers. This reduction of the Pt substrate thickness is not critical for the correct description of the adsorption properties of the species of interest. Our test calculations of the adsorption energy for the O_2 on the new unit cell revealed that its deviation from the four-layer slab calculations lies within 130 meV.

4.3.3.1 O_2 with two coadsorbed water molecules

The influence of water coadsorption was studied for the hollow (fcc) and bridge positions on the Pt(111) surface, for the bridge and short bridge positions on Pt(100) and Pt(110) surfaces, respectively. The adsorption geometries are shown in Fig. 62.

Table 9 summarizes some selected properties of the O_2 molecule on Pt surfaces in the presence of coadsorbed water. The adsorption energy was calculated for the adsorption of the O_2 molecule on a Pt surface with relaxed water molecules.

As it was in the case of adsorption under UHV conditions, the adsorption on Pt(110) at the short bridge reveals the highest adsorption energy of all three surfaces suggesting that it is still the preferred adsorption site on a polycrystalline Pt substrate. However, the adsorption energy is not strongly influenced by the water. The presence of coadsorbed water on Pt(111) and Pt(100), in contrast, leads to a strong increase of the adsorption energies for all three studied sites due to stabilization by water molecules. Formation of hydrogen bonds on Pt

substrates gives rise to the O-O bond elongation on low index Pt, making O_2 molecules more labile towards electrochemical reactions. At the same time hydrogen bonding does not affect Pt-O distances to a large extent (compare Table 6 and Table 9).
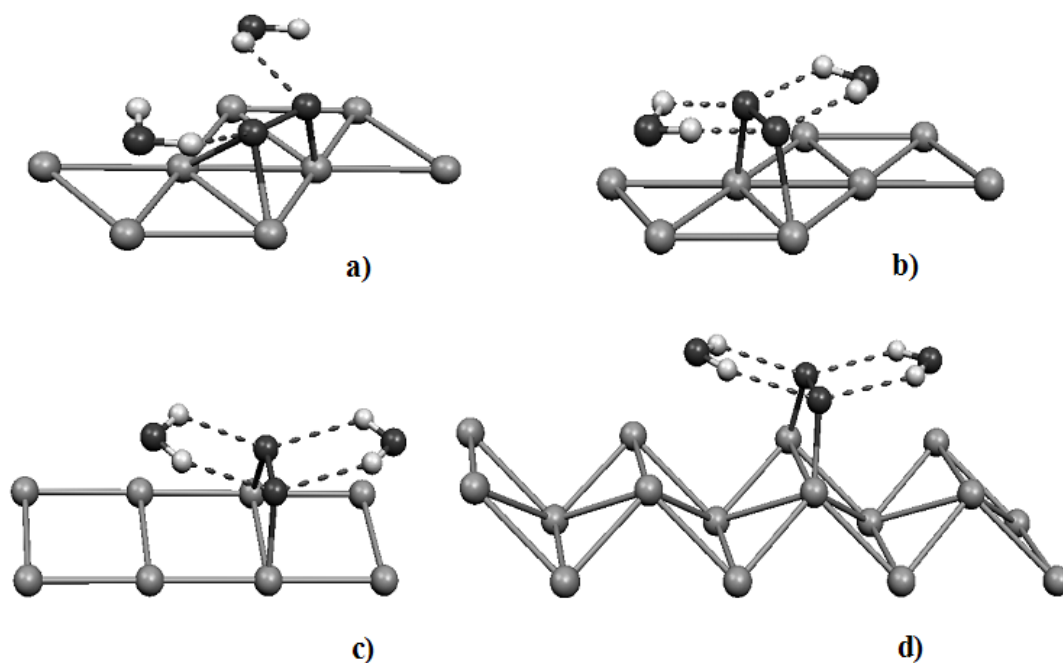
Fig. 62: Oxygen molecule and two water molecules coadsorbed on low index Pt surfaces; a) O_2 lies in the hollow position on (111); b) O_2 lies in the bridge position on (111); c) O_2 lies in the bridge position on (100); d) O_2 lies in the short bridge position on (110).

Table 9: Selected properties of the O_2 molecule coadsorbed with two water molecules on low index Pt surfaces derived from the VASP (PW91-GGA/PAW) results for the two-layer slab.

Adsorption site	Adsorption energy, eV	Pt-O bond length, Å	O-O bond length, Å
Hollow (111) fcc	-1.04	1) 2.06 2) 2.19 3) 2.32	1.41
Bridge (111)	-1.27	2.07×2	1.49
Bridge (100)	-1.22	2.00×2	1.41
Short bridge (110)	-1.56	1.99×2	1.40

Analogous studies of the system demonstrated that the hydrated protons react with the adsorbed O_2 molecules on the Pt(111) under the formation of the chemisorbed $^\bullet$OOH species, which has a significant barrier of approximately 0.4 eV, whereas the barrier of its decomposition is only about 0.1 eV [218]. In acidic aqueous solutions the proton transfer occurs very fast to form a proton-transfer intermediate H^+-O-O$\cdots$Pt(111), which has a much higher electron affinity than O_2 due to the proton field, and consequently induces the subsequent electron transfer from the Pt slab. The electron would be more readily transferred from the negatively charged slab; however, subsequent relaxation of the proton-transfer intermediate including its dehydration requires a much longer time for acceptance of further charge, probably due to the stronger electrostatic attraction between the charged slab and the intermediate, whereas the interaction is much weaker for the uncharged case. The chemisorbed $^\bullet$OOH decomposes into the adsorbed hydroxyl and atomic oxygen [218] in agreement with out results.

4.3.3.2 $^\bullet$OH with two coadsorbed water molecules

The adsorption of hydroxyl in the presence of two coadsorbed water molecules was studied for the atop position on Pt(111) and bridge and short bridge positions on Pt(100) and Pt(110), respectively. The adsorption geometries are shown in Fig. 63.
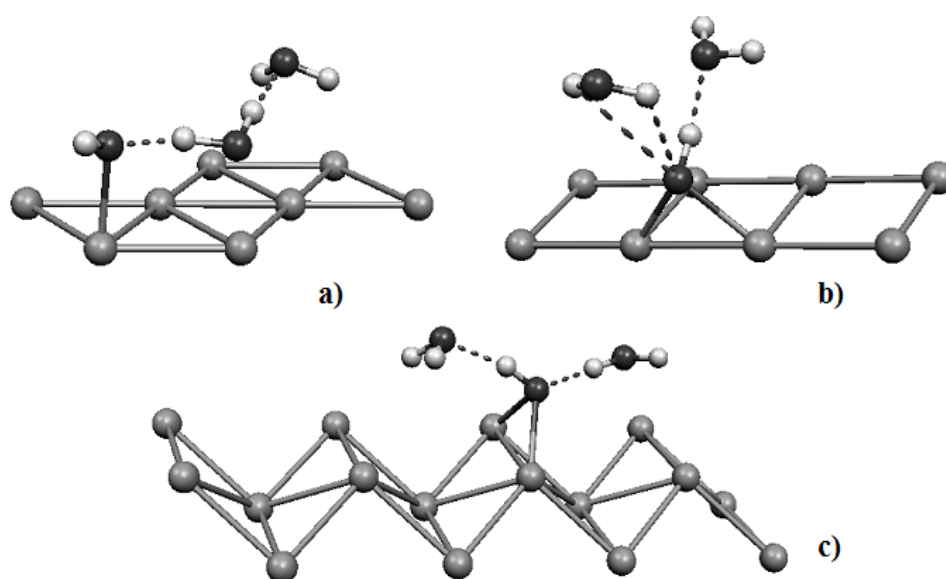
Fig. 63: Hydroxyl and two water molecules coadsorbed on low index Pt surfaces; a) $^\bullet$OH lies in the atop position on (111); b) $^\bullet$OH lies in the bridge position on (100); c) $^\bullet$OH lies in the short bridge position on (110).

Table 10 summarizes some selected properties of the hydroxyl on Pt surfaces in the presence of coadsorbed water. The adsorption energy was calculated for the adsorption of $^{\bullet}$OH on a Pt surface with relaxed water molecules.

Table 10: Selected properties of the hydroxyl species coadsorbed with two water molecules on low index Pt surfaces derived from the VASP (PW91-GGA/PAW) results for the two-layer slab.

Adsorption site	Adsorption energy, eV	Pt-O bond length, Å	O-H bond length, Å
Atop (111)	-3.21	2.07	0.978
Bridge (100)	-3.43	2.08×2	1.017
Short bridge (110)	-3.54	2.12×2	1.009

The presence of coadsorbed water gives rise to hydrogen bond formation, which increases the adsorption energy for all studied adsorption sites as it is known from previous theoretical studies [95]. A most prominent effect is found for (111) and (110) surfaces where the formation of hydrogen bonds increases the adsorption energy by roughly 1.0 eV. The hydroxyl becomes more stable on these Pt surfaces with stabilization on (110) surface being more pronounced. The hydroxyl at the bridge position on Pt(100) – the most stable configuration under UHV conditions also increases its adsorption energy, by 0.69 eV. A very interesting fact of the significant increase of the adsorption energy for the $^{\bullet}$OH species in the presence of coadsorbed water due to the strong stabilization effect via hydrogen bonds can be considered in understanding of the increased membrane degradation under dry operation conditions. The $^{\bullet}$OH species are bound less strongly than in the presence of water and desorb from the catalyst surface to participate in membrane degradation reactions.

Hydrogen bonding moves hydroxyl closer to the Pt surface for the bridge position on (100), but on (111) and (110) surfaces $^{\bullet}$OH moves away from the Pt surface. H-bonding increases O-H bond length for the bridge and short bridge positions on (100) and (110) surfaces, respectively (compare Table 8 and Table 10). The elongation of Pt-O bond length should lead to the increased mobility of the $^{\bullet}$OH species on the Pt surfaces.

It was found recently that in the (OH + H$_2$O)/Pt(111) system the hydroxyls and water molecules form "rings" with every O atom coordinated to three H atoms. The Pt-OH and Pt-OH$_2$ bond lengths were calculated to 2.11 Å and 2.17 Å, respectively, in a good agreement

with our findings. This phase is considered to be an intermediate in the H_2O formation reaction on Pt(111) [95].

The hydrated hydroxyl within the adlayer of $^\bullet OH/H_2O$ on metal surfaces can be represented by the basic structural unit $^\bullet OH(H_2O)_2$ composed of the $^\bullet OH$ itself and the two complexing H_2O molecules [98]. Similarly to the case of a hydroxyl ion OH^- in bulk liquid water, the migration of the $^\bullet OH$, is determined by the vibrational motion of the oxygens. The hydrogen hopping from H_2O to $^\bullet OH$ is along the hydrogen bond and is equivalent to an effective transfer of a hydroxyl in the opposite direction. The rate-limiting step is the rearrangement of the oxygen centers. While there is no long-range mass transfer of oxygens or hydrogens, the apparent diffusion coefficient of $^\bullet OH$ in the presence of water on the surface is $3 \times 10^{-9}\,m^2\,s^{-1}$ [98]. This suggests that the $^\bullet OH$ transfer may play a key role in (electro)catalytic processes on the metal surfaces, or alternatively $^\bullet OH$ can migrate into the bulk water solution.

4.3.4   Relevance for fuel cells

In the previous sections I have presented the results of periodic and cluster-based DFT studies of O_2, O, $^\bullet OOH$, $^\bullet OH$, and H_2O_2 adsorption and properties on three low index Pt surfaces [(111), (100), and (110)] in order to obtain insight into the reduction mechanism of O_2 under conditions relevant for PEMFCs. Oxygen reduction is one of the key processes in low temperature fuel cells, and it has a great impact on the performance, stability, and reliability of the entire fuel cell system.

From our VASP adsorption energies it is possible to construct the energetic pathways of the reaction on Pt. These adsorption energies were obtained in the absence of an electric potential, and would formally correspond to the potential of zero (total) charge. Fig. 64a - c show energy diagrams of water formation on three low index surfaces.

The calculations use one oxygen and two hydrogen molecules in the gas phase and a relaxed Pt surface as reference, and we keep this stoichiometry throughout the reaction. For these diagrams the adsorption energies of molecular hydrogen were calculated to be -0.88 eV, -1.17 eV, and -0.14 eV for (111), (100), and (110) surfaces, respectively. It depends on the electrochemical potential of the anode and is therefore somewhat semantic whether the adsorbed species is called atomic hydrogen or proton. At the cathode we followed the policy

to calculate only the neutral adsorbates, i.e. each reduction step was accompanied by protonation.
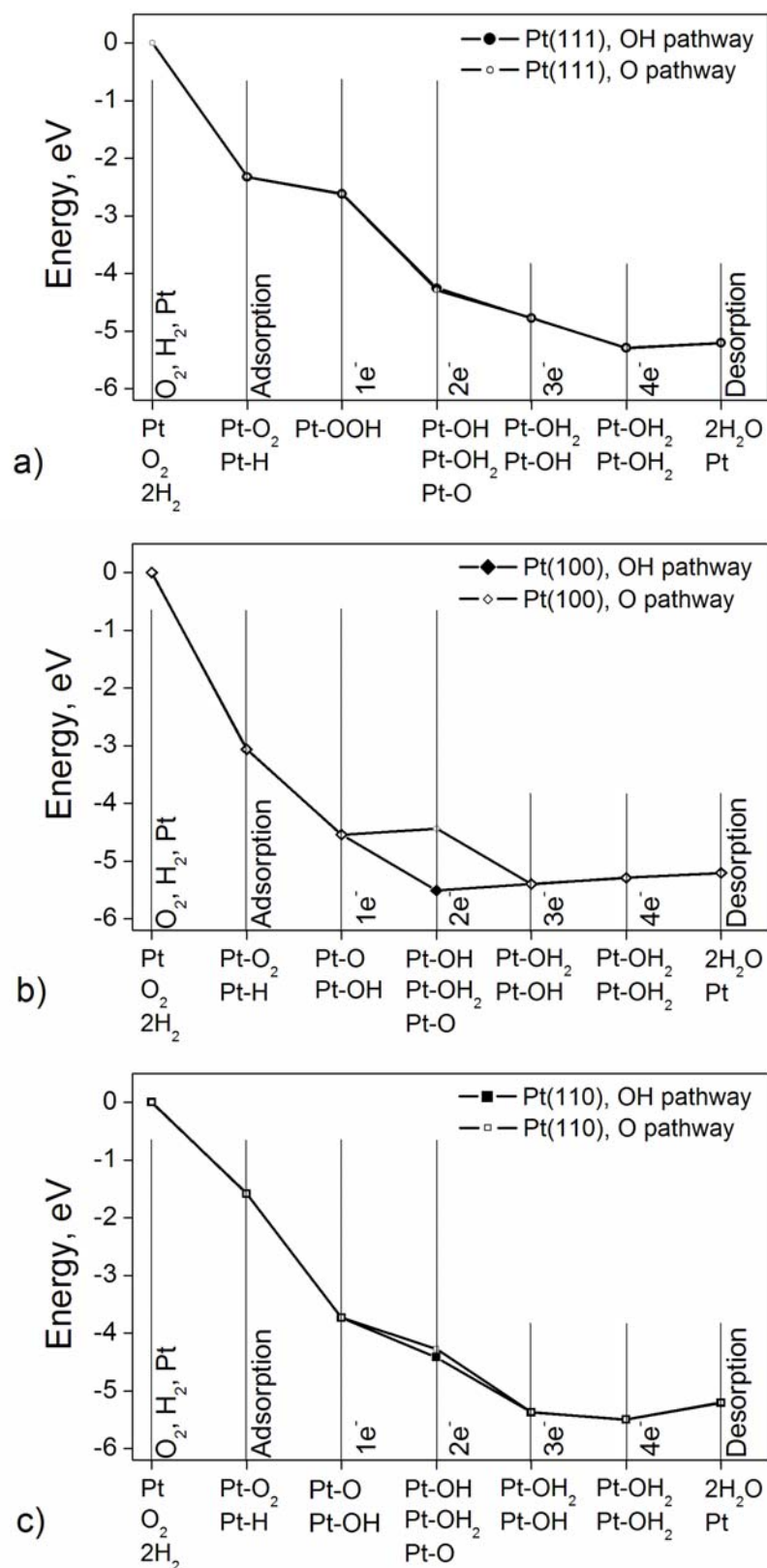
Fig. 64: Energy diagram of the oxygen reduction on a) Pt(111) surface; b) Pt(100) surface; c) Pt(110) surface. Intermediates of the reduction are shown on the horizontal axis.

121

At the relevant cathode potentials, the oxygen species presumably reacts directly with a proton (or hydronium ion) from solution rather than with adsorbed hydrogen. The effects of solvation or interactions with counterions are not considered at this stage.

In the first step we let the reactants adsorb on the Pt surface, whereby we assume that H_2 adsorbs dissociatively and O_2 molecularly. In the second step the oxygen molecule is reduced by one electron to form a superoxide $^\bullet$OOH radical on the (111) surface (Fig. 64a), and an atomic oxygen and a hydroxyl radical on the (100) and (110) surfaces (Fig. 64b - c). In homogeneous aqueous solution, addition of the first electron to O_2 is unfavorable by -0.33 V [219]. On all crystal faces considered here it is at least exothermal. After two-electron reduction we have basically two possibilities: formation of two hydroxyl radicals or the formation of atomic oxygen and a water molecule. Note that at this point the O-O bond is already broken on all Pt surfaces. The possible formation of hydrogen peroxide is prevented by its instability on Pt. H_2O_2 decays into hydroxyl radicals, or into atomic oxygen and a water molecule. As one can see in Fig. 64b - c, the former path is preferred for the (100) and (110) surfaces, and only on the (111) surface both paths are energetically similar (Fig. 64a). The formation of hydroxyl radicals is very important for the fuel cell, since it is believed that the $^\bullet$OH radical is the main agent that leads to the membrane degradation [34].

The $^\bullet$OH radicals adsorb very strongly on the (100) surface (Table 8). This fact explains the energy increase in the following reduction steps on this surface. The surface is poisoned by the OH species, and this fact may reduce the activity dramatically [67, 72]. On the (111) and (110) surfaces the reduction can proceed more easily, decreasing the total energy without any hindrances with low activation energy [68]. After four-electron reduction we obtain the end product – water. This step is followed by water desorption from the Pt surface into the electrolyte. The desorption is entropically driven, at least when the product water is gas phase water.

The calculated enthalpy of water formation amounts to -250.8 kJ mol^{-1}. This is in good agreement with the experimental value of -241.8 kJ mol^{-1}. Because of the decrease of the number of gas molecules the overall entropy decreases in the fuel cell reaction. This is mostly translational entropy. After the adsorption step this translational entropy is already lost, and ΔH should be very close to ΔG for each catalytic step.

Fig. 64a - c were constructed in order to compare relative activities of the three low index Pt surfaces in the ORR because it is considered to be a convenient "overall" way of comparing. According to the present study, the best surface for the oxygen reduction seems to be the (111) facet, since it produces a continuous decrease in energy, with no minimum. The

(110) surface should have a similar activity, but the (100) surface should have a reduced activity because of the strong adsorption of OH species. Experimental results in alkaline and perchloric acid media support this proposal [72].

The presence of electric potentials on the electrochemical interfaces gives rise to nonspecific electrostatic effects for adsorbed species upon surface bonding [220]. Electric potentials influence the properties of adsorbed species and can also control chemical reactions on the electrode surface. Thus, it was shown recently that for a PEMFC which was fed directly with reformed hydrogen in the presence of CO, increasing the anode potential to values at which CO is oxidized to CO_2 (0.6 V) led to a significant increase of the fuel cell performance because the poisoned catalyst surface was cleaned during the applied current pulses [12]. It is therefore of principal importance to study the effects of electrode potential on the properties of adsorbed reactants and intermediates (oxygen molecule and oxygen containing species in our case) to understand and control electrochemical processes on the electrode surface.

Electrode potentials different from the potential of zero (total) charge were modeled by an electric field perpendicular to the Pt surface. For a double layer of approximately 3 Å thickness the range of applied fields corresponds to potentials in the range of -1.92 to +1.92 V versus the potential of zero charge. It was shown that a double layer thickness of 3 Å gives very good agreement of the experimental Stark tuning slopes for CO adsorbed on Pt electrodes in aqueous electrolyte with the calculated ones [81, 82, 145]. Nevertheless, the presence of interspersed Nafion® chains and the proximity of three-phase boundaries in real fuel cells could affect the effective dielectric constant and therefore the double layer thickness locally. Furthermore, the thickness of the double layer can be affected by the potential itself: the larger the difference between the electrode potential and the potential of zero charge is, the smaller is the Debye-Hückel length [221].

The mentioned electric potential limits will adjust depending on the variation of the double layer thickness and the local dielectric constant. The natural limits will be determined by the reactions of the solvent, and this range will normally be narrower than the one used in the present calculations. The electric field intensities employed in our study are therefore believed to cover most of the cases which can arise for oxygen reduction on Pt in a fuel cell.

The presence of an electric potential affects the geometries, charges and adsorption energies of the species on a catalyst surface quite dramatically. When a current is drawn from the fuel cell the anode potential is changed to more positive values, whereas the cathode potential is changed negatively. It means that in our field dependent calculations we go from

positive electric fields towards negative ones. With more negative potential, the oxygen molecule moves closer to the Pt surface, with the O-O bond getting weaker as can be seen from the O-O bond length (Fig. 46) and stretching frequency (Fig. 49). The population of the antibonding π^*-orbital increases. These conditions should facilitate the O-O bond breaking. The same is applicable for the O-O bond in the $^\bullet$OOH radical. It is interesting to note that for the adsorbed oxygen atom negative fields make the Pt-O bond stronger, as can be seen from the Pt-O stretching frequencies (Fig. 53). The $^\bullet$OH radical moves away from the surface, even though the Pt-(OH) frequency does not change much (Fig. 55, Fig. 57). One of the possible consequences is the fact that under heavy fuel cell loads the radical leaves catalyst surfaces more easily, the degradation activity increases. Thus, we observed $^\bullet$OH radicals during fuel cell operation in the formed water by means of the spin trapping technique (see section 4.2.3.2) [187].

The present results were obtained for UHV conditions, but when one studies electrochemical reactions, the electrode is in contact with liquid water, and under fuel cell conditions the catalyst is covered with H_2O molecules to a large extent. The solvation of the adsorbed O_2 and $^\bullet$OH increases their adsorption energy dramatically. The decrease of the adsorption energy can be one of the reasons for the increased membrane degradation under the dry fuel cell operation, when $^\bullet$OH species can leave the surface of the electrocatalyst more easily and attack the membrane. The solvation makes the O_2 species accessible for the hydrated protons which leads to the enhanced reactivity in the ORR in comparison to the UHV conditions as discussed in previous sections. In the presence of coadsorbed water radical intermediates formed during oxygen reduction can change their properties significantly, they can even leave the surface of an electrocatalyst [79, 98] to recombine in bulk solution, or to participate in membrane degradation reactions [34].

At the operation conditions of PEMFCs where the oxygen reduction takes place at 350 K at a three-phase interface consisting of the gas phase, a water-swollen membrane, and the catalyst surface, the ORR mechanisms are far more complex than at the O_2/pure Pt interface, and they depend on several factors such as interactions among hydrated protons, polymer, and water with O_2 and the rest of the intermediate species and products, in the presence of various adsorbates such as OH^- and acid groups from the polymeric membrane, as well on the electrode potential [218].

Charter 5

5 SUMMARY

The present work deals with the investigation and characterisation of different processes which take place in a working PEMFC. This manuscript is divided into two parts. On part of chapter 4 is dedicated to the results and the interpretation of the experimental research (sections 4.1 and 4.2). The SQUID technique was used to investigate magnetic properties of the electrode material. The EPR was the main approach to investigate the radical formation in a working fuel cell. The other part comprises the results and discussion of the quantum chemical calculations of the O_2 and its reduction intermediates adsorption on low index Pt surfaces (sections 4.3).

The motivation for the first part of the work was to understand the processes of membrane degradation which leads to the dramatic reduction of the PEMFC performance after the extended use. It is possible to separate the causes of degradation into three main components: mechanical, thermal, and chemical degradation [222].

Most proton exchange membranes in use rely on the presence of 20 - 40% water by volume for proton conductivity. The water, in turn, provides a pathway for hydrogen and oxygen crossover from opposite sides of the membrane. The diffusion rates are slow and generally represent only a 1 - 3% loss in fuel cell efficiency at some reasonable current density; however, the oxygen crossover does provide a means for the formation of peroxide and hydroperoxide radicals, which can slowly deteriorate the membrane. Traces of transition metals, like Fe^{2+} and Cu^{2+} ions can facilitate membrane degradation from peroxides. Dry operation of a fuel cell can lead to high concentrations of H_2O_2 due to decreased PEM pore water content. The loss of sulfonic groups has been mapped across the thickness of polystyrene sulfonic acid, resulting in formation of sulfobenzoic acid, *p*-benzaldehyde, sulfonic acid, formaldehyde, and large quantities of low-molecular-weight polystyrene sulfonic acid, as detected in product water. It is well known that Nafion® PEMs show highly efficient and stable performance; however, fluoride ions as well as water-soluble, low-molecular-weight perfluorosulfonic acid were found in the product water along with evolved CO_2. It was assumed before that the majority of membrane degradation, associated with the

125

loss of ion exchange capacity, occurs on the H_2 side and is caused by the molecular oxygen diffusion from the cathode side to react with atomic hydrogen chemisorbed on the surface of the platinum anode catalyst to produce peroxide and hydroperoxide. Reduction of the formed hydrogen peroxide is inhibited at the H_2-covered Pt electrode. It accumulates at the H_2-covered Pt/PEM interface and diffuses into the PEM.

Studies of the fuel cell components and *in situ* EPR

Conventional *in situ* analysis of fuel cells is limited mostly to static and dynamic electrochemical methods, in particular current-voltage characteristics and impedance spectroscopy or cyclovoltammetry. On the basis of acquired data it is possible to study degradation processes (including membrane degradation) in a working fuel cell indirectly. It was our main purpose to develop a method which permits the direct observation and monitoring of radical formation *in situ* in a working fuel cell in order to prove or correct known assumptions of the membrane chemical degradation processes. The work aims at an understanding of the pathways of oxidative degradation of membranes, and it wants to provide guidance in the choice of favorable fuel cell operating conditions and in the preparation of alternative membranes with improved durability. For this a miniature fuel cell which can operate in a resonator of an X-band EPR spectrometer was constructed. The power density characteristics of the cell is approximately 50 times worse than that of the up-to-date best fuel cell systems because our cell is not optimized for the operation under high current densities; the contact between the membrane and catalyst particles is poor. However, the processes in the working *in situ* fuel cell are valid for all low temperature fuel cells, thus it can be used for our studies without any loss of the commonness. The fuel cell was equipped with GDEs and also with CCMs without a gas diffusion layer. The fuel cell equipped with the GDEs revealed an EPR signal, whereas the cell without a gas diffusion layer, e.g. equipped only with CCM was EPR silent.

In order to understand the nature of the EPR signal from the *in situ* EPR fuel cell equipped with GDEs, EPR and SQUID techniques were used. The GDEs based on the plane weave carbon with different Pt loadings $(0.00 - 2.00 \, \text{mg cm}^{-2})$ and Pt on Vulcan XC-72 with different Pt content $(0 - 20\%)$ as well as pure Pt black were considered. The GDE material has an EPR signal with a *g* value of 2.0030 and a peak-to-peak line width of approximately 3 G. The signal is considered to be assigned to localized spins associated with defects independent of the graphite π electrons. The signal intensity decreases with increasing Pt loading and strongly depends on the air humidity. The GDE samples with and without Pt show essentially

different line width behavior as a function of temperature that can be explained in terms of changing the nature of radical centers. Without plane weave carbon support, Vulcan XC-72 carbon material reveals a signal with a *g* value of 1.9980 and a peak-to-peak line width of approximately 78 G. The signal is considered to be assigned to π electron spins. With increasing Pt content the signal decreases and disappears at the Pt content of 20%. SQUID measurements of GDE magnetization properties indicate that magnetization is determined by the diamagnetic contribution from the plane weave carbon (~99 wt% of the GDE). Pt black reveals Pauli paramagnetism which diminishes with increasing carbon content.

It is known that the degradation of a membrane in a working fuel cell is caused by the $^\bullet$OH and $^\bullet$OOH radicals formed during incomplete oxygen reduction. We modeled the degradation of the membrane components sPEKH, PBI, and A 501 via $^\bullet$OH radical attack. For this, the water suspensions of these polymers containing hydrogen peroxide and the POBN spin trap were irradiated with the UV light to decompose H_2O_2 molecules into hydroxyl radicals. For the sPEKH no radical formation was observed, probably due to the poor accessibility of the polymer particles for the $^\bullet$OH radicals. It is known, however, that the membrane in a fuel cell is saturated with water and can be reached by the radical species in its hydrophilic regions. The PBI and A 501 polymers, in contrast, revealed pronounced EPR signals from the POBN-$^\bullet$R radical adducts, demonstrating that these polymers can be attacked by the $^\bullet$OH radicals. The anisotropic character of the signal in case of the PBI polymer indicates that the radicals are fixed on the water insoluble polymer particles. The higher mobility of the radicals in the case of the A 501 polymer causes narrowing of the lines.

The $^\bullet$OH and $^\bullet$OOH radicals, responsible for the membrane degradation, can be formed at the cathode side of the fuel cell. Because of the partial oxygen crossover through the membrane these radicals can be formed at the anode side as well. The concentration of free radicals produced in a fuel cell is extremely low and their lifetime is relatively short, so that it is not possible with conventional methods to observe them directly. We therefore employed the spin trapping technique, using the spin trap molecules POBN, DMPO, DBNBS, and DEPMPO. Radical formation was studied separately at the anode and cathode side of the *in situ* EPR fuel cell.

At the anode side of the cell formal addition of hydrogen atoms to the spin trap molecules was observed. However, experiments with D_2O solution of the POBN spin trap and D_2 as a fuel revealed that the process of H atom addition proceeds in two steps. At the first step the spin trap molecule is reduced to the anion-radical which reacts afterwards with ambient water (H_2O or D_2O) to form the hydrogen (deuterium) atom adduct. Hydrogen atoms from the

feeding gas do not react with a spin trap. If ethanol was added to the POBN spin trap water solution at the anode side, products of ethanol partial oxidation ($^\bullet C_2H_4OH$) were detected in addition to the hydrogen atom adduct since ethanol itself can act as a fuel and was oxidized in a working fuel cell.

At the cathode side we were able to demonstrate the $^\bullet OH$ radical formation during the oxygen reduction by introducing the DMPO spin trap water solution into the cell equipped with the Nafion$^\circledR$ 115 membrane. In the experiments with POBN ethanol-water solution it was shown that the $^\bullet OH$ radicals are able to oxidize ethanol to $CH_3^\bullet CHOH$ and $^\bullet CH_2CH_2OH$ radicals which can be detected using the POBN spin trap.

The formed $^\bullet OH$ radicals manifested their destructive nature when F-free membranes were used instead of a very stable Nafion$^\circledR$ membrane. They attacked the membrane and formed different organic radicals on the membrane surface. The formation of radicals was confirmed by the addition of a spin trap water solution at the cathode side. Nitrone (POBN, DMPO, and DEPMPO) and nitroso (DBNBS) spin traps were employed. The spin trap molecules react with the radicals under formation of the stable spin trap adducts. Due to the fact that the radicals are immobilized, mobility of the formed adducts is hindered to some extent, which is proven by the increased line width and anisotropic character of the recorded EPR signals.

It was also shown that the introduction of the radical scavenger decreases the concentration of the radicals on the membrane surface, at least within experimental time range. Only a very weak signal was observed for the modified membrane even after 20 minutes of closed circuit operation. However, long term stability tests are necessary in order to come to a decision whether the improvements have provisional or permanent character.

In general, we develop a novel method employing the spin trapping technique which allows one to "peek" inside a running fuel cell and monitor both wanted and unwanted electrochemical processes selectively. At the anode, free radical intermediates of the fuel conversion reaction are trapped, and at the cathode the spin trap attaches to radical defects on the proton-conducting polymer membrane. The latter is particularly significant since these defects result from membrane degradation. This observation will allow researchers to determine within minutes the electrochemical operating conditions which lead to degradation of their new membranes, an information of extreme importance for an improved fuel cell lifetime.

It is interesting to note that no traces of degradation were detected at the anode side of the fuel cell for any membrane used. The $^\bullet OH$ and $^\bullet OOH$ radicals formed via oxygen crossover

through the membrane and incomplete reduction at the anode catalyst were not detected either. Thus, numerous experimental data and speculations about membrane degradation at the anode side in literature could not be confirmed. This can be due to the very low concentration of the oxygen containing radicals at the anode and/or the preference of the spin trap reaction path leading to the H-adducts. However, the spin trapping technique can be very valuable for the investigation of oxidation mechanisms for different fuels potentially interesting for the fuel cell applications.

Quantum chemical calculations of O_2 and its reduction intermediates on low index Pt surfaces

As it was shown in *in situ* fuel cell spin trap experiments oxygen containing radicals are deemed important in understanding the degradation effects in a working fuel cell. In the theoretical part of the manuscript we investigated the energetics of the oxygen reduction reaction intermediates on Pt surfaces in the conditions relevant for the fuel cells. The presence of applied electric fields and coadsorption of water were considered.

The adsorption properties of the oxygen molecule and intermediates of the ORR on the (111), (100), and (110) platinum surfaces were calculated in the DFT-GGA framework (PW91-GGA/PAW) using periodic boundary conditions and a slab model of the Pt surface. The electric field dependence of the adsorbate properties was studied using a cluster model of the adsorption system. The B3LYP functional and a 6-311G** basis set for the O and H atoms and a LANL2DZ basis set for the Pt atoms were employed in this case.

The oxygen molecule has two preferential adsorption sites on the (111) surface, which are the hollow and the bridge positions, with adsorption in a bridge fashion being the most favourable. O_2 at the hollow position bears more negative charge and is best referred to as a peroxolike O_2^{2-} state. The charge transfer at the bridge position is smaller, therefore the oxygen molecule forms the superoxolike O_2^{-} state here. These assignments are also supported by the O-O internal vibrational frequencies in their respective adsorbed states. Even if the peroxolike adsorbate is more polar, the superoxolike adsorbate in the bridge position is found to be much more polarizable. This remarkable feature may be ascribed to the fact that in the peroxo-state, the $2\pi^*$-orbital is "saturated" with electrons, whereas in the superoxo-state, it may still accept electrons.

On the (100) and (110) surfaces, O_2 adsorbs mostly at the bridge positions between two Pt atoms. The product of oxygen dissociation in the gas phase, atomic oxygen, lies in the threefold and fourfold hollows on the (111) and (100) surfaces, respectively. The bridge

position is preferred for the (110) facet. The formation of O_{ads} via electrochemical oxygen reduction is not energetically beneficial in comparison to the formation of $^\bullet OH$ radicals. The probable formation of atomic oxygen after the first electron reduction and decay of the $^\bullet OOH$ ($^\bullet OO^-$) radical could be followed by the reaction with water molecules present on Pt to form two adsorbed hydroxyl radicals [223]. But the most probable way of forming surface-bonded $^\bullet OH$ is through water oxidation [78].

Hydroxyl radicals may adsorb at the atop, hollow, and bridge positions on all three surfaces, with the atop position preferred for the (111) and (110) and the bridge position preferred for the (100) surface. $^\bullet OH$ on the (100) surface has the highest adsorption energy for low index Pt planes, which may explain why this particular surface shows the lowest activity for the ORR in alkaline and perchloric acid media.

The $^\bullet OOH$ radical was found to be stable only at the bridge position on the Pt(111) surface, whereas on other surfaces it decayed into $^\bullet OH$ and O species. Hydrogen peroxide was unstable on all low index Pt surfaces and decayed into hydroxyl radicals, or a water molecule and an O atom. This interesting observation clarifies the known fact that production of H_2O_2 at the fuel cell cathode leads to an enhanced membrane degradation.

The effect of a uniform external electric field on the adsorbate properties on a $Pt_9(111)$ cluster has been studied by means of an *ab initio*, DFT-based, cluster model approach. It is well known that electric potentials influence the properties of adsorbed species and can also control chemical reactions on the electrode surface. For a double layer of approximately 3 Å thickness the range of applied fields corresponds to potentials in the range of -1.92 to +1.92 V versus the potential of zero charge. We believe that the electric field intensities employed in the study cover most of the cases which can arise for oxygen reduction on Pt in a fuel cell. For all adsorbed species the applied electric field is predicted to have a strong impact and to cause considerable changes in the bond lengths, charge transfer characteristics and vibrational frequencies.

The presence of coadsorbed water on the catalyst surfaces was modeled by the coadsorption of two water molecules together with the O_2 and $^\bullet OH$ species. The presence of water leads to the formation of hydrogen bonds and strengthens the adsorption significantly. The increased membrane degradation under the dry operation conditions can be due to the fact that the formed $^\bullet OH$ species are bound less strongly and can desorb from the Pt catalyst surface to participate in membrane degradation reactions.

It is known that under conditions relevant for the fuel cells, solvated O_2 on the catalyst surface may react with a hydrated proton resulting in a proton-transfer intermediate

H^+-O-O$\cdots$Pt(111), which has a much higher electron affinity than O_2 due to the proton field, and consequently induces the subsequent electron transfer from the Pt slab to form chemisorbed $^\bullet$OOH. The $^\bullet$OOH species is unstable and decays into $^\bullet$OH$_{ads}$ and O$_{ads}$. In the presence of coadsorbed water the $^\bullet$OH species are known to have very high mobility on catalyst surfaces, thus the $^\bullet$OH translational motion may play a key role in (electro)catalytic processes on the metal surfaces, or alternatively $^\bullet$OH can migrate into the bulk water solution (into the PEM) and participate in degradation processes.

In general, at the operation conditions of PEMFCs, the O_2 reduction mechanism is far more complex than on pure Pt under UHV conditions. A number of factors such as interactions with hydrated protons, polymer, and water with O_2 and the rest of the intermediate species and products, in the presence of various adsorbates such as OH$^-$ and acid groups from the polymeric membrane, as well as the electrode potential influence the reduction process and should be considered for the correct description of the system.

The current study demonstrates that DFT methods are capable of effectively describing adsorption geometries, charge transfers and vibrational frequencies of the oxygen containing species upon adsorption on low index Pt surfaces. We believe that the present study provides new insights into the complicated problem of oxygen reduction in particular in low temperature fuel cell applications.

Further work in a similar direction should take into account the stabilization or destabilization of surface-adsorbed species by coadsorbed water molecules at different coverages in the presence of electric field (potential) in order to understand which influence on the adsorbed species it has and how coadsorbed water affects these impacts.

ZUSAMMENFASSUNG

Diese Arbeit beschäftigt sich mit der Untersuchung und Charakterisierung verschiedener Prozesse, die in einer laufenden PEMFC ablaufen. Von seinem Aufbau her ist das Manuskript zweigeteilt: ein Teil von Kap. 4 widmet sich den Resultaten und der Interpretation der experimentellen Untersuchungen (Kap. 4.1 und 4.2). Die SQUID-Technik wurde verwendet um magnetische Eigenschaften des Elektrodenmaterials zu untersuchen. Die EPR war die Hauptmethode für die Untersuchungen der Radikalbildung in einer laufenden Brennstoffzelle. Der andere Teil umfasst die Ergebnisse der quantenchemischen Rechnungen von der Adsorption des O_2 und seiner Reduktionszwischenprodukte auf "low index" Platin-oberflächen und deren Deutung (Kap. 4.3).

Die Motivation für den ersten Teil war der Wunsch, die Prozesse der Membrandegradation, die zum dramatischen Abbau der Brennstoffzellenleistung nach längerem Einsatz führen, zu verstehen. Es ist möglich, drei verschiedene Gründe für die Membrandegradation zu trennen. Das sind die mechanische, thermische und chemische Degradationen [222].

Die Gründe für den frühzeitigen Ausfall umfassen mangelhafte Befeuchtung, vor allem in der Einlaufzone, wo die Reaktandengeschwindigkeiten sehr hoch sind und entlang den Abdichtungen strömen. Wenn eine Perforation der MEA auftritt, folgt ein rapider Abfall der Zellenspannung, weil Wasserstoff und Sauerstoff in gegenüberliegende Zellenräume einlaufen und auf der Oberfläche des Elektrodenkatalysators reagieren. Die Wärme der Rekombination kann dabei die Membran zum Schmelzen bringen; wodurch die Perforation fortgesetzt wird.

Zurzeit werden die PEMFCs bei ungefähr 80°C betrieben. Die PEMs sind nicht signifikant beeinflusst bis etwa 150°C, wo das meiste Wasser entfernt wird und die Membran an irreversibler Austrocknung leidet. Die thermische Degradation der Membranen in der H^+-Form beginnt üblicherweise mit dem Verlust von Sulfongruppen bei über 200°C. Die Protonleitfähigkeit der meisten Protonaustauschmembranen beruht auf der Gegenwart eines Volumenanteils von 20 - 40% Wasser. Aber das Wasser ist auch das Medium, das die Wasserstoff- und Sauerstoffüberführung auf die gegenüber liegenden Seiten ermöglicht. Die Diffusionsgeschwindigkeiten sind klein und machen bei mäßigen Stromdichten nur einen Verlust von 1 - 3% aus. Dennoch bietet die Sauerstoffdiffusion den Weg für die Peroxid- und Hydroperoxidradikalbildung, die zur langsamen Membrandegradation führen. Spuren von

132

Übergangsmetallen, z.B. Fe^{2+}- und Cu^{2+}-Ionen, können die Membrandegradation durch Peroxide fördern. Der trockene Betrieb einer Brennstoffzelle führt zu hohen Konzentrationen von H_2O_2 auf Grund eines reduzierten Wassergehalts in den Poren. Der Verlust von Sulfongruppen wurde quer durch die Polystyrolsulfonsäuremembran untersucht. Dadurch entstehende Benzoesulfonsäure, *p*-Benzaldehyd, Sulfonsäure, Formaldehyd und große Mengen von niedermolekularer Polystyrolsulfonsäure wurden nachgewiesen. Es ist gut bekannt, dass Nafion® PEMs hocheffizientes and stabiles Verhalten ausweisen, aber dennoch wurden sowohl Fluoridionen als auch wasserlösliche niedermolekulare Perfluorsulfonsäure zusammen mit gebildetem CO_2 im Produktwasser gefunden. Es wurde angenommen, dass die meisten Degradationsprozesse, die mit dem Verlust der Ionenaustauschkapazität verbunden sind, auf der Wasserstoffseite auftreten und durch die Diffusion von molekularem Sauerstoff von der Kathodenseite hervorgerufen sind. O_2 reagiert mit chemisorbiertem atomarem Wasserstoff auf der Anodenkatalysatoroberfläche und bildet Peroxide und Hydroperoxide. Die Reduktion von Wasserstoffperoxid auf der mit Wasserstoff bedeckten Elektrode ist gehindert, H_2O_2 diffundiert in die PEM hinein und entwickelt seine destruktive Natur.

Untersuchungen der Brennstoffzellenkomponenten und *in situ* EPR

Konventionelle *in situ* Analyse der Brennstoffzellen beschränkt sich auf die statischen und dynamischen elektrochemischen Methoden, insbesondere Strom-Spannungscharakteristika und Impedanzspektroskopie oder Zyklovoltammetrie. Aufgrund der Daten, die mittels dieser Methoden erhalten werden können, ist es möglich, indirekte Aussagen über die Degradationsprozesse (darunter auch die Membrandegradation) der Brennstoffzelle zu machen. Es war unser Hauptziel, eine Methode zu entwickeln, welche die direkte Beobachtung und ein Monitoring der Radikalbildung *in situ* in einer laufenden Brennstoffzelle ermöglicht, um die bekannten Annahmen für die chemischen Membrandegradationsprozesse zu beweisen oder zu korrigieren. Die Arbeit strebt ein Verständnis der oxidativen Membrandegradationspfade an und will eine Beratung für die Wahl günstiger Betriebsbedingungen der Brennstoffzellen und für die Herstellung alternativer Membranen mit einer verbesserten Alterungsbeständigkeit liefern. Um diese Ziele zu erreichen, wurde eine Miniaturbrennstoffzelle, die in einem Resonator eines X-Band EPR-Spektrometers betrieben werden kann, gebaut. Die Leistungsdichten der Zelle sind etwa 50 Mal niedriger als für die aktuell besten Brennstoffzellsysteme, weil unsere Zelle für den Betrieb unter hohen Stromdichten nicht optimiert ist; der Kontakt zwischen der Membran und den Katalysatorpartikeln ist mangelhaft. Dennoch sind die Prozesse, die in der laufenden *in*

situ Brennstoffzelle ablaufen, für alle Niedertemperaturbrennstoffzellen gültig. Daher konnte die *in situ* Zelle ohne Verlust der Allgemeingültigkeit für unsere Untersuchungen verwendet werden. Die Brennstoffzelle wurde sowohl mit Gasdiffusionselektroden (GDEs) als auch mit katalysatorbeschichteten Membranen (CCMs) ohne eine Gasdiffusionsschicht ausgerüstet. Die Zelle mit den GDEs wies ein EPR-Signal auf, während die Zelle mit der CCM EPR-inaktiv war.

Um die Natur des EPR-Signals von der mit den GDEs ausgerüsteten *in situ* Brennstoffzelle zu verstehen, kamen EPR- und SQUID-Methoden zum Einsatz. Die GDEs basierend auf Kohlenstoffgewebe mit verschiedener Pt-Beladung ($0.00 - 2.00$ mg cm^{-2}), Pt auf Vulcan XC-72 mit verschiedenem Pt-Gehalt ($0 - 20\%$) und pures Platinpulver wurden untersucht. Das GDE-Material wies EPR-Signal mit *g*-Faktor 2,0030 und eine Peak-to-Peak Linienbreite von etwa 3 G auf. Das Signal stammt von lokalisierten Spins, die mit den Defekten verbunden und von π-Elektronen im Graphit unabhängig sind. Die Signalintensität nimmt mit der Zunahme der Pt-Beladung ab und hängt von der Luftfeuchtigkeit ab. Die Linienbreite des Signals von GDEs mit und ohne Pt in Funktion der Temperatur verhält sich grundsätzlich anders, was darauf hindeutet, dass die Radikalzentren ihre Natur und Eigenschaften ändern. Ohne Kohlenstoffgewebe zeigt pures Vulcan XC-72 Material ein Signal mit *g*-Faktor 1,9980 und Peak-to-Peak Linienbreite von etwa 78 G. Das Signal stammt von π-Elektronen. Mit steigendem Pt-Gehalt nimmt die Signalintensität ab und verschwindet beim Pt-Gehalt von 20%. SQUID-Untersuchungen von magnetischen Eigenschaften der GDE deuteten an, dass die Magnetisierung hauptsächlich vom diamagnetischen Anteil des Kohlenstoffes bestimmt wird (~ 99 wt% der GDE). Pures Platinpulver weist Pauli-Paramagnetismus auf, der mit die Abnahme des Pt-Gehalts mit entsprechender Zunahme des Kohlenstoffanteils abnimmt.

Es ist bekannt, dass die Membrandegradation in einer laufenden Brennstoffzelle von $^\bullet$OH und $^\bullet$OOH Radikalen, die während der unvollständigen Sauerstoffreduktion gebildet werden, verursacht wird. Wir haben die Degradation der Membrankomponenten sPEKH, PBI und A 501 durch $^\bullet$OH Radikalangriff modelliert. Dafür wurden Wassersuspensionen dieser drei Polymere mit Wasserstoffperoxid in Gegenwart der POBN-Radikalfalle mit UV-Licht bestrahlt, um die H_2O_2-Moleküle zur Dissoziation zu bringen. Fürs sPEKH wurde keine Radikalbildung nachgewiesen, vermutlich infolge der mangelhaften Zugänglichkeit der Polymerpartikel für die $^\bullet$OH Radikale. Dennoch ist bekannt, dass die Membran in einer Brennstoffzelle mit dem Wasser gesättigt und für die Radikalspezies in ihren hydrophilen Bereichen zugänglich ist; die Membran kann dort angegriffen werden. Die PBI- und A 501-

Polymere hingegen zeigten ausgeprägte EPR-Signale der POBN-$^\bullet$R Radikaladdukte, was darauf hindeutet, dass diese Polymere von den $^\bullet$OH Radikalen angegriffen werden konnten. Der anisotrope Charakter des Signals im Falle des PBI-Polymers deutet darauf hin, dass die gebildeten Radikale auf dem wasserunlöslichen Polymer befestigt sind. Die hohe Beweglichkeit der Radikale im Falle des A 501-Polymers resultierte in schmaleren Linien des Spektrums.

Die $^\bullet$OH- und $^\bullet$OOH-Radikale, die für die Membrandegradation verantwortlich sind, können auf der Kathodenseite der Brennstoffzelle gebildet werden. Aufgrund der partiellen Sauerstoffüberführung durch die Membran können diese Radikale auch auf der Anodenseite entstehen. Die Konzentration der freien Radikale in einer Brennstoffzelle ist äußerst gering und ihre Lebensdauer ist relativ kurz. Also ist es nicht möglich, diese Radikale mit konventionellen Methoden nachzuweisen. Deswegen haben wir die Radikalfallenmethode auch *in situ* eingesetzt, und die Radikalfallen POBN, DMPO, DBNBS und DEPMPO kamen zum Einsatz. Die Radikalbildung wurde separat auf der Anoden- und der Kathodenseite der *in situ*-EPR-Brennstoffzelle untersucht.

Auf der Anodenseite wurde formale Addition von Wasserstoffatomen an Radikalfallenmoleküle nachgewiesen. Fig. 65a stellt das EPR-Spektrum vom POBN-$^\bullet$H dar. Experimente mit D_2O Lösung von POBN und D_2 als Brenngas zeigten, dass der Prozess der H-Atom Addition in zwei Stufen abläuft. In der erste Stufe wird die Radikalfalle zum Anion-Radikal reduziert, gefolgt von der Protonierungreaktion mit dem Wasser aus der Umgebung (D_2O bzw. H_2O). Dadurch wird das H- bzw. D-Addukt gebildet. Es gibt keine direkte Reaktion zwischen Wasserstoffatomen vom Brenngas mit den Radikalfallen. Wenn Ethanol zur Radikalfallenlösung beigemischt wurde, wurden die Produkte der partiellen Oxidation des Ethanols ($^\bullet C_2H_4OH$) zusätzlich zum H-Addukt detektiert. In diesem Fall diente Ethanol auch als Brennstoff, der in der laufenden Brennstoffzelle oxidiert werden kann.

Auf der Kathodenseite wurde die $^\bullet$OH-Bildung während der Sauerstoffreduktion nachgewiesen. Dafür wurde wässrige DMPO-Radikalfallenlösung in der mit der Nafion$^\circledR$-115-Membran ausgerüsteten Zelle eingesetzt. Fig. 65b zeigt das EPR-Spektum vom DMPO-$^\bullet$OH Radikaladdukt. In Experimenten mit der wässrigen POBN-Ethanollösung wurde gezeigt, dass die $^\bullet$OH Radikale in der Lage sind, Ethanol zu $CH_3{}^\bullet CHOH$- und $^\bullet CH_2CH_2OH$-Radikalen zu oxidieren, die mittels POBN Radikalfalle abgefangen und anschließend detektiert werden konnten.

Die gebildeten $^\bullet$OH Radikale machten ihre destruktive Natur deutlich, wenn F-freie Membranen anstelle der stabilen Nafion$^\circledR$-Membran eingesetzt wurden. Sie griffen die

Membran an und bildeten verschiedene organische Radikale auf der Membranoberfläche. Die Bildung von Radikalen wurde bewiesen, indem Radikalfallenlösungen hinzugegeben wurden. Nitroso- (DBNBS) und Nitronradikalfallen (POBN, DMPO und DEPMPO) wurden verwendet. Radikalfallenmoleküle reagierten mit gebildeten organischen Radikalen und führten zu stabilen Radikalfallenaddukten. Aufgrund der Tatsache, dass die Radikale immobilisiert sind, sind die EPR-Signale anisotrop. Fig. 65c zeigt das Produkt POBN-•R der Reaktion von POBN-Molekülen mit während der Membrandegradation gebildeten Radikalen •R. Die beschränkte Beweglichkeit der Radikale auf der Membranoberfläche führt zur Verbreiterung der Linien, die vor allem bei hohem Magnetfeld zu sehen ist.
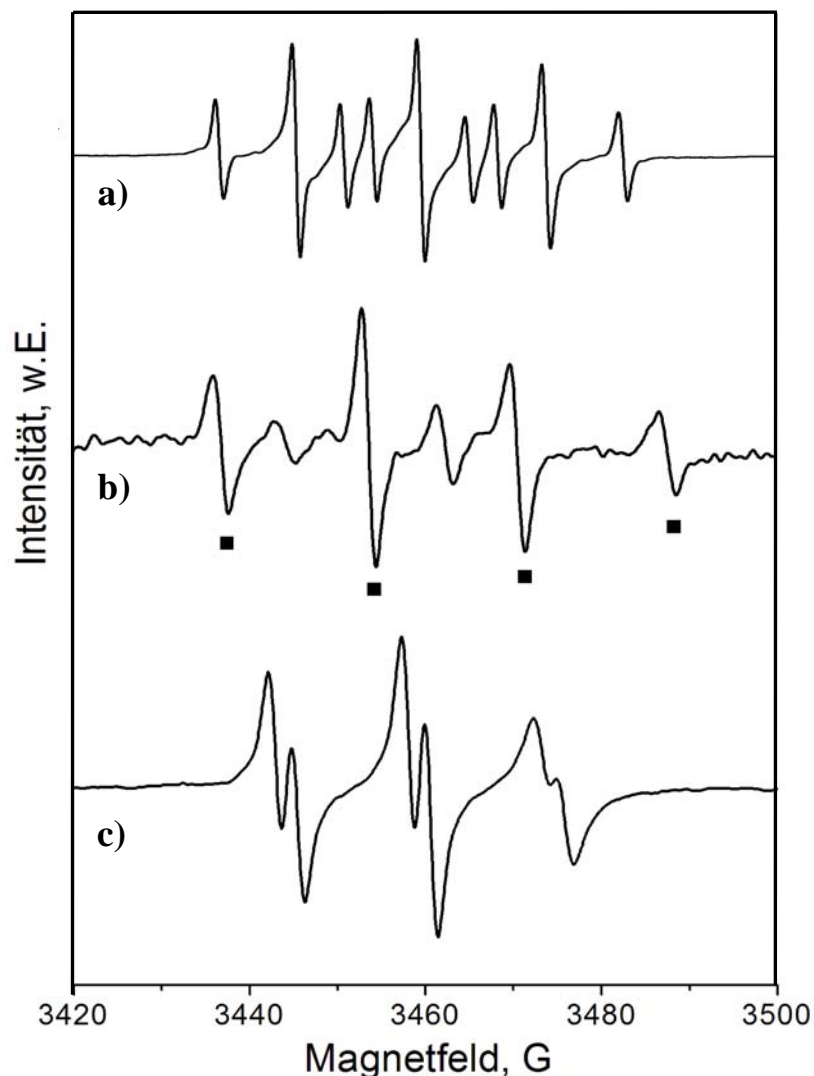

Fig. 65: EPR-Spektren von a) POBN-•H; b) DMPO-•OH von der mit Nafion®-115-Membran ausgerüsteten Brennstoffzelle; c) POBN-•R von der mit der 1025-Membran ausgerüsteten Brennstoffzelle.

Es wurde auch gezeigt, dass die Einführung von Radikalscavenger in die Membran die Konzentration der gebildeten Radikale auf der Membranoberfläche im experimentellen Zeitmaßstab reduziert. Ein Signal von nur sehr geringer Intensität wurde nach 20 Minuten Kurzstromschlussbetrieb beobachtet. Aber langfristige Stabilitätstestexperimente sind erforderlich, um eine präzise Analyse des Einflusses von Radikalscavenger auf die langfristige Membranstabilität zu erlauben.

Zusammenfassend haben wir eine neue Methode basierend auf Radikalfallen entwickelt, die es erlaubt, in eine laufende Brennstoffzelle hineinzuschauen und erwünschte und unerwünschte Prozesse zu überwachen. Auf der Anodenseite werden freie Radikale abgefangen, auf der Kathodenseite wird das Radikalfallemolekül an den Defekten der protonenleitenden Membran befestigt. Das Letzte ist von großer Bedeutung, weil diese Defekte durch die Membrandegradation entstehen. Diese Beobachtung macht es für Wissenschaftler möglich, innerhalb von wenigen Minuten elektrochemische Bedingungen, die zur Degradation ihrer neuen Membranen führen, zu bestimmen. Die erhaltene Information ist sehr wichtig für die Verbesserung der Charakteristika der Membranlebensdauer.

Es ist bemerkenswert, dass für keine der untersuchten Membranen Spuren der Membrandegradation auf der Anodenseite der Brennstoffzelle detektiert wurden. Auch die durch die Sauerstoffüberführung und unvollständige Reduktion auf der Anodenseite gebildeten $^\bullet$OH- und $^\bullet$OOH-Radikale wurden nicht nachgewiesen. Daher konnten zahlreiche experimentelle Daten und Spekulationen aus der Literatur nicht bestätigt werden. Das kann daran liegen, dass die Konzentration von sauerstoffhaltigen Radikalen sehr gering ist und/oder der Radikalfallenreaktionspfad der H-Adduktbildung bevorzugt ist. Dennoch haben die Experimente mit Ethanol gezeigt, dass die Radikalfallenmethode sehr nützlich für die Untersuchung von Oxidationsmechanismen verschiedener Brennstoffe sein kann, die eventuell für die Brennstoffzellen interessant sind.

Quantenchemische Rechnungen zu O_2 und seinen Reduktionszwischenprodukten auf "low index" Pt Oberflächen

In *in situ* Experimenten mit Radikalfallen wurde gezeigt, dass die sauerstoffhaltigen Radikale sehr wichtig sind für das Verstehen der Degradationseffekte in einer laufenden Brennstoffzelle. Im theoretischen Teil der Dissertation untersuchten wir die Adsorptionseigenschaften von Zwischenprodukten der Sauerstoffreduktion auf den Platin-oberflächen unter Bedingungen, die für die Brennstoffzellen relevant sind. Die angelegten

elektrischen Felder und die Gegenwart von Wasser auf der Katalysatoroberfläche wurden in Betracht gezogen.

Die Adsorptionseigenschaften vom Sauerstoff und von Zwischenprodukten der ORR (Sauerstoffreduktionsreaktion) an den (111)-, (100)- und (110)-Platinoberflächen wurden berechnet im Rahmen des DFT-GGA-Ansatzes (PW91-GGA/PAW). Periodische Grenzbedingungen und das Slab-Model wurden angewendet. Die Adsorbateigenschaften wurden in Abhängigkeit vom elektrischen Feld mittels eines Cluster-Modells untersucht. Das B3LYP-Funktional und ein 6-311G**-Basis-Satz für die O- and H-Atome und ein LANL2DZ-Basis-Satz für die Pt Atome wurden in diesem Fall verwendet.

Das Sauerstoffmolekül hat zwei bevorzugte Adsorptionspositionen an der (111)-Oberfläche, die Loch- und Brücken-Positionen. Die Adsorption in der Brücke weist eine größere Adsorptionsenergie auf. O_2 in der Loch-Position hat mehr negative Ladung und kann als peroxi-ähnlicher Zustand O_2^{2-} bezeichnet werden. Der Ladungstransfer ist kleiner für die Brücken-Position, daher befindet sich hier das Sauerstoffmolekül im superoxo-ähnlichen Zustand. Diese Zuordnungen sind auch durch die O-O-internen Schwingungsfrequenzen in entsprechenden Adsorptionspositionen bestätigt. Das peroxi-ähnliche Adsorbat ist polarer, das superoxo-ähnliche dagegen viel mehr polarisierbar. Diese auffallende Besonderheit beruht auf dem Fakt, dass im Peroxo-Zustand das $2\pi^*$-Orbital mit Elektronen „gesättigt" ist, während es im Superoxo-Zustand noch Elektronen aufnehmen kann.

An den (100)- und (110)-Oberflächen adsorbiert O_2 hauptsächlich in den Brücken-Positionen zwischen zwei Platinatomen. Das Produkt der Sauerstoffmoleküldissoziation, atomarer Sauerstoff, liegt in den dreizähligen und vierzähligen Löchern der (111)- bzw. (100)-Oberflächen. An der (110)-Oberfläche ist die Brücken-Position bevorzugt. Die Bildung von O_{ads} durch elektrochemische Sauerstoffreduktion ist im Vergleich zur •OH Radikalbildung energetisch ungünstig. Die wahrscheinliche Bildung von atomarem Sauerstoff nach dem ersten Elektronentransfer und der Zerfall von •OOH (•OO⁻)-Radikal könnte von der Reaktion mit Wassermolekülen, die auf der Pt-Oberfläche präsent sind, gefolgt sein, wobei zwei Hydroxylradikale gebildet werden [223]. Aber die wahrscheinlichste Art, die •OH Radikale an der Platinoberfläche zu bilden, ist die Wasseroxidation [78].

Hydroxylradikale können in den Atop-, Loch- und Brücken-Positionen an allen drei Oberflächen adsorbieren. Die Atop-Position ist an den (111)- und (110)- und die Brücken-Position an der (100)-Oberfläche bevorzugt. An der (100)-Oberfläche hat •OH die größte Adsorptionsenergie für all "low index" Pt Oberflächen. Dies erklärt, warum diese Oberfläche die niedrigste Aktivität für die ORR in alkalischer und saurer ($HClO_4$) Umgebung aufweist.

Das $^\bullet$OOH Radikal war nur stabil in der Brücken-Position von Pt(111), während es auf den anderen Oberflächen in $^\bullet$OH und O-Spezies zerfiel. Wasserstoffperoxid war instabil an den "low index" Pt-Oberflächen und zerfiel in zwei Hydroxylradikale bzw. in ein Wassermolekül und atomaren Sauerstoff. Diese interessante Beobachtung erklärt die bekannte Tatsache, dass die Bildung von H_2O_2 auf der Kathode zur verstärkten Membrandegradation führt. Aufgrund der Adsorptionsenergien wurden die Reduktionspfade an drei Pt-Oberflächen dargestellt (Fig. 66).
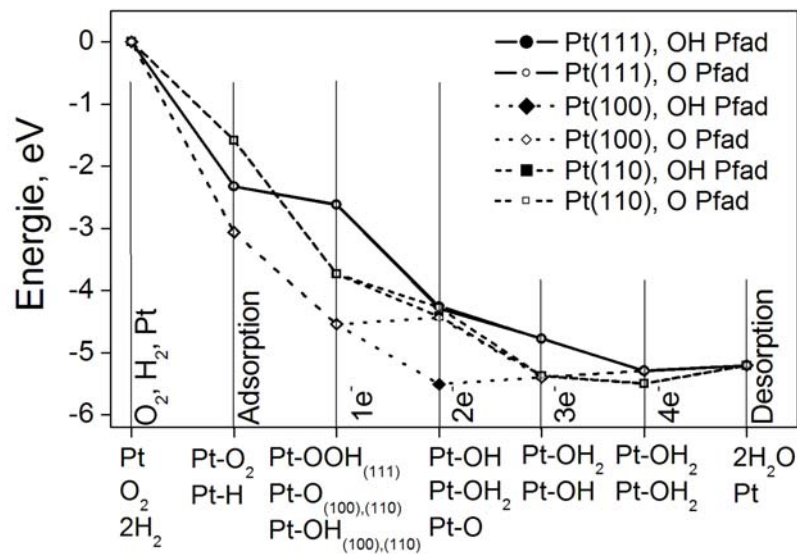

Fig. 66: Reaktionspfade der Sauerstoffreduktion auf den Pt(111), Pt(100) und Pt(110) Oberflächen.

Fig. 66 wurde konstruiert, um die relativen Aktivitäten drei "low index" Pt-Oberflächen für die Reaktion der Sauerstoffreduktion zu vergleichen. Entsprechend unseren Untersuchungen ist Pt(111) die beste Oberfläche für die Sauerstoffreduktion, weil sie ohne Minimum eine ständige Abnahme der Energie aufweist. Die (110)-Oberfläche sollte eine ähnliche Aktivität aufweisen, während die (100)-Oberfläche weniger aktiv ist wegen der starken Adsorption der OH-Spezies.

Der Effekt eines gleichmäßigen elektrischen Feldes auf die Adsorbateigenschaften an dem $Pt_9(111)$ Cluster wurde mittels eines *ab initio* DFT-basierenden Cluster-Ansatzes untersucht. Es ist gut bekannt, dass die elektrischen Potentiale die Eigenschaften von adsorbierten Spezies beeinflussen und auch die chemische Reaktionen an der Elektrodenoberfläche kontrollieren können. Für eine Doppelschicht von etwa 3 Å Dicke entspricht der Bereich angelegter Felder dem Potentialbereich von -1,92 to +1,92 V gegen das Potential der Nullladung. Wir glauben, dass die Intensitäten des elektrischen Feldes, die in der Arbeit

139

verwendet wurden, die meisten Fälle abdecken, die für die Sauerstoffreduktion in einer Brennstoffzelle auftreten können. Für alle untersuchte Adsorbate wird vorhergesagt, dass das angelegte elektrische Feld einen starken Einfluss auf das System hat und beträchtliche Änderungen von Bindungslängen, Ladungstransfereigenschaften sowie von Schwingungs-frequenzen hervorrufen soll.

Die Gegenwart des Wassers auf der Katalysatoroberfläche wurde durch Coadsorption von zwei Wassermolekülen zusammen mit dem O_2 bzw. $^\bullet OH$ modelliert. Das Wasser bildet Wasserstoffbrücken und verstärkt wesentlich die Adsorption im Vergleich zu UHV-Bedingungen. Das kann dazu führen, dass wenn die Gase nicht genug befeuchtet sind und/oder die Brennstoffzelle zu wenig Wasser bildet, die OH-Spezies schwächer am Pt-Katalysator gebunden werden und deswegen leichter desorbieren und mehr Schaden anrichten können. Es ist bekannt, dass unter für die Brennstoffzellen wichtigen Bedingungen solvatisierter O_2 mit dem hydratisierten Proton an der Katalysatoroberfläche reagieren kann, um den Protonenübergangskomplex H^+-O-O$\cdots$Pt(111) zu bilden. Dieser Komplex hat eine viel größere Elektronenaffinität als O_2 wegen des Protonenfeldes, was schließlich den Elektrontransfer von dem Pt auslöst, um chemisorbiertes $^\bullet OOH$ zu bilden. Die $^\bullet OOH$-Spezies sind instabil und zerfallen in $^\bullet OH_{ads}$ und O_{ads}. In Gegenwart von coadsorbiertem Wasser sind die $^\bullet OH$-Spezies auf der Katalysatoroberfläche sehr mobil, dadurch kann $^\bullet OH$ eine entscheidende Rolle in (elektro)katalytischen Prozessen an den Metalloberflächen spielen. Als Alternative dazu können die $^\bullet OH$-Spezies ins umgebende Wasser (in die PEM) diffundieren und an Degradationsprozessen teilnehmen.

Im allgemeinen, unter Betriebsbedingungen von PEMFCs, ist der O_2 Reduktions-mechanismus komplizierter als auf dem reinen Platin im UHV. Mehrere Faktoren müssen betrachtet werden für die korrekte Beschreibung des Systems, z.B. Wechselwirkungen zwischen hydratisierten Protonen, Polymer und Wasser mit dem O_2 und anderen Zwischenprodukten und Produkten in Gegenwart verschiedener Adsorbate wie OH^- und Säuregruppen von der Polymermembran. Aber auch das elektrische Potential beeinflusst den Reduktionsprozess.

Unsere Rechnungen demonstrieren, dass DFT-Methoden für die effektive Beschreibung von Adsorptionsgeometrien, Ladungstransfereigenschaften und Schwingungsfrequenzen für sauerstoffhaltige Adsorbate an "low index" Pt-Oberflächen brauchbar sind. Wir glauben, dass diese Arbeit neue Erkenntnisse über das komplizierte Problem der Sauerstoffreduktion, insbesondere für Niedertemperaturbrennstoffzellen, anbietet.

Weitere Forschung in diese Richtung soll Stabilisierung und Destabilisierung von Adsorbaten durch coadsorbierte Wassermoleküle für verschiedene Bedeckungen in Gegenwart eines angelegten elektrischen Feldes (Potentials) berücksichtigen, um zu verstehen, welchen Einfluss dies auf die adsorbierten Spezies hat und wie das coadsorbierte Wasser diese Effekte beeinflusst.

ACKNOWLEDGEMENT

First of all I would like to thank Prof. Dr. Emil Roduner for giving me the opportunity to make my PhD work in his group. I appreciate very much his permanent support and invaluable discussions on different topics. I thank him very much for his encouragement to perform theoretical *ab initio* studies and giving me the opportunity to learn these techniques in Eindhoven, the Netherlands. I am very grateful that he let me present our activities on numerous conferences, workshops, and seminars.

Taking the chair of the examination board by Prof. Dr. Thomas Schleid is kindly acknowledged. Writing the second advisory opinion by Prof. Dr. Hermann Stoll is also kindly acknowledged.

I thank all my group colleagues contributed to a pleasant atmosphere. In particular Dr. Herbert Dilger for his support with EPR, Linux, and Web administration. Some problems could not be ever solved without his help. Dr. Igor Tkach for the valuable discussions on fuel cells and advanced EPR techniques, Mr. Svetlin Mitov for the valuable discussions on the membrane components degradation.

My thank goes to Dr. Marc Koper from the Schuit Institute of Catalysis, Laboratory of Inorganic Chemistry and Catalysis, Eindhoven University of Technology, the Netherlands and his group members Dr. Steven Mitchell and Dr. Tatyana Shubina for introducing to me Gaussian 98 and VASP packages. They showed to me all the power of modern computational chemistry and taught me how to use it and I am very grateful for this.

I thank Dr. Jochen Kerres and his group members Dr. Martin Hein and Dr. Andreas Ullrich from the Institute for Chemical Processes Engineering, Stuttgart University for providing me with different membranes used in low temperature fuel cells and for the valuable discussions on the membrane chemistry in a working fuel cell.

I thank Dr. Thorsten Schmauke and Dr. George Hübner for introducing to me Linux, for the assistance with EPR measurements and *ab initio* calculations.

CURRICULUM VITAE

Alexander Panchenko

Date of birth, place of birth: 22nd of May 1979, Jarowoje, Russia.

Education:

1986-1996:   Secondary School, Jarowoje, Russia.

1996-2001:   Study of Chemistry at the Novosibirsk State University, Russia, Department of Natural Sciences. Diploma work entitled "Photocatalytic oxidation of aromatic compounds in gas phase over TiO_2".

2001-2004:   Dissertation at the Stuttgart University, Institute of Physical Chemistry, AG-Roduner.

BIBLIOGRAPHY

[1]   G. Carle, *Fuel Cell Today*, 1 (2003).

[2]   S. Barrett, *Fuel Cells Bulletin*, 10 July (2003).

[3]   T. Koppel, *The Ballard Fuel Cell and the Race to Change the World*, John Wiley & Sons (1999).

[4]   K. Kordesch, G. Simander, *Fuel Cells and Their Applications*, VCH Publishers, New York (1996).

[5]   M. Corbett, *Opportunities in Advanced Fuel Cell Technologies V1- Stationary Power Generation 1998-2008*, Kline & Company, Inc., Fairfield, NJ (1998).

[6]   C.E. Thomas, B.D. James, F.D. Lomax Jr., I.F. Kuhn Jr., *Int. J. Hydrogen Energy*, **25**, 551 (2000).

[7]   Z. Jusys, J. Kaiser, R.J. Behm, *Phys. Chem. Chem. Phys.*, **3**, 4650 (2001).

[8]   W.R. Grove, *Phil. Mag.*, **14**, 127 (1839).

[9]   G. Sandstede, *Bunsenmagazin*, **3**, 66 (2000).

[10]   G.G. Scherer, *Sol. State Ionics*, **94**, 249 (1997).

[11]   M. Quintus, Dissertation, Universität Stuttgart (2002).

[12]   L. Carrette, K.A. Friedrich, U. Stimming, *Fuel Cells*, **1**, 5 (2001).

[13]   *Fuel Cell Handbook, Sixth Edition*, by EG&G Technical Services, Inc. Science Applications International Corp., Under Contract No. DE-AM26-99FT40575, U.S. Dept. of Energy, Office of Fossil Energy, National Energy Technology Laboratory, Morgantown, W. Virginia, November (2002).

[14]   Q. Li, R. He, J.O. Jensen, N.J. Bjerrum, *Chem. Mater.*, **15**, 4896 (2003).

[15]   Aldrich, *Technical Information Bulletin*, No AI-163, Aldrich Chemical Company, Inc. P.O. box 355, Milwaukee, WI 53201, USA.

[16]   A. Bosnjakovic, S. Schlick, *J. Phys. Chem. B*, **108**, 4332 (2004).

[17]   C. Huang, K.S. Tan, J. Lin, K.L. Tan, *Chem. Phys. Lett.*, **371**, 80 (2003).

[18]   L. Depre, J. Kappel, M. Poppall, *Electrochim. Acta*, **43**, 1301 (1998).

[19]   B. Bonnet, D.J. Jones, J. Roziere, L. Tchicaya, G. Alberti, M. Casciola, L. Massinelli, B. Baner, A. Peraio, E. Ramunni, *J. New Mat. Electrochem. Systems*, **3**, 87 (2000).

[20]   J. Kerres, A. Ullrich, M. Hein, *J. Pol. Sci.*, **39**, 2874 (2001).

[21]   J. Kerres, *J. Membr. Sci.*, **185**, 3 (2001).

[22] Q. Guo, P.N. Pintauro, H. Tang, S. O'Connor, *J. Memb. Sci.*, **154**, 175 (1999).

[23] J.S. Wairight, J.T. Wang, D. Weng, R.F. Savinell, M.H. Litt, *J. Electrochem. Soc.*, **143**, 1233 (1996).

[24] G. Hübner, Dissertation, Universität Stuttgart (1999).

[25] R. Hodgton, J.R. Boyack, A.B. LaConti, *Advance Development and Technical Report*, No 65DE5, General Electric Co., West Lynn, MA, USA (1966).

[26] N. Aweir, *Eur. Polym. J.*, **14**, 9 (1978).

[27] B. Sangchakr, T. Hisanaga, K. Tanaka, *J. Photochem. Photobiol. A: Chem.*, **85**, 187 (1995).

[28] K. Okamoto, Y. Yamamoto, H. Tanaka, M. Tanaka, *Bull. Chem. Soc. Jpn.*, **58**, 2015 (1985).

[29] H. Wang, G.A. Capuano, *J. Electrochem. Soc.*, **145**, 780 (1998).

[30] F.N. Büchi, B.Gupta, O. Haas, G.G. Scherer, *J. Electrochimica Acta*, **40**, 345 (1995).

[31] G.G. Scherer, *J. Phys. Chem.*, **94**, 1008 (1990).

[32] D.M. Bernardi, M.W. Verbrugge, *J. Electrochem. Soc.*, **139**, 2477 (1992).

[33] R.A. Assink, C. Arnold Jr., R.P. Holladsworth, *J. Membr. Sci.*, **56**, 143 (1991).

[34] G. Hübner, E. Roduner, *J. Mater. Chem.*, **9**, 409 (1999).

[35] D. Behar, J. Rabani, *J. Phys. Chem.*, **92**, 5288 (1988).

[36] H. Kaczmarek, L.A. Linden, J.F. Rabek, *Polym. Degrad. Stab.*, **47**, 175 (1995).

[37] T.R. Ralph, M.P. Hogarth, *Platinum Met. Rev.*, **46**, 3 (2002).

[38] Z. Hou, B. Yi, H. Zhang, *Electrochem. Sol. State Lett.*, **6**, A232 (2003).

[39] M. Wilson, F. Garzon, K. Sickafus, S. Gottesfeld, *J. Electrochem. Soc.*, **140**, 2872 (1993).

[40] R.M. Darling, J.P. Meyers, *J. Electrochem. Soc.*, **150**, A1523 (2003).

[41] S. Gottesfeld, T.A. Zawodzinski, in *Advances in Electrochemical Science and Engineering*, R.C. Alkire, H. Gerischer, D.M. Kolb, C.W. Tobias, eds., p.195, Wiley-VCH, Weinheim (1997).

[42] L.M. Roen, C.H. Paik, T.D. Jarvi, *Electrochem. Sol. State Lett.*, **7**, A19 (2004).

[43] K. Tawara, T. Nishimura, H. Iwanami, T. Nishimoto, T. Hasuike, *Ind. Eng. Res.*, **40**, 2367 (2001).

[44] J.R. Rostrup-Nielsen, *Phys. Chem. Chem. Phys.*, **3**, 283 (2001).

[45] M.M. Mench, H.M. Chance, C.Y. Wang, *J. Electrochem. Soc.*, **151**, A144 (2004).

[46] T. Ioroi, K. Yasuda, Z. Siroma, N. Fujiwara, *J. Electrochem. Soc.*, **150**, A1225 (2003).

[47] S. Mukerjee, S.J. Lee, E.A. Ticianelly, J. McBreen, B.N. Grgur, N.M. Markovic, P.N. Ross, J.R. Giallombardo, E.S. De Castro, *Electrochem. Sol. State Lett.*, **2**(1), 12 (1999).

[48] D. Le, B. Sea, K. Lee, K. Lee, *Ind. Eng. Chem. Res.*, **41**, 3594 (2002).

[49] Q. Li, R. He, J. Gao, J.O. Jensen, N.J. Bjerrum, *J. Electrochem. Soc.*, **150**, A1599 (2003).

[50] V.S. Bagotzky, Y.B. Vassilyev, O.A. Khazova, *J. Electroanal. Chem.*, **81**, 229 (1977).

[51] E. Christoffersen, P. Liu, A. Ruban, H.L. Skriver, J.K. Norskov, *J. Catal.*, **199**, 123 (2001).

[52] U.A. Paulus, A. Wokaun, G.G. Scherer, T.J. Schmidt, V. Stamenkovich, V. Radmilovich, N.M. Markovic, P.N. Ross, *J. Phys. Chem. B*, **106**, 41081 (2002).

[53] G.L. Troughton, A. Hamnett, *Bull. Electrochem.*, **7**, 488 (1991).

[54] J. Choi, K. Park, B. Kwon, Y. Sung, *J. Electrochem. Soc.*, **150**, A973 (2003).

[55] A.B. Anderson, E. Grantscharova, *J. Phys. Chem.*, **99**, 9149 (1995).

[56] P.S. Kauranen, E. Skou, J. Munk, *J. Electroanal. Chem.*, **404**, 1 (1996).

[57] G. Vijayaraghavan, L. Gao, C. Korzeniewski, *Langmuir*, **19**, 2333 (2003).

[58] B. Gurau, R. Viswanathan, R. Liu, T.J. Lafrenz, K.L. Ley, E.S. Smotkin, E. Reddington, A. Sapienza, B.C. Chan, T.E. Mallouk, S. Sarangapani, *J. Phys. Chem. B*, **102**, 9997 (1998).

[59] A. Lima, C. Coutanceau, J.M. Leger, C. Lamy, *J. Appl. Electrochem.*, **31**, 379 (2001).

[60] M. Cappadonia, J.W. Erning, S.M. Saberi Niaki, U. Stimming, *Sol. State Ionics*, **77**, 65 (1995).

[61] M. Ise, K.D. Kreuer, J. Maier, *Sol. State Ionics*, **125**, 213 (1999).

[62] M. Watanabe, H. Uchida, Y. Seki, M. Emori, P. Stonehart, *J. Electrochem. Soc.*, **143**, 3847 (1996).

[63] P. Berg, K. Promislow, J.S. Pierre, J. Stumper, B. Wetton, *J. Electrochem. Soc.*, **151**, A341 (2004).

[64] E.A. Cho, J.J. Ko, H.Y. Ha, S.A. Hong, K.Y. Lee, T.W. Lim, I.H. Oh, *J. Electrochem. Soc.*, **151**, A661 (2004).

[65] A. Damjanovic, M.A. Genshaw, J.O'M. Bockris, *J. Phys. Chem.*, **45**, 4057 (1964).

[66] N.M. Markovic, T.J. Schmidt, V. Stamenkovic, P.N. Ross, *Fuel Cells*, **1,** 105 (2001).

[67] N.M. Markovic, P.N. Ross, in *Interfacial Electrochemistry*, A. Wieckowski ed., p. 821, Marcel Dekker, New York (1999).

[68] R.A. Sidik, A.B. Anderson, *J. Electrochem. Soc.*, **528**, 69 (2002).

[69]   A.C. Luntz, J. Grimblot, D.E. Fowler, *Phys. Rev. B*, **39**, 12903 (1989).

[70]   R. Adzic, in *Electrocatalysis*, J. Lipkowski, P.N. Ross, eds., Chap. 5, p. 197, Wiley-VCH, New York (1998).

[71]   B.N. Grgur, N.M. Markovic, P.N. Ross Jr., *Langmuir*, **13**, 6370 (1997).

[72]   N.M. Markovic, H.A. Gasteiger, P.N. Ross Jr., *J. Phys. Chem.*, **100**, 6715 (1996).

[73]   A.B. Anderson, T.V. Albu., *J. Electrochem. Soc.*, **147**, 4229 (2000).

[74]   T. Jacob, R.P. Muller, and W.A. Goddard, III, *J. Phys. Chem. B*, **107**, 9465 (2003).

[75]   A. Eichler, J. Hafner, *Phys. Rev. Lett.*, **79**, 4481 (1997).

[76]   B.N. Grgur, N.M. Markovic, P.N. Ross, *Can. J. Chem.*, **75**, 1465 (1997).

[77]   C. Hartnig, M.T.M. Koper, *J. Electroanal. Chem.*, **532**, 165 (2002).

[78]   N. M. Markovic, T.J. Schmidt, B.N. Grgur, H.A. Gasteiger, R.J. Behm, P.N. Ross, *J. Phys. Chem.*, **103**, 8568 (1999).

[79]   A. Panchenko, H. Dilger, E. Roduner, J. Kerres, M. Hein, A. Ullrich, T. Kaz, in *Proceedings of the 2nd European PEFC Forum*, D. Stolten, B. Emonts, R. Peters, eds., Vol. 1, p. 79, European Fuel Cell Forum (2003).

[80]   J.L. Whitten, H. Yang, *Surf. Sci. Rep.*, **24**, 55 (1996).

[81]   M.T.M. Koper, R.A. van Santen, S.A. Wasileski, M.J. Weaver, *J. Chem. Phys.*, **113** 4392 (2000).

[82]   S.A. Wasileski, M.J. Weaver, M.T.M. Koper, *J. Electroanal. Chem.*, **500**, 344 (2001).

[83]   M. Garcia-Hernandez, D. Curulla, A. Clotet, F. Illas, *J. Chem. Phys.*, **113**, 364 (2000).

[84]   D.T. Sawyer, *Oxygen Chemistry,* Oxford University Press, London (1991).

[85]   A. Groß, A. Eichler, J. Hafner, M.J. Mehl, D.A. Papaconstantopoulos, *Surf. Sci.*, **539**, 542 (2003).

[86]   C. Puglia, A. Nilsson, B. Hernnäs, O. Karis, P. Bennich, N. Martenson, *Surf. Sci.*, **347**, 303 (1996).

[87]   P.D. Nolan, B.R. Lutz, P.L. Tanaka, J.E. Davis, C.B. Mullins, *J. Chem. Phys.*, **111**, 3696 (1999).

[88]   B.C. Stipe, M.A. Rezaei, W. Ho, *Phys. Rev. Lett.*, **78**, 4410 (1997).

[89]   M. Bauer, C. Lei, K. Read, R. Tobey, J. Gland, M.M. Murnane, H.C. Kapteyn, *Phys. Rev. Lett.*, **87**, 025501 (2001).

[90]   J.L. Gland, B.A. Sexton, G.B. Fisher, *Surf. Sci.*, **95**, 587 (1980).

[91]   G.B. Fisher, B.A. Sexton, *Phys. Rev. Lett.*, **44**, 683 (1980).

[92]   K. Bedürftig, S. Völkening, Y. Wang, J. Wintterlin, K. Jacobi, G. Ertl, *J. Chem. Phys.*, **111(24)**, 11147 (1999).

[93]   G.E. Mitchell, J.M. White, *Chem. Phys. Lett.*, **135**, 84 (1987).

[94]   G. Gilarowski, W. Erley, H. Ibach, *Surf. Sci.*, **351**, 156 (1996).

[95]   A. Michaelides, P. Hu, *J. Chem. Phys.*, **114 (1)**, 513 (2001).

[96]   M.T.M. Koper, T.E. Shubina, R.A. van Santen, *J. Phys. Chem. B*, **106,** 686 (2002).

[97]   T.E. Shubina, M.T.M. Koper, *Electrochim. Acta*, **47**, 3621 (2002).

[98]   P. Vassilev, M.T.M. Koper, R.A. van Santen, *Chem. Phys. Lett.*, **359**, 337 (2002).

[99]   D. Kim, B. Lee, D. Lee, *Bull. Korean Chem. Soc.*, **20(6)**, 696 (1999).

[100] E.A. Moelwyn-Hughes, *Physical Chemistry*, Pergamon Press, New York (1957).

[101] S. Nakanishi, Y. Mukouyama, K. Karasumi, A. Imanishi, N. Furuya, Y. Nakato,
       J. Phys. Chem. B, **104**, 4181 (2000).

[102] Y. Mukouyama, S. Nakanishi, T. Chiba, K. Murakoshi, Y. Nakato, *J. Phys. Chem. B*,
       105, 7246 (2001).

[103] P.A. Thiel, T.E. Madey, *Surf. Sci. Rep.*, **7**, 211 (1987).

[104] H. Ogasawara, B. Brena, D. Nordlund, M. Nyberg, A. Pelmenschikov,
       L.G.M. Pettersson, A. Nilsson, *Phys. Rev. Lett.*, **89**, 276102 (2002).

[105] S. Meng, L.F. Xu, E.G. Wang, S. Gao, *Phys. Rev. Lett.*, **89**, 176104 (2002).

[106] J.A. Weil, J.R. Bolton, J.E. Wertz, *Electron paramagnetic resonance: elementary
       theory and practical applications*, John Wiey & Sons, Inc., New York (1994).

[107] R.J. Cook, D.H. Whiffen, *Phys. Med. Biol.*, **7**, 277 (1962).

[108] A. Schweiger, G. Jeschke, *Principles of pulse electron paramagnetic resonance*,
       Oxford, University Press (2001).

[109] E.G. Janzen, *Acc. Chem. Res.*, **4**, 31 (1971).

[110] A.E. Dikalova, M.B. Kadiiska, R.P. Mason, *PNAS*, **98**, 13549 (2001).

[111] G.R. Buettner, *Free rad. Biol. Med.*, **3**, 259 (1987).

[112] J. Clarke, *SQUIDs*, *Scientific American,* **271(2)**, 46 (1994).

[113] T. Schmauke, M. Menzel, E. Roduner, *J. Molec. Catal. A: Chem.*, **194**, 211 (2003).

[114] D. Jiles, *Introduction to Magnetism and Magnetic Materials*, Kluwer Academic
       Publishers, Dordrecht (1990).

[115] *Ferromagnetic Materials*, K.H.J. Buschow, E.P. Wohlfarth, eds., North-Holland
       Publishing Company, Amsterdam (1980).

[116] S. Blundell, *Magnetism in condensed matter*, Oxford University Press Inc., New York
       (2001).

[117] P. Hohenberg, W. Kohn, *Phys. Rev.*, **136**, B864 (1964).

[118] W. Koch, M.C. Holthausen, *A chemist's guide to density functional theory*, Wiley-VCH, Weinheim, New York, Chichester, Brisbane, Singapore, Toroto (1999).

[119] W. Kohn, L.J. Sham, *Phys. Rev.*, **140**, A1133 (1965).

[120] F. Jensen, *Introduction to computational chemistry*, John Wiley & Sons, Chichester, New York, Weinheim, Brisbane, Singapore, Toronto (1999).

[121] S.H. Vosko, L. Wilk, M. Nusair, *Can. J. Phys.*, **58**, 1200 (1980).

[122] C. Lee, W. Yang, R.G. Parr, *Phys. Rev. B*, **37**, 785 (1988).

[123] P.J. Perdew, J.A. Chevary, S.H. Vosko, K.A. Jackson, M.R. Pederson, D.J. Singhm, C. Fiolhais, *Phys. Rev. B*, **46**, 6671 (1992).

[124] A.D. Becke, *J. Chem. Phys.*, **104**, 1040 (1996).

[125] A.D. Becke, *Phys. Rev. A*, **38**, 3098 (1988).

[126] L.A. Curtiss, K. Raghavachari, G.W. Trucks, J.A. Pople, *J. Chem. Phys.*, **94**, 7221 (1991).

[127] M. Segall, Dissertation, University of Cambridge (1997).

[128] G. Kresse, J. Hafner, *J. Phys. Rev. B*, **47**, 558 (1993).

[129] G. Kresse, J. Hafner, *J. Phys. Rev. B*, **49**, 14251 (1994).

[130] G. Kresse, J. Furthmüller, *Comput. Mater. Sci.* **6**, 15 (1996).

[131] P.E. Blöchl, *Phys. Rev. B*, **50**, 17953 (1994).

[132] G. Kresse, J. Joubert, *Phys. Rev. B*, **59**, 1758 (1999).

[133] M.T.M. Koper, in *Modern aspects of electrochemistry*, C.G. Vayenas, B.E. Conway, R.E. White, eds., Vol. 36, p. 51, Kluwer Academic/Plenum Press (2003).

[134] P.J. Hay, W.R. Wadt, *J. Chem. Phys.*, **82**, 270 (1985).

[135] Gaussian 98, Revision A.7, M.J. Frisch, G.W. Trucks, H.B. Schlegel, G.E. Scuseria, M.A. Robb, J.R. Cheeseman, V.G. Zakrzewski, J.A. Montgomery, Jr., R.E. Stratmann, J.C. Burant, S. Dapprich, J.M. Millam, A.D. Daniels, K.N. Kudin, M.C. Strain, O. Farkas, J. Tomasi, V. Barone, M. Cossi, R. Cammi, B. Mennucci, C. Pomelli, C. Adamo, S. Clifford, J. Ochterski, G.A. Petersson, P.Y. Ayala, Q. Cui, K. Morokuma, D.K. Malick, A.D. Rabuck, K. Raghavachari, J.B. Foresman, J. Cioslowski, J.V. Ortiz, A.G. Baboul, B.B. Stefanov, G. Liu, A. Liashenko, P. Piskorz, I. Komaromi, R. Gomperts, R.L. Martin, D.J. Fox, T. Keith, M.A. Al-Laham, C.Y. Peng, A. Nanayakkara, C. Gonzalez, M. Challacombe, P.M.W. Gill, B. Johnson, W. Chen, M.W. Wong, J.L. Andres, C. Gonzalez, M. Head-Gordon, E.S. Replogle, J.A. Pople, Gaussian, Inc., Pittsburgh PA (1998).

[136] P.E.M. Siegbahn, M.R.A. Blomberg, M. Wirstam nee Pavlov, R.H. Crabtree, *J. Biol. Inorg. Chem.*, **6**, 460 (2001).

[137] J.R.B. Gomes, F. Illas, *Int. J. Mol. Sci.*, **2**, 201 (2001).

[138] J. C. Slater, *Quantum Theory of Molecular and Solids, Vol. 4: The Self-Consistent Field for Molecules and Solids*, McGraw-Hill, New York (1947).

[139] V. Fock, *Zeitung für Physik*, **61**, 126 (1930).

[140] B. Miehlich, A. Savin, H. Stoll, H. Preuss, *Chem. Phys. Lett.*, **157**, 200 (1989).

[141] K. Ataka, T. Yotsuyanagi, M. Osawa, *J. Phys. Chem.*, **100**, 10664, (1996).

[142] P.S. Bagus, C.J. Nelin, W. Müller, M.R. Philpott, H. Seki, *Phys. Rev. Lett.*, **58**, 559 (1987).

[143] X. Li, A.A. Gewirth, *J. Am. Chem. Soc.*, **125**, 7086 (2003).

[144] H. Härle, A. Lehnert, U. Metka, H.R. Volpp, L. Willms, J. Wolfrum, *Appl. Phys. B.,* **68**, 567 (1999).

[145] M.J. Weaver, *Surf. Sci.*, **437**, 215 (1999).

[146] F.M. Baumann, Dissertation, Universität Stuttgart (1998).

[147] L. Petrakis, G. Grandy, *Nature*, **289**, 476 (1981).

[148] E.M. Cashell, V.J. McBrierty, *J. Mat. Sci.*, **12**, 2011 (1977).

[149] M.S. Akther, A.R. Chughtai, D.M. Smith, *J. Appl. Spectrosc.*, **39**, 143 (1985).

[150] O.E. Andersson, B.L.V. Prasad, H. Sato, T. Enoki, Y. Hishiyama, Y. Kaburagi, M. Yoshikawa, S. Bandow, *Phys. Rev B*, **58**, 16387 (1998).

[151] J.B. Goodenough, *Phys. Rev.*, **120**, 67 (1960).

[152] J.W. McClure, *Phys. Rev.*, **119**, 606 (1960).

[153] F. Tsui, L. Jin, O. Zhou, *Appl. Phys. Lett.*, **76**, 1452 (2000).

[154] R.R. Gupta, in *Landolt-Börnstein New Series II/16 Diamagnetic susceptibility*, K.H. Hellwege, ed., Springer, Berlin, 16, 7 (1986).

[155] S. Hudgens, M. Kastner, H. Fritzsche, *Phys. Rev. Lett.*, **33**, 1552 (1974).

[156] J. Heremans, C.H. Olk, D.T. Morelli, *Phys. Rev. B*, **49**, 15122 (1994).

[157] M.S. Dresselhaus, G. Dresselhaus, K. Sugihara, I.L. Spain, H.A. Goldberg, *Graphite Fibers and Filaments*, Springer-Verlag, Berlin (1988).

[158] S. Chehab, K. Guérin, J. Amiell, S. Flandrois, *Eur. Phys. J. B*, **13**, 235 (2000).

[159] J.C. Charlier, X. Gonze, J.P. Michenaund, *Carbon*, **32**, 289 (1994).

[160] M.F. Ling, T.R. Finlayson, C.L. Raston, *Austral. J. Phys.*, **52**, 913 (1999).

[161] R.C. Haddon, L.F. Schneemeyer, J.V. Waszczak, S.H. Glarum, R. Tycko, G. Dabbagh, A.R. Kortan, A.J. Muller, A.M. Musjsce, M.J. Rosseinsky, S.M. Zahurak,

A.V. Makhija, F.A. Thiel, K. Raghavachari, E. Cockayne, V. Elser, *Nature* (London), **350**, 46 (1991).

[162] R.S. Ruoff, D. Beach, J. Cuomo, T. McGuire, R.L. Whetten, F. Diedrich, *J. Phys. Chem.*, **95**, 3457 (1991).

[163] To be published in*: Studies of High-T$_c$ Superconductivity,* **44-45**, A. Narlikar, ed.

[164] K. Wakabayashi, *Mol. Cryst. Liq. Cryst.*, **340**, 7 (2000).

[165] K. Kawamura, T. Katsuramaki, *Am. Carb. Soc.*, Proceedings, 708 (1995).

[166] A. Nakayama, K. Suzuki, T. Enoki, S.L. Divittorio, M.S. Dresselhaus, K. Koga, M. Endo, N. Shindo, *Synth. Met.*, **57**, 3736 (1993).

[167] Y. Yamamoto, T. Miura, Y. Nakae, T. Teranishi, M. Miyake, H. Hori, *Phys. B: Condens. Matter*, **329-333**, 1183 (2003).

[168] F.E. Hoare, J.C. Walling, *Proc. Phys. Soc. (London)*, **B64**, 337 (1951).

[169] T. Sasakawa, T. Suemitsu, J. Kitagawa, O. Sologub, P. Salamakha, T. Takabatake, *J. Phys.: Condens. Matter*, **14**, L267 (2002).

[170] J. Kerres, W. Zhang, L. Jörissen, V. Gogel, *J. New Mat. Electrochem. Systems*, **5**, 97 (2002).

[171] J. Kerres, A. Ulrich, M. Hein, V. Gogel, K.A. Friedrich, L. Jörissen, *Fuel Cells*, **1-2**, 105 (2004).

[172] B. Yang, A. Manthiram, *Electrochem. Sol. State Lett.*, **6(11)**, A229 (2003).

[173] P. Staiti, F. Lufrano, A.S. Aricò, E. Passalacqua, V. Antonucci, *J. Membr. Sci.*, **188**, 71 (2001).

[174] O. Savadogo, B. Xing, *J. New Mat. Electrochem. Systems*, **3**, 345 (2000).

[175] A. Noshay, L.M. Robeson, *J. Appl. Polym. Sci.*, **20**, 1885 (1976).

[176] C.L. Ramos, S. Pou, B.E. Britigan, M.S. Cohen, G.M. Rosen, *J. Biol. Chem.*, **267**, 8307 (1992).

[177] M.L. McCormick, G.R. Buettner, B.E. Britigan, *J. Bacteriol.*, **180**, 622 (1998).

[178] K.D. Kreuer, *J. Membr. Sci.*, **185**, 29 (2001).

[179] A. Panchenko, H. Dilger, E. Möller, T. Sixt, E. Roduner, *J. Pow. Sources*, **127(1-2)**, 325 (2004).

[180] E. Gülzow, M. Schulze, N. Wagner, T. Kaz, R. Reissner, G. Steinhilber, A. Schneider, *J. Pow. Sources*, **86**, 352, (2000).

[181] J. Kerres, A. Ulrich, Th. Häring, M. Baldauf, U. Gebhardt, W. Priedel, *J. New Mat. Electrochem. Systems*, **3**, 129 (2000).

[182] F. Laurencelle, R. Chahine, J. Hamelin, K. Agbossou, M. Fournier, T.K. Bose, A. Laperriére, *Fuel Cells*, **1**, 66 (2001).

[183] W. Liu, K. Ruth, G. Rusch, *J. New Mat. Electrochem. Systems*, **4**, 227, (2001).

[184] G. Chen, E.A. Betterton, R.G. Arnold, *J. Appl. Electrochem.*, **29**, 961 (1999).

[185] J. Yu, B. Yi, D. Xing, F. Liu, Z. Shao, Y. Fu, H. Zhang, *Phys. Chem. Chem. Phys.*, **5**, 611 (2003).

[186] K. Stolze, N. Udilova, H. Nohl, *Acta Biochimica Polonica*, **47(4)**, 923 (2000).

[187] A. Panchenko, H. Dilger, J. Kerres, M. Hein, A. Ullrich, T. Kaz, E. Roduner, *Phys. Chem. Chem. Phys.*, **6**, 2891 (2004).

[188] H. Yanagida, Y. Masubuchi, K. Minagawa, T. Ogata, J. Takimoto, K.A. Koyama, *Ultrasonics Sonochem.*, **5**, 133 (1999).

[189] K. Makino, M.M. Mossoba, P. Riesz, *J. Phys. Chem.*, **87**, 1369 (1983).

[190] D. Han, E. Williams, E. Cadenas, *J. Biochem.*, **353**, 411 (2001).

[191] E. Finkelstein, G.M. Rosen, E.J. Rauckman, *J. Am. Chem. Soc.*, **102**, 4994 (1980).

[192] C.L. Hawkins, M.D. Rees, M.J. Davies, *FEBS Letters*, **510**, 41 (2002).

[193] O.M. Lardinois, K.F. Medzihradszky, P.R. Ortiz de Montellano, *J. Biol. Chem.*, **274,** 35441 (1999).

[194] D. Pietraforte, M. Minetti, *Biochem. J.*, **321**, 743 (1997).

[195] J. Vasquez-Vivar, B. Kalyanaraman, P. Martasek, N. Hogg, B.S.S. Masters, H. Karoui, P. Tordo, K.A. Pritchard Jr., *Proc. Natl. Sci. USA*, **95**, 9220 (1995).

[196] C. Lee, K. Miura, X. Liu, J.L. Zweier, *J. Biol. Chem.*, **275(50)**, 38965 (2000).

[197] P. Ionita, B.C. Gilbert, A.C. Whitwood, *Lett. Org. Chem.,* **1**, 70 (2004).

[198] D.I. Potapenko, Th.L. Clanton, E.G. Bagryanskaya, N.P. Gritsan, V.A. Reznikov, V.V. Khramtsov, *Free Radic. Biol. Med.*, **34**, 196 (2003).

[199] N.M. Atherton, *Principles of electron spin resonance*, Ellis Horwood PTR Prentice Hall, New York, London, Toronto, Sydney, Tokyo, Singapore (1993).

[200] J.L. Clément, J.P. Finet, C. Fréjaville, P. Tordo, *Org. Biomol. Chem.*, **1**, 1591 (2003).

[201] Y. Xu, Z. Chen, J. Sun, K. Liu, W. Chen, W. Shi, H. Wang, Y. Liu, *J. Org. Chem.*, **67**, 7624 (2002).

[202] F. Chalier, P. Tordo, *J. Chem. Soc.*, *Perkin Trans.*, **2**, 2110 (2002).

[203] P. Stampfuß, W. Wenzel, *Chem. Phys. Lett.*, **370**, 478 (2003).

[204] K. Huber, G. Herzberg, *Molecular Spectra and Molecular Structure: Constants of Diatomic Molecules*, Vol.4, Van Nostrand Reinhold, New York (1979).

[205] H. Nakatsuji, H. Nakai, *Chem. Phys. Lett.*, **197**, 339 (1992).

[206] P.H. Krupenie, *J. Phys. Chem. Ref. Data*, **1**, 423 (1972).

[207] M.E. Jacox, *Vibrational and Electronic Energy Levels of Polyatomic Transient Molecules, AIP*, Woodbury (1994).

[208] T. Shimanouchi, *Table of Molecular Vibrational Frequencies*, Consolidated Vol. 1, NSRDS, NBS-39.

[209] Y. Tarchouna, M. Bahri, N. Jaidane, Z. Ben Lakhdar, J.P. Flament, *J. Chem. Phys.*, **118**, 1189 (2003).

[210] M.T.M. Koper, R.A. van Santen, *J. Electroanal. Chem.*, **472**, 126 (1999).

[211] T. Li, P.B. Balbuena, *J. Phys. Chem. B*, **105**, 9943 (2001).

[212] X. Lin, N.J. Ramer, A.M. Rappe, K.C. Hass, W.F. Schneider, B.L. Trout, *J. Phys. Chem. B*, **105**, 7739 (2001).

[213] *Chemisorption and Reactivity on Supported Clusters and Thin Films*, R. Lambert, G. Pacchioni, eds., NATO ASI Series, Series E: Applied Sciences - Vol. 331, Kluwer Academic Publishers Group, Dordrecht (1996).

[214] S.A. Wasileski, M.T.M. Koper, M.J. Weaver, *J. Chem. Phys.*, **115**, 8193 (2001).

[215] S.A. Wasileski, M.T.M. Koper, M.J. Weaver, *J. Am. Chem. Soc.*, **124**, 2796 (2002).

[216] T. Ohwaki, K. Kamegai, K. Yamashita, *Bull. Chem. Soc. Jpn.*, **74**, 1021 (2001).

[217] S. Wilke, V. Natoli, M.H. Cohen, *J. Chem. Phys.*, **112**, 9986 (2000).

[218] Y. Wang, P.B. Bulbuena, *J. Phys. Chem. B*, **108**, 4376 (2004).

[219] E.F. Elstner, in *Sauerstoffabhängige Erkrankungen und Therapien*, BI-Wiss.-Verl., Mannheim, Leipzig, Wien, Zürich (1993).

[220] N. Kizhakevariam, I. Villegas, M.J. Weaver, *J. Phys. Chem.*, **99**, 7677 (1995).

[221] C.H. Hamann, W. Vielstich, in *Elektrochemie*, Wiley-VCH, Weinheim, New York, Chichester, Brisbane, Singapore, Toronto, (1998).

[222] A.B. LaConti, M. Hamdan, R.C. McDonald, *Handbook of Fuel Cells – Fundamentals, Technology and Applications*, Vol. 3: *Fuel Cell Technology and Applications*, W. Vielstich, H. Gasteiger, A. Lamm, eds., John Wiley & Sons, Ldt. (2003).

[223] S. Völkening, K. Bedürftig, K. Jacobi, J. Wintterlin, G. Ertl, *J. Phys. Rev. Lett.*, **83**, 2672 (1999).